UNIVERSIDAD DE CHILE
FACULTAD DE CIENCIAS FÍSICAS Y MATEMÁTICAS
DEPARTAMENTO DE GEOLOGÍA

ANALYSIS OF COOLING EFFECTS AND NON NEWTONIAN RHEOLOGY ON LAVA FLOW DYNAMICS

TESIS PARA OPTAR AL GRADO DE MAGÍSTER EN CIENCIAS, MENCIÓN GEOLOGÍA
MEMORIA PARA OPTAR AL TÍTULO DE GEÓLOGA

CAMILA CONSTANZA VERA VIDAL

PROFESOR GUÍA:
ANGELO CASTRUCCIO ÁLVAREZ

MIEMBROS DE LA COMISIÓN:
YARKO NIÑO CAMPOS
ALDO TAMBURRINO TAVANTZIS

SANTIAGO DE CHILE
2018

RESUMEN DE LA MEMORIA PARA OPTAR AL TÍTULO DE GEÓLOGA
Y GRADO DE MAGÍSTER EN CIENCIAS, MENCIÓN GEOLOGÍA
POR: CAMILA CONSTANZA VERA VIDAL
FECHA: 2018
PROF. GUÍA: ANGELO CASTRUCCIO ÁLVAREZ

ANALYSIS OF COOLING EFFECTS AND NON NEWTONIAN RHEOLOGY ON LAVA FLOW DYNAMICS

La actividad volcanica representa una gran amenaza para la propiedad privada, comunidades y habitantes ubicados en las cercanias de centros volcanicos. La volcanologia y mecanica de fluidos se utilizan en conjunto con el fin de estudiar la evolucion de los flujos de lava. Nos enfocamos en el estudio de flujos de lava simples y viscosos, de composiciones andesitica hasta riolitica, para determinar la relevancia de la evolucion reologica del flujo en tiempos de emplazamiento, distancias, y proporciones finales. Los experimentos analogos han sido una herramienta util en previos estudios de flujos de lava. Para este trabajo se caracterizo el manjar, un derivado de la leche, para utilizarlo como material analogo de lava viscosa con una reologia dependiente de la temperatura. Los experimentos simularon un flujo no confinado simple sobre una superficie inclinada, en el Laboratorio de Volcanologia Experimental del Laboratoire de Magmas et Volcans, Clermont-Ferrand, Francia.

Un total de 33 experimentos de extrusiones puntuales sobre una superficie inclinada, con caudales desde 1 (cc/s) a 25 (cc/s), con inclinaciones entre 10° - 15°, y diferentes temperaturas iniciales desde ambiente hasta 71℃. Cada experimento fue grabado con camara visual y camara termica, con los cuales se pudo obtener la evolucion termica y las distancias en el tiempo a las que avanzaba cada flujo. Se utilizo python para obtener la base de datos de temperatura, y bibliotecas especificas para manejar, procesar y visualizar datos, tales com matplotlib, scipy y pandas.

Los resultados indican que la formacion de una pseudo corteza en los flujos de manjar que estan sujetos a enfriamiento, controlan las distintas dimensiones y tiempos de emplazamiento obtenidos para los flujos estudiados, mientras que los cambios de pendiente tambien juegan un rol importante en estos resultados. La existencia de esta pseudo corteza esta basada en la perdida de agua presente en el manjar, asi como tambien en la buena correlacion existente que muestra el numero de Graetz con las diferentes dimensiones obtenidas, que dependen de la tasa efusiva, la escala de tiempo de extrusion, y por ende el desarrollo de esta corteza obtenida segun estimaciones basadas en la difusividad termica del material. Mayores caudales presentan flujos mas anchos con menores espesores, mientras que menores caudales se desarrollan de manera vertical, teniendo menor expansion areal y mayores espesores. Mayores pendientes resultan en flujos que se desarrollan principalmente pendiente abajo, con distancias de X_{min} e Y_{max} menores. Por otro lado, la comparacion entre flujos sujetos a enfriamiento versus flujos en condiciones isotermales, tambien apoyan la teoria de existencia de una pseudo corteza que controla la dinamica de flujo.

Los modelos DEM realizados presentan caracteristicas similares a las presentes en flujos de lava, con zonas de menor espesor cerca del punto extrusivo, seguido por un posible canal central entre estructuras tipo levee que culminan en un frente de flujo de gran espesor, presentando la mayor potencia del flujo. Este frente de flujo inflado, consideramos que es evidencia de que existe una pseudo corteza que contiene material con mayor movilidad en su

interior. Los perfiles de temperatura de termocuplas y FLIR, tambien muestran como existe un perfil termal vertical en los flujos, con altas temperaturas en porciones internas luego de que todo el material ya ha sido extruido, mientras la superficie del flujo presenta menores temperaturas.

ABSTRACT DE LA MEMORIA PARA OPTAR AL TÍTULO DE GEÓLOGA
Y GRADO DE MAGÍSTER EN CIENCIAS, MENCIÓN GEOLOGÍA
POR: CAMILA CONSTANZA VERA VIDAL
FECHA: 2018
PROF. GUÍA: ANGELO CASTRUCCIO ÁLVAREZ

ANALYSIS OF COOLING EFFECTS AND NON NEWTONIAN RHEOLOGY ON LAVA FLOW DYNAMICS

Volcanic activity represents a major threat to life, property and communities placed near volcanic centers. Volcanology and fluid mechanics work together in order to study the evolution of lava flows, which represent the high temperature and low velocity spectrum of volcanic processes. We focus on the study of simple viscous lava flows, ranging from andesitic to rhyolitic composition, to determine the relevance of rheological evolution on flow emplacement times, distances and final dimensions. Analogue experiments have been a useful tool in past studies of lava flows. For this work manjar, a dairy product from Chile, was characterized in order to use as analogue material of viscous lava with temperature dependent rheology. Experiments simulating a single unconfined flow over a slope were performed in the Experimental Volcanology Laboratory of the Laboratorie de Magmas et Volcans, Clermont-Ferrand, France.

A total of 33 experiments were performed consisting of point extrusions down an inclined smooth base, with initial flow rates from 1 (cc/s) to 25 (cc/s), slopes of 10° - 15°, and different initial temperatures ranging from ambient to 71℃. Each experiment was recorded with visual and thermal cameras from map view. Flow advance was measured in time with the help of a grid placed beneath the surface. Thermal data was retrieved with Python, obtaining basal area of the flow in time along with temperature evolution in time of interest points within the surface. Pandas, scipy and matplotlib libraries were used to access, process, analyze and visualize the data base obtained for the experiments.

Results indicate the formation of a pseudo-crust on manjar flows that are subject to cooling controls the different dimensions and times of emplacement obtained for the range of flow rates studied, while slope also plays an important role in these results. The existence of a pseudo-crust is based upon the water loss present for manjar flows, as well as the good agreement with timescales shown by Graetz number and different dimensions obtained that depend upon flow rate, extrusion timescale, and hence the development of crust obtained from thermal diffusivity of manjar. Higher flow rates present wider flows with smaller depths, and smaller flow rates develop vertically producing flows with thicker depths and narrower widths. Higher slopes result in flows that develop further downslope, with shortest upslope and cross-slope distances. On the other hand, comparison with isothermal experiments reveal there is significant difference between cooling and isothermal dynamics, supporting the presence of a pseudo-crust that controls it as well.

DEM models of the flows present similar features to those found in lava flows, with depressed zones near the extrusion point followed by channelization in between structures like levees followed by inflated flow fronts that present the thickest portion of the flows, which we take as evidence for the strength of an outer pseudo-crust containing hotter and less viscous material in the interior. Temperature profiles from thermocouples and *FLIR* data show how flow front material surface is subject to rapid temperature drops while inside portions of the flow

remain at high temperatures even after material injection has ceased.

Flow of matter is only a matter of time.

Agradecimientos

Para empezar, agradezco la paciencia de mis profesores, Angelo, Aldo y Yarko, por su tiempo, buena disposicion y apoyo en los altos y bajos de este proceso, y por mostrar su interés siempre en esta dulce versión de la ciencia. A Olivier Roche, por su confianza y por abrir las puertas para mi pasantía en el LMV, no solo una, sino dos veces. A Andrew Harris, por facilitar el uso de la camara FLIR, a Silvia Vallejo por enseñarme a usar la cámara y por tantas cosas mas, a Cyrille, quien materializo mi aparato experimental. A toda la familia del LMV, quienes hicieron de mi pasantia un momento increíble, Patricio, Ale, Anne, Cat, Swetha, Nélida y tantos más. Al Departamento de Posgrado y Postítulo de la Universidad por otorgarme la beca de pasantía, y al Posgrado de Geología por otorgarme la beca de ayuda de viaje para asistir a IAVCEI 2017. Agradezco también al Centro de Excelencia en Geotermia de los Andes, que me apoyó como tesista para realizar este estudio de posgrado y brindó apoyo económico para mi participación en congresos nacionales e internacionales.

Gracias a quienes me facilitaron la vida en Santiago y aportaron con su granito de arena a este trabajo, la Jacqui por siempre tener un abrazo o palabra de aliento, Felipe Cordera y Carlos Calvo por su ayuda con el reómetro, Felipe Uribe por el proceso pre Magister, Vivi del laboratorio de aguas, a todos en el laboratorio Civil. El paso por la Universidad, que dejó grandes amistades que me acompañan hasta el día de hoy, desde la sección 5, el breve paso por dimec, hasta el pregrado de Geología. También a los volcanólogos por los congresos, viajes y presentaciones vividas, y a los compañeritos de posgrado por todos los almuerzos, oncesitas, celebraciones y reuniones, el apoyo moral estuvo siempre presente.

A mi papá y mi Titi por su apoyo incondicional, porque me entregaron las herramientas para poder llegar hasta acá y me impulsan a ser siempre mejor, los adoro con todo mi ser, no hubiese llegado hasta donde estoy sin ustedes. Gracias a mis hermanas por inspirarme a ser mujer profesional, fuerte y autosuficiente, son dos polos opuestos que me han ayudado a buscar el equilibrio. También agradezco a mi familia de la vida, mis amigos los nerds, mis amigos del colegio, mis Palomitas, mis Bumeran, porque todos siempre han estado ahí en distintas etapas de este viaje de vida, y en todos los sube y baja de mi versión tesista.

Y por ultimo, y por todo, a Alfonso. Gracias por ser y crecer conmigo hasta acá, por haberle dado el sí a nuestra Bestia Peluda y por todo lo que se viene, ¡etapa superada!

Table of Contents

List of Tables

List of Figures

Chapter 1

Introduction

Lava flows represent a superficial expression of heat processes occurring in Earth's interior, where molten rock is ejected above the crust, and becomes landscape, being found in different geological settings throughout the globe. Even though these flows are slow moving, they are dangerous, destructive, and a significant hazard to communities in the vicinity of volcanic complexes. It is thus essential to understand the evolution of effusive volcanic eruptions, recognize the factors that control their dynamics, and emplacement. In the study of lava flows, field observation is a key element, providing the main source of information, and data gathering for scientists to work with. Although, challenges found in the field are hard to overcome: (1) good timing is needed as volcanic activity cannot be controlled or repeated at will, (2) the recurrence of different types of events is variable, (3) situations can turn dangerous easily, (4) processes under investigation cannot be observables by themselves.

A full understanding of lava flows dynamics attempts to predict final flow dimensions, and time of emplacement in order to evaluate hazards assessment of possible effusive eruptions near populated volcanic areas or to estimate as accurately as possible the evolution of an ongoing flow. This process must take into account a wide set of variables, most of which change rapidly within the chosen reference system, and in time. The complexity of this issue leaves us with a handful of possibilities that must be simplified and organized in order to be tackled. Analogue experimentation is then used to complement field observation by making laboratory models that can be controlled and repeated at will in a safe environment. The experimental system must have similarities with the natural event in order to make plausible links between the processes and their result. This can be achieved qualitatively by physical similarities, quantitatively by scaling analysis or both combined.

In the study of lava flows dynamics a first approximation when categorizing flows is based upon chemical composition, which can be a direct measurement of rheological properties that are known to control lava dynamics and influence in the final dimensions of the flow. The most famous type of flows are those found in world known volcanic centers like Hawaii and Etna, where eruptions are relatively frequent and last up to years long, pouring large volumes of hot material flowing over whatever crosses their path, like routes, private properties, fields or previously solidified black rock that form river-like morphologies. These flows are of basaltic composition, the low silica and also low viscosity end of magma composition. In general, these flows are relatively wider than thicker, presenting low aspect ratios and running out distances

of hundreds of kilometers. Given the periodicity and high frequency of basaltic events, there are several studies of flow dynamics, lava properties and in situ rheological measurements, allowing for scientists to better constrain the factors controlling the evolution of these flows. On the other hand, viscous and silicic lava flows with compositions from andesite to dacite and rhyolite, found in composite volcanoes, volcanic cones and near calderas, very typical across the Andes mountain range and other subduction zones between convergent margins of plate tectonics around the ring of Fire. Effusive activity of volcanoes found in this settings typically give rise to single events resulting in flows of simple viscous units with high aspect ratios. Due to the nature of these viscous flows the frequency of events is very low, this translates into a scarce register and information, leaving us mostly with past deposits to study their processes as geological evidence, with only a handful of contemporary eruptions from which advancement data has been obtained via satellite imaging or in situ measuring but no accurate data capturing the rheological evolution of these viscous flows during emplacement. There is still much to learn about this volcanic flows, given that emplacement mechanisms are not the same as basalts, their resulting morphologies can also vary greatly, and also represent a slow moving and destructive event.

This is where analogue models can be used to complement what we know about viscous, thermo-rheologically dependent flows down inclined planes, in order to constrain the role of system properties like flow rate, total volume erupted, and underlying slope, to name a few, with materials of heterogeneous, time-dependent properties.

1.1 Statement of the problem

The main concern with effusive volcanic eruptions is when and where lava will stop, and how long it will take to get there, specially when flows could affect roads, communities, or properties in their path. There are several studies that attempt to relate lava flow advance with a series of factors from the volcanic event, volcanic edifice and properties of the lava, and it is known that effusion rate is one of the major controls in the final dimensions of the flow Walker (1971). Most of these studies focus on the low viscosity end of lava flows, because of the larger register of events and information available to investigate, settling the base for studying all viscous flows.

Flows of lava represent a very complex phenomena with rheological properties that change with time, distance from the vent and within the flow due to cooling, crystallization, gas bubbles, flow velocity and more. This happens for all compositional ranges of lava, although not necessarily in the same rate or producing the same results. While silicate melt behaves as a Newtonian fluid for liquidus temperatures, lava has been proven to possess a minimum yield stress that needs to be overcome in order to initiate flow, and once lava is in motion, small increases in stress can cause large deformation. Numerous authors have characterized the rheology of lava with the Herschel-Bulkley model, which can describe the shear thinning behavior recognized in previous studies due to the presence of crystals, bubbles or even as a consequence of structure of the silicate melt Pinkerton and Sparks (1978), Dingwell (2015), and to in situ measurements of rheology Pinkerton and Norton (1995), property that has already been thought to explain how magma can ascend through vertical conduits given its high viscosities and yield strengths Colucci et al. (2017).This is why considerable

simplifications have been made in the use of numerical and analogue modeling, giving us a hint of how fluid mechanics is necessary to understand the coupling between cooling and evolution of the flow.

In addition to the behavior shown solely by lava composition, several changes in time should also be taken into account, as the ones previously mentioned like cooling, crystallization and more. It has been agreed by different authors that the rheology of lava is non-Newtonian with a minimum yield strength and a shear thinning behavior Liu et al. (2018), Vona et al. (2011); Castruccio et al. (2010); Whittington et al. (2009); Vetere et al. (2006); Pinkerton and Sparks (1978). The complexity of lava behavior has lead to a number of simplifications in order to constrain the problem of lava flows run-out length, dynamic behavior and evolution.

The use of analogue models of lava flows have been a useful tool in the last 30 years for constraining the role of previously mentioned factors. These models have used a variety of materials, mixtures and experimental set ups, starting from isothermal Newtonian fluids, Newtonian fluids with a solidifying crust, Bingham isothermal fluids, Bingham fluids with a solidifying crust and Herschel Bulkley isothermal fluids. For this reason, we propose a thermo rheologically dependent material with plastic behavior to model cooling flows in order to study the evolution and consequences of non-Newtonian flows in the laboratory as analogue for lava flows.

1.2 Scope of this thesis

The main goal of this thesis is to study highly viscous lava flows dynamics through experimental analysis with laboratory analogue models. In order to achieve this, specific goals are proposed:

- Study the rheology and feasibility of use for a material of temperature dependent rheology as analogue of viscous lava.
- Identify the role of cooling in the dynamics and emplacement of a simple flow of said material under a series of initial setups.
- Determine qualitative similarities between experiments and real lava flows morphologies.
- Compare the dynamics and emplacement proportions between scaled models and known data of natural events through dimensionless analysis.

1.3 Thesis structure

The present work focuses in the analogue modeling of viscous lava flows from the geologic and flow dynamics perspective. In **Chapter 1** the scope is presented with the main goals of the investigation, followed by a review of lava flow dynamics and rheology. In **Chapter 2** there is insight for the state of the art of lava flow analogue models, background on rheology and lava flows dynamics, emplacement and thermal evolution. **Chapter 3** presents the methodology followed for selecting the appropriate analogue material and the performing of small scaled lava flows with data acquisition. Once the methodology is set, the results

are shown in **Chapter 4**, organized according to the dynamics evolution of the experiment, followed by its emplacement times and final features and finally the thermal evolution of the flows. These results are discussed in **Chapter 5** with the conclusion of this work.

Glossary

Table 1.1: Glossary of data obtained from the experiments, initial characteristics, time dependent variables and final results.

Initial experimental values		
Symbol	Units or values	Description
Q	$m^3\ s^{-1}$	Flow rate
T_{i}	℃	Initial manjar temperature
α	$^\circ$	Angle with respect to the horizontal
U_m	[1,2,3]	Number of uses of manjar
Vol_t	m^3	Manjar total volume
T_{amb}	℃	Ambient temperature
ζ_Q	s	Material ejection timescale
Manjar Properties		
ρ	$kg\ m^{-3}$	Density
$\tau_y(T)$	Pa	Yield strength
$k(T)$	$Pa\ s^{n-1}$	Consistency
$n(T)$		Flow index
R	$^oC\ cm\ W^{-1}$	Thermal resistivity
λ	$W\ m^{-1}\ K^{-1}$	Thermal conductivity
c_v	$MJ\ m^{-3}\ K^{-1}$	Volumetric specific heat
κ	$m^2\ s^{-1}$	Thermal diffusivity

Table 1.2: Glossary of data obtained from the experiments, initial characteristics, time dependent variables and final results.

Results and relevant parameters		
Symbol	Units or values	Description
X_{max}	m	Downslope extent
Y_{max}	m	Cross-slope extent
X_{min}	m	Upslope extent
ξ_{max}	m	Maximum depth measured
t^*	s	Transition time
L^*	m	Transition downslope length
t_c	s	Time of cross-slope stabilization
t_u	s	Time of upslope stabilization
t_f	s	Time of run-out length completion
din		Data obtained from dynamic evolution
$flir$		Data obtained through *FLIR* imaging
$A_{\mathrm{din},flir}$	m^2	Total area of the flow
$\xi_{\mathrm{din},flir}$	m	Estimated depth
$\nu_{\mathrm{din},flir}$	$Pa\ s$	Viscosity estimate
T_{index}	-	Temperature index
V_1	$m\ s^{-1}$	Average velocity of early regime 1
vel	$m\ s^{-1}$	Average velocity of early regime 2
V_{final}	$m\ s^{-1}$	Final measure of flow velocity

Chapter 2

Background on Lava flows and Rheology

The flow of viscous fluids down an inclined plane is an important subject of research in the fluid mechanics field that has several applications in geology. Particularly for volcanologists there are a wide variety of gravitational currents as a result from different processes, for example, lavas flowing down volcanic vents or slow moving domes, to lahars and volcanic avalanches. Each of these flows present unique properties and features that must be taken into account for hazards assessment.

Lava flows consist of viscous material with properties that change continuously in time from extrusion until latter emplacement due to a series of factors. To understand and unify both geological and physical aspects of lava flows, this chapter includes the necessary background on these topics, in addition to the theory used for approaching scaling and analysis of results described in the discussion of this thesis.

2.1 Lava Flows

Lava flows are a mixture of molten rock, crystals and bubbles that spread over the underlying topography as a gravity current. During the evolution of the flow, these properties vary in time and space within the current due to heat loss, crystallization and volatile loss. This changes occur at different rates, and also heterogeneously in the flow, because of different times of exposure of material to ambient conditions, such as flow front material versus lava extruded in final stages of an eruption, or also due to layering within the flow, where the outer layer of lava versus material present in the inner core have different heat fluxes and rheological evolutions. This goes on until eventual complete solidification and crystallization takes place, reaching rock solid state, a process that can take up from days to years, depending on flow dimensions and ambient factors.

The main classification of lava flows is based upon chemical composition of total rock weight. According to their silica content, lavas range from basalts of 42wt% to 52wt% SiO_2, followed by andesite up to 62wt% SiO_2, dacite from 62wt% to 68wt% SiO_2 and rhyolite up to 78wt% SiO_2. Temperatures measured for freshly extruded lava range from 700℃ to over 1000℃, depending mainly on composition. Also, lava flow composition is an important control in eruptive style Cashman and Sparks (2013) and emplacement dynamics, where a number

of styles of lava flows can be found Griffiths (2000). Different lava flow styles can be related through lava composition, eruption temperature and effusion rate to different types of volcano morphologies and tectonic settings. On the same note, the variety of magma compositions lead to important differences in lava rheology Diniega et al. (2013), flow geometry and dynamical models used to study lava flows, that can, and usually have been, divided into basaltic or mafic and silicic Cashman and Sparks (2013). The silicic term will be used indifferently as viscous or highly viscous in the following chapters of this work, as those are the focus of study.

Viscous lava flows are found throughout the most relevant stratovolcanoes in the ring of fire, from the Andes to the Cascade Volcanic Arc in the U.S., also Japan and Indonesia, only to name a few places hosting famous silicic centers like Unzen volcano, Chaitén, Cordón Caulle, Chao, Santiaguito and Newberry. Previous studies of high silica flows have been with volcanic products of eruptions with no data from eruption to emplacement and focused mostly on lava flow morphology to infer conceptual models on flow dynamics Fink (1983), or inferred effusion rate by assuming yield strengths based on chemical composition of the flows and complemented data with analogue models Lyman et al. (2004).

The first detailed scientific observations of the emplacement of a rhyolite flow were made in the 2011-2012 eruption of Cordon Caulle in southern Chile, with effusion rates of up to 50 (m^3/s) at the beginning of the eruption, a total of 0,4 (km^3) of lava emitted and showing flow advance for up to 9 months after cease of material extrusion, where satellite imaging allowed the authors to determine the influence of lava crust on the advance of the flow Magnall et al. (2017). Prior to this eruption, Chaiten volcano gave rise to a rhyolite dome without development of laterally extensive flow field on 2008-2009 Pallister et al. (2013), with effusion rates of up to 66 (m^3/s) and an average of 45 (m^3/s) during the 4 months of eruption, resulting in a dome of 0,8 (km^3) according to photogrammetry estimates.

Other contemporary eruptions of viscous flows with available information of emplacement include volcanoes like Santiaguito, Colima and Lonquimay. On 1999 Harris et al. (2004) studied the evolution of an aa blocky flow of dacitic composition on Santiaguito Volcano in Guatemala, it had a duration of almost 3 years with low effusion rates in early stages of the eruption and higher in the latter, going from 0.6 to 2.1 (m^3/s) with an average of 0,45 (m^3/s). In this eruption, flow length increased due to thermal efficient transport of the material in the early stages of the event due to a cooled crust and hot core, which allowed fresh material reach kilometric lengths up to 3.75 (km) even with low effusion rates. The latter stage of higher flow rate did not come in hand with further lengthening and the flow was assumed to have reached its maximum cooling-length, with levées up to 117 (m).

The andesite flow of Colima volcano studied by Navarro-Ochoa et al. (2002) formed a block-andesite lava that grew via three branches until effusion rate waned, reaching velocities as high as 36 (m/h) in the steepest slopes during early stages of the eruption and decreased to 0.2 (m/h) in final stages, building a flow 3.8 (km) long with high aspect ratio despite the abrupt slopes of the volcano, confirming the non-Newtonian properties of the flow according to the authors.

On Christmas day of 1988, Lonquimay volcano formed a small cone on its northeast flank and extruded a 10.2 (km) long andesite lava flow with a volume of 0.23 (km^3) over a 13 month time span with an average effusion rates of 8 (m^3/s), that started with over 100 (m^3/s)

and wanned exponentially over time, being one of the first eruptions with detail study of its evolution in Chile Naranjo et al. (1992). The resulting flow morphology was studied in detail, with levée formation and front flow thickening along with apparent viscosity measurements with Jeffreys equation. All flows described here fit in the viscosity range of 10^5 to 10^9 (Pa s).

2.1.1 Rheology

Rheology is the science of deformation and flow of a fluid. It provides mathematical expressions for describing how a material deforms under an applied stress and allows for classification among a number of rheological behaviors Barnes et al. (1989).

The rheology of lava depends on the variety of factors present, and as lava flows evolve and are subject to new temperature conditions, these factors change as a result of cooling, crystallization, strain and vesiculation. The result is a complex heterogeneous dynamic system that can be described by different models according to the phase observed and time of observation.

For the study of lava flows three main models relating the applied stress, τ (Pa) with the deformation rate $\dot{\gamma}$ ($1/s$) are used and described as follows. The simplest and first relationship is shown in equation 2.1. A linear dependence of strain rate with stress, where μ is a constant named newtonian dynamic viscosity (Pa s). Fluids classified under this behavior are known as Newtonian and water is a common example, with a viscosity of 10^{-3} (Pa s). Silicate melts also fall into this category with viscosities that depend on composition, hydrous content, and temperature, with several models attempting to relate all these parameters in order to obtain approximated values Giordano et al. (2008), Hui and Zhang (2007).

$$\tau = \mu\dot{\gamma} \tag{2.1}$$

In any other case, as the ones described below, fluids are known as non-Newtonian.

The second relationship describes materials that need a minimum amount of stress in order to deform or flow, as described by equation 2.2 are called Bingham fluids. The minimum amount of stress is represented by τ_y, the yield strength, and μ_p, the plastic viscosity. Once the stress applied exceeds the yield strength, condition shown in equation 2.2, the material starts to deform in a linear manner between stress and strain. These are also referred to as viscoplastic flows. This is the most used rheological model for the study of lava flows, which are assumed as a mixture of silicate melt of Newtonian behavior, with a solid fraction represented by crystals that generate a net of connecting materials generating a yield strength Dragoni (1997) Lyman and Fink (2001) Filippucci et al. (2010).

$$\tau = \tau_y + \mu_p\dot{\gamma} \tag{2.2}$$

The last model often used to describe lava flows exhibits a minimum yield stress that needs to be overcome for flow to take place as criteria 2.3 shows. This results in thick deposits or stationary volumes on any slope, where a Newtonian fluid would go on flowing until surface tension effects take place.

$$\dot{\gamma} = 0 \Leftrightarrow \tau < \tau_y \tag{2.3}$$

Once this type of fluids is yielding, there is a non-linear relationship between stress and strain rate characterized by an index flow, n, and a consistency, k ($Pa\ s^n$), that depend on the properties of the material in study. In case $n > 1$ the fluid behaves as shear thickening with a viscosity that increases as stress is applied, also known as dilatant fluids. If $n < 1$ the fluid is shear thinning or plastic, which is the case studied in lava flows due to the arrange of a newtonian solution of silicate melt with a network of variable sizes and quantity of crystals and bubbles. As shown in equation 2.4, this model is the Herschel-Bulkley. When $n = 1$ the case simplifies to a Bingham model with $k = \mu_p$.

$$\tau = \tau_y + k\dot{\gamma}^n \tag{2.4}$$

For some fluids the shear-thinning behavior can also be a time dependent property, named thixotropy.

It is worth noting that there are plenty of non-Newtonian fluids with complex relationships such as the ones described above, that will not be discussed in the development of this work, the three mentioned models and time-dependent relationships are the most relevant rheological parameters and concepts used in the modeling of viscous lava flows.

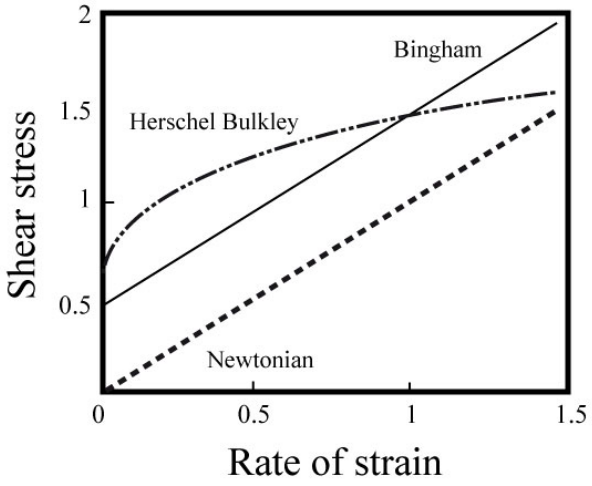

Figure 2.1: Three rheological models described above. The dashed line refers to Newtonian approach, straight line to Bingham model and dotted-dashed line a Herschel Bulkley model of a plastic fluid. Image modified from Balmforth and Craster (2000).

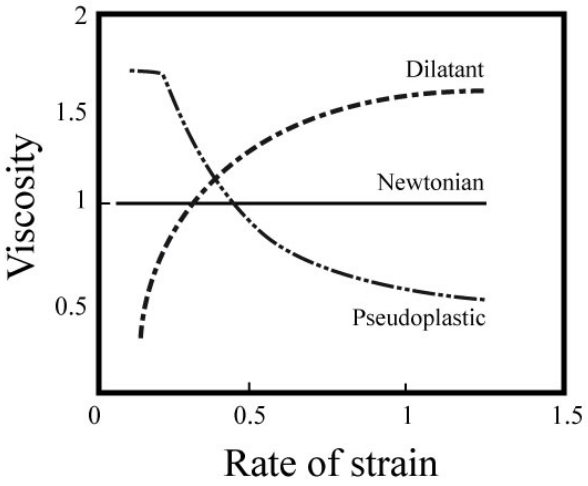

Figure 2.2: Fluids classified according to viscosity variation with strain rate.

As pointed out in this section, the point at which lava rheology is accounted for is very relevant, since extrusion at temperatures above the liquid temperature begins for molten magmas. For this reason, most models consider the use of Newtonian rheology, because at high temperatures the material is yet to develop significant yield stress, even when some shear thinning behavior has been agreed upon by different authors Cimarelli et al. (2011) Cordonnier et al. (2009). On the other hand, authors also have assumed the non-Newtonian behavior as apparent due to different factors controlling flow deformation Hess et al. (2008), or that depending on composition there is no need to take into account the effects of yield strength Lavallée et al. (2007). These disagreements lead us only to agree that the role in the complex interplay between all different factors influencing the response of lava to the wide spectrum of ambient and internal conditions over which are studying the subject it is yet to be fully understood.

Although previously mentioned facts can be misleading, the Herschel Bulkley model has been agreed upon by a good number of authors as has proven to be a good fit for available data on lava flow rheology, which reveals a shear thinning behavior for basaltic melts at liquidus temperatures with crystal contents below five percent, as well as for rhyolites, considering the power law exponent depends on temperature and crystal fraction Liu et al. (2018), Cimarelli et al. (2011), Spera et al. (1988). According to Spera et al. (1988) the power law exponent is dependent on temperature and crystal fraction, so the degree of non-Newtonian behavior increases if temperature increases, with smaller flow index as well as with crystal fraction. A recent study by Liu et al. (2018) states that this behavior is presented at solid fractions that exceed a critical value of 0.33 to 0.4, with shear thinning behavior, thixotropy and existence of an apparent yield stress that depends on solid fraction. Recent studies have developed a series of models that relate crystal fraction, strain rate and size distribution of particles to obtain values of consistency, flow index and yield stress from suspensions via analogue modeling Castruccio et al. (2010) or experimental data Cimarelli et al. (2011). Magma composition and water content has also proven to be as relevant when estimating

lava viscosity according to Whittington et al. (2009), given that water content produces such a high decrease in viscosity that the percentage of water in magma is just as important as composition, an andesite with 0% wt is more viscous than a dacite with 1%wt and a rhyolite with 2%wt.

The non-Newtonian behavior of magma is also studied to understand emplacement, where factors such as strain rate and pressure allow for suitable conditions in deformation of the magma in order to produce dyke intrusions as well as conduit ascent followed by flow spreading Petford (2003). Other condition to be considered is viscous heating produced by deformation in the flow, which can also explain the shear thinning behavior of magma and viscous reduction at ascent, or high strain rate conditions, permitting mobility Cordonnier et al. (2012). The presence of bubbles is also relevant factor in this equation and has been studied by Bagdassarov and Pinkerton (2004) and Bagdassarov and Pinkerton (2004), defining their role in shear thinning behavior of flows dependent upon strain rate. A recent study by Colucci et al. (2017) confirms the relevance in considering bubbles and non-Newtonian behavior of the flows, which accounts for magma upheaval through conduits due to heterogeneous profiles of pressure, strain rate and velocity distribution of material that permit higher exit velocities, mass flow and density during extrusion.

Thixotrophy has also been seen on these studies, according to Bagdassarov and Pinkerton (2004) it can be produced by bubble deformation and recovery due to changes in shear stress, noting that flow history is relevant for the study of lava evolution and is thought to be a factor controlling the development of effusive or explosive volcanic eruptions Cordonnier et al. (2012) Pistone et al. (2015).

2.1.2 Features and characteristics

The main focus of this study are simple lava flows, defined as a single unit of flow from a particular eruptive event in time, which may last from a few hours up to months, flows that cannot be divided into flow units with respect to emplacement or cooling dynamics Walker (1971). This definition leaves out compound lava flows that comprise a number of units emplaced, either dividing the flows into two or more branches, or overlapping flows, very typical feature in volcanic centers of basaltic composition.

Given a simple flow of viscous lava, few key morphological features are common to a number of deposits. Assuming an unconfined slope ranging from 0° to 20°, typical value found near volcanic vents, and according to the underlying topography, the resulting flow morphologies can be classified in the range of domes, *coulees* or blocky lava flows. Most lava domes and *coulees* are of dacitic to rhyolite composition, as well as blocky lava flows, although for all these morphologies lava composition can also range to andesite and even basalt. The exceptions where basaltic lavas also present these morphological features, despite their low viscosity, shows that composition is not the only factor controlling the final dimensions and characteristics of this flows, in this case, factors like extrusion rate, underlying topography and total volume take control of the resulting deposit characteristics, showing that viscosity of the material is only one of the factors influencing the final morphology of the flow.

Lava domes are emplaced in horizontal or sub-horizontal topographies, generating an axisymmetric flow that grows radially from the volcanic vent, forming as magma cools and degases

as it is subject to atmospheric conditions, comprising up to 6% of eruptions worldwide Sigurdsson et al. (2015). *Coulees* and blocky lava flows continue to elongate in the downslope direction after a phase of axisymmetrical radial growth from the vent until gravitational forces take control of the flow dynamics and lava begins to channelize and auto-confine. Eventually a maximum cross slope length is reached and the downslope direction represents the maximum distance measured from the vent until flow front. Both flows are characterized by an elongated downslope length but *coulees* are generally considered a transition flow between lava domes and lava flows, representing low-lying lava domes that have flowed downhill and present thicker deposits than lava flows. A general rule for all viscous lava flows described is the presence of high aspect ratio, this is maximum flow thickness versus width, in comparison to low viscosity flows. This is due to higher viscosities and yield strength which leads to final thicknesses from tens to hundreds of meters.

The textural term for describing the deposit of *coulees* or lava flows of viscous behavior is blocky. These are distinguished from other types of lava flows deposits because of their relatively smooth polyhedral blocks bounded by dihedral angles, lacking an exceeding amount of rough and spinose character seen in other types of lava flow, along with much thicker deposits of tens or hundreds of meters thick in comparison to other types of lava flows Sigurdsson et al. (2015). This type of flow is the most common among silicic lava flows ranging from andesite to rhyolite. The core of the flows are usually dense, vesicle free and may go from crystal rich with a phenocryst content of 60% to obsidian, meaning no crystals were nucleated and the structure solidified as glass. Ramping and fold structures are common, with the presence of ogives that are identified as cross-flow ridges, convex down flow with limbs that run close and parallel to the flow margins, usually found in the flow front. The term blocky *coul*ee is also used widely for describing this type of flows of silicic composition ranging from dacite to rhyolite.

2.1.3 Emplacement dynamics and thermal control

The first studies analyzing the factors controlling final length of lava flows proposed by Walker et al. (1973) gathered information of 41 basaltic to andesitic lava flows. Data showed good correlation between mean effusion rate and final lava flow length and the authors stated that viscosity control is relevant on the thickness of the flows rather than on control length, disregarding the general assumption that length was directly influenced by the viscosity of the fluid. Malin considered there was more to take into account than only flow rate, Malin (1980) postulated that volume erupted was the major control in final length after analyzing data of 84 historic flows on Mauna Loa and Kilauea in Hawaii, after seeing poor correlation between length and average effusion rate. Later studies determined that effusion rate and total volume are not the only factors to consider in the control of final length in lava flows.

Considering the impact of ambient conditions in the emplacement of lava, Guest et al. (1987) state that the thermal evolution of erupted material is relevant in determining the maximum length reached for a flow, classifying flows that are subject to ambient conditions for long periods of time where cooling of the distal portions of the flow is relevant, leading to thickened front flows and decreased advance rate due to cooled down material retaining hotter inner core flow. These are termed *cooling-limited*. By contrast, short lived eruptions where lavas do not reach a mature thermal state show an immediate decrease in advance rate once supply

from the vent is terminated, showing sluggish advance in the flow front due to drainage of the central channel are termed *volume-limited* flows, Walker (1971). This also leads to consider factors other than flow properties such as flow rate and volume for estimating total advance of lava. On this topic, the study by Pinkerton and Wilson (1994) took all data gathered by the previous authors and took into account morphology features of each flow along with effusion rates and total volume erupted to make a regression analysis. This lead to an empirical relationship between final length and factors such as time, slope and thickness, which translates as an indirect measurement of flow rheology being considered in this type of calculations. Efforts for predicting the emplacement of these flows have been made theoretically by different authors with several simplifications, in addition to complementary studies of numerical or analogue models for most of these studies.

Isothermal dynamics

Initial attempts to relate flow dynamics with rheological features were made for basaltic flows by Nichols (1939). In this study, the author was the first to propose basaltic flows moved with laminar motion, discarding previous attempts to estimate viscosities that assumed turbulent flow. Considering laminar motion and Newtonian behavior, he used equation 2.5 to estimate new lava flow viscosities. That is the Jeffreys equation and is used to roughly estimate this value for basaltic flows up to this day. In Jeffreys (1925) the author considers the flow of a Newtonian fluid (water) down an inclined plane, and proposed it is possible to relate the mean velocity of the flow (v) with the viscosity of the material (μ) for a channel much wider than deep as shown in 2.5.

$$\bar{v} = \frac{\mathrm{d}^2 \rho g \sin\alpha}{3\mu} \tag{2.5}$$

Where d is flow depth, ρ is the materials density and α the degree of the slope. However, this equation does not take into account the presence of a yield strength, hence it will over-estimate velocities and under-estimate viscosity values when applied to non Newtonian flows. This method is widely used up to this day even for viscous compositions of lava, were rheology estimates are necessary and little data is available Farquharson et al. (2015).

Theoretical solution of final dimensions of downslope and cross-slope extent considering isothermal Newtonian flow was presented by Lister (1992). In this work the author analyses the flow of a viscous fluid down an inclined plane from a point source using lubrication theory. He found the dynamical regime of the flow at short times correspond to the following descriptions of downslope and cross-slope distances.

$$X_{\mathrm{downslope}} \approx \left[\frac{(\rho g)^3 Q^4 (\sin\theta)^5}{(3\mu)^3 (\cos\theta)^2}\right]^{\frac{1}{9}} t^{\frac{7}{9}} \tag{2.6}$$

$$Y_{crossslope} \approx \left(\frac{Q\cos\theta}{\sin\theta}\right)^{\frac{1}{3}} t^{\frac{1}{3}} \tag{2.7}$$

The forces involved in his analysis correspond to buoyancy and viscous stress, neglecting surface tension and inertia. Although this work considers a very simplified case of viscous current down an inclined plane, it is the basis for the following studies on heterogeneous rheology with cooling and non-Newtonian materials.

Cooling dynamics

One of the first authors to study the role of cooling in viscous flows using analogue models was Stasiuk et al. (1993). In his experiments the author studied the spreading of an axisymmetric flow of heated syrup, a material with viscosity strongly dependent on temperature, over an horizontal surface in a very cold environment to determine the role of cooling over the relationship found by Huppert (1982). He determined that, at first, the flows spread like isoviscous flows such as the ones described by Huppert, and later the cooling effects take place, slowing the advance of the flow due to a bulk viscosity that stays constant over time. He also determined that bulk viscosity is sensitive to eruption rate and cooling effects rather than to eruption viscosity, stating that high eruption rates favor low bulk viscosities and long lava flows compared to decreasing eruption rates that produce increasing bulk viscosities with time.

Even when the evolution of a Newtonian fluid over a surface is still subject of active research, the study of non Newtonian fluids can be made with some idealizations and simplification in order to tackle a problem of higher complexities Balmforth et al. (2006). The main simplification made by the authors is that the fluid is relatively shallow and it moves slowly, this added to mass conservation constraints and making use of lubrication theory, they state it is possible to diagnose positions of upstream, downstream and maximum cross-slope lengths of a power law fluid with yield strength extruded at a constant flow rate via scaling theory, following power laws in time. According to observation, the flow is seen to move between a set of regimes that depend on the dominant balance of forces acting up in the fluids advance. The dynamical regimes described by the authors are based upon dominance of either slope or yield stress component, although both play little role in the initial phase of extrusion evolution, which is characterized by an axisymmetric Newtonian fashion. This can be followed by one of two early life regimes, the first consists of an important gravity component that guides the downslope extent. The second indicates the flow follows a slope-dominated Newtonian state. Both regimes are followed by a late-time transition that leads to an inclined, yield-stress dominated state.

In the study of shallow viscoplastic flows on an inclined plane, Balmforth et al. (2002) shows both numerical and analytical solutions for a reduced equation of a Herschel-Bulkley constitutive law of isothermal fluids, neglecting the effects of temperature variations that lead to changes in rheology. With these approximations in mind we can compare the dynamic regimes of the flow and determine when temperature changes take an effect on the evolution of the flows. According to the authors, for a viscoplastic material the temporal evolution of the flow follows a power law of the time with constant slope that depend on a number of things, like forces governing the flow: either yield stress dominated or not. Their analysis is shown in tables 2.1 and 2.2, n refers to the flow index of the material and B to the Bingham number defined as equation 2.8:

$$B = \frac{\tau}{\mathrm{e}\rho g H cos(\theta)} \tag{2.8}$$

Table 2.1: Time exponent according to Balmforth et al. (2002) for experiments with B«1 and n $\neq 0$. Maximum value of flow index is found at 20℃ and minimum at 47.55℃.

n	0.445		0.677	
Regime	Early Regime	Long time regime	Early Regime	Long time regime
X_{max}	0.456	0.745	0.477	0.763
Y_{max}	0.456	0.333	0.477	0.333
X_{min}	0.456	-0.078	0.477	-0.096

Table 2.2: Time exponent according to Balmforth et al. (2002) for experiments with B>1 and n $\neq 0$, defined as yield dominated.

Regime	X_{max}	Y_{max}	X_{min}
Early Regime	0.4	0.4	0.4
Long time regime	1	0	0

2.2 Dimensional analysis and π theorem

The main goal of analogue models is to understand complex natural processes via experimental methods developed in a controlled, repeatable environment through observation in a laboratory. Given the problem of an unconfined viscoplastic material flowing down an inclined plane with a free surface, its complexity leaves us with no satisfactory mathematical model to formulate. It is here where experimental methods as the ones used in this thesis can establish similarities and simulate physical features of the problem properly. This can be done on the basis of dimensional analysis.

This analysis consists of organizing the dimensional quantities involved in one specific set of physical variables into a series of dimensionless groups in order to identify relevant dependencies of the problem tackled.

The controlling variables will have dimensions that are a combination of the basic dimensional quantities such as mass (M), time (T), length (L), temperature (K), electric current (A), number of molecules (N), etc. The number of applicable quantities to a specific experimental system is identified as n. The controlling variables are identified as m and can be determined experimentally according to the system in study.

The following cases are possible:

- When $m \leq n + 1$ the dimensionless combination of variables can be determined.

- When $m > n+1$ dimensionless groups must be identified and understood based in terms of their physical meaning in the experimental system. Scaling between natural and analogue processes is assessed by comparison of these dimensionless variables calculated for each system.

Dimensionless groups identified with this procedure need to be understood according to their physical meaning. The scaling procedure between natural scenario and laboratory models can be assessed by comparing the same dimensionless group, in order to determine if experiments can actually represent the full scale process.

Typical dimensionless numbers in the analysis of lava flows correspond to the following:

The Reynolds number represents the ratio between inertial and viscous forces of the fluid, indicating whether the dynamical regime of a flow is laminar or turbulent. Most lava flows are laminar, with Re numbers well below 500 when V is the mean velocity of the flow and h represents flow depth.

$$Re = \frac{Vh}{\mu} \tag{2.9}$$

The Froude number represents the ratio between gravity forces and viscous forces of the fluid, indicating the relevant importance of the flow velocity versus gravity wave speed, which classifies flows as sub-critical or supercritical.

$$Fr = \frac{V}{g \sin\theta} \tag{2.10}$$

The Graetz number has been used by a number of authors for considering heat loss in lava flows. Variables are V mean flow velocity, κ the thermal diffusivity of the material, L is the length of the flow, and $\mathrm{d_e}$ the equivalent diameter of the flow, which is equal to four times the cross sectional area divided by the wetted perimeter. Pinkerton and Wilson (1994) states that lavas reach a critical Graetz number when reaching their final lengths, with the critical value going from 200 to 300.

$$G_z = \frac{V_1 \mathrm{d}^2}{\kappa X} \tag{2.11}$$

The Peclet number describes the balance between conductive and advective heat transport, showing for a series of basaltic flows that advection is more important relative to conduction in lava flows, but not as much as in analogue models. The larger the Pe, the smaller the heat loss from the surface and farther the lava surface moves before it reaches solidification temperatures.

$$Pe = \frac{V\mathrm{d}}{\kappa} \tag{2.12}$$

The Bingham number reflects the ratio of yield strength of the fluid to a characteristic viscous stress. Flows of purely viscous fluids have B = 0 while yield strength is large enough to prevent flow when $B = B^*$. B^* represents a critical Bingham number.

$$B = \frac{\tau_y}{\rho g H} \tag{2.13}$$

Chapter 3

Material characterization and experimental setup

For the development of this thesis and the study of scaled models of lava flows the following chapter establishes two main steps regarding the methodology. The first is the criteria used for selecting manjar Nestlé as analogue material along with the detailed study of its intrinsic and rheological properties. The second is the experimental methodology followed in the laboratory for performing the models proposed, the setup and materials used, and data acquisition.

3.1 Material selection

To accomplish suitable results, it is key to find a material that allows plausible links between the laboratory experiments and viscous lava flows, either through qualitative similarity or quantitative scaling analysis. The proposed criteria for material selection follows two main guidelines:

Similar rheological behavior to the flows we aim to study:

- Non-Newtonian.
- Temperature dependent rheology.

Pragmatism:

- Readily available and affordable for this thesis budget.
- Easy to handle in the laboratory, neither toxic nor dangerous to use.

A total of four fluids were chosen according to the latter two criteria and were tested for the first two in the laboratory. The test consisted in a simple model for uncovering temperature dependent rheology based on the the instant release of an axisymmetric flow on an horizontal plane. As shown by Huppert (1982), the geometry of the flow as a function of time of the material can be related by equation (3.1) where r_n is the radial extent of the flow, V is the flow velocity, μ is the Newtonian dynamic viscosity and t the time elapsed, considering a fluid with Newtonian behavior and a constant value of viscosity. The coordinate system is shown

in Figure 3.1, where z is the vertical ax indicating the center of the cilinder from where the material is dropped.

$$r_n = 0.894(\frac{gV^3}{3\mu})^{1/8}t^{1/8} \tag{3.1}$$

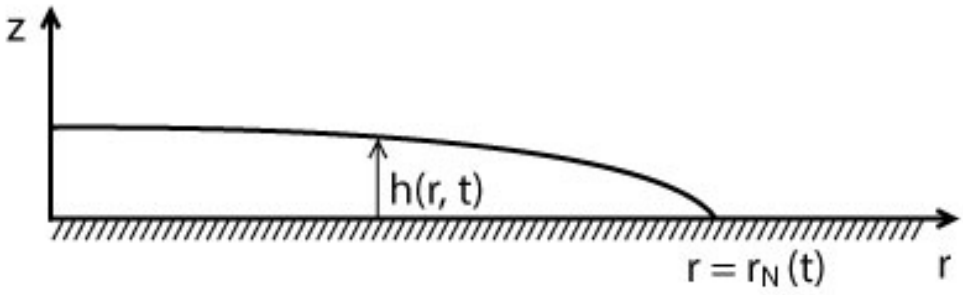

Figure 3.1: Coordinate system in the perpendicular view of an axisymmetric flow for estimating the radial extent from $r = 0$ to $r = r_n(t)$. Modified from Huppert (1982).

.

This model allows for a simplified estimation of an apparent viscosity given the previously mentioned constraints. A chosen constant volume of each material is heated at 3 different temperatures and recorded with a video camera directly from above for measuring radial extent versus time to obtain a range of viscosity values assigned to these different temperatures. Velocities are estimated as the advance of an average value of 4 axisymmetric points representing the ratio of the flow in time, obtained from video files. Chosen fluids were: (1) natural honey, (2) manjar Nestlé, (3) syrup and (4) caramel. The summary of results obtained in these tests is shown in Table 3.1.

For manageable temperatures in the laboratory, the apparent Newtonian viscosities obtained indicate that the most suitable material is manjar Nestle. Being a dairy product it is very easy to handle, water-soluble, readily available and presents a range of 3 orders of magnitude in viscosity for the chosen range of temperatures. This leads to a full study of manjar intrinsic properties and rheology prior to the development of experimental scaled lava flows. This criteria is similar to the one used by Stasiuk et al. (1993) when studying the effects of cooling in lava flow emplacement. The viscosity dependence of temperature for typical analogue materials like syrup and PEG 600 is compared to manjar in addition to andesite in Figure 3.2 modified from the latter study.

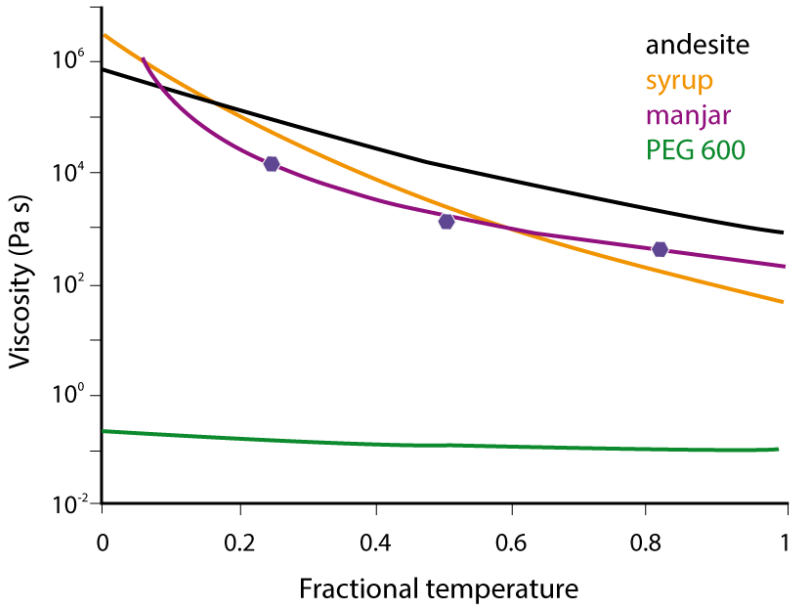

Figure 3.2: Viscosity as a function of temperature expressed as a fraction between two temperature end points. Modified from Stasiuk et al. (1993). Manjar from 23℃ to 70℃ shows the three points measured and the resulting curve with a power law adjustment. Curves for the remaining materials are extracted from the mentioned paper, with temperature limits as follows: glucose syrup from -20℃ to 30℃, polyethylen glycol 600 from 17℃ to 40℃, and andesitic melt from 800℃ to 1200℃.

Table 3.1: Viscosity results obtained in simple axisymmetric flows at different temperatures for honey, manjar Nestle, syrup and caramel.

Material	Initial temp. (℃)	Ambient temp. (℃)	Maximum depth (mm)	Final radial extent (cm)	Time elapsed (min)	Apparent viscosity (Pa s)
Honey	16	14	5	11,5	5,8	522,0
	25	14,5	3	13	13,3	138,4
	35	15	1,5	12,5	16,9	83,3
Manjar Nestle	35	18	2,5	6	1,9	15200,5
	48	18	12	7,5	1,3	1370,8
	61	18	9	8,3	1,0	437,1
Syrup	9	15	3,5	13	4,2	53,8
	16	15	2,5	14,5	3,7	31,2
	33	15	2	14	0,7	8,1
Caramel	30	16	2	15	0,5	5,4

3.2 Manjar Nestlé characterization

Once determined that the material chosen as analogue for the modeling of viscous lava flows is manjar Nestlé, a series of measurements and tests are carried out in order to determine relevant parameters for the development of this thesis.

Manjar Nestlé is a dairy product manufactured in Chile with an industrial automatized process that follows a fixed recipe maintaining a regular proportion of ingredients. It is sold in sealed alumina foil packages available in every supermarket and convenience store in Santiago, Chile. Packages of 1 (kg) shown in Figure 3.3 were used for most measurements and experiments performed on this work, in other cases a smaller version of 200 (gr) as shown in 3.5 was used. Properties and values exposed in the following sections correspond to this brand and packaging of manjar only and may differ from other brands due to different formulas but a stack of manjar was bought for the measuring of physical, thermal and rheological parameters as well as in the laboratory experiments performed so their properties remain constant between the packages.

Figure 3.3: Reference picture of a 1(kg) package of manjar Nestlé used in this work.

3.2.1 Manjar properties

As previously stated, manjar is a dairy product and its main ingredients are water and sugar, because of this the intrinsic properties of the material vary with many factors such as heat, time and exposure to atmosphere. From now on, when referring to the use of manjar for experiments or measurements, it is given that the material is fresh and just poured out of the package unless stated otherwise.

Density

The density of manjar was measured at room temperature of 2℃ and set to a constant value of 1340 (kg/m^3) for the following chapters of this thesis. Although it is a fact that density for this material varies due to water loss and temperature variations, the effect of each of these variables in density changes escapes from the scope and goals of this study. Previous studies have constrained density values for *dulce de leche*, a material similar to manjar, within the same temperature range as the one used in the experiments performed in this thesis. They found that density decreases with temperature, going from 1350.7 to 1310.7 (kg/m^3) Barbosa et al. (2013).

Water content

Given that this thesis consists in the study of heated manjar behavior as gravitational current, the water content in time is measured against temperature for a given amount of material. Manjar total weight is measured in a precision scale and is heated from ambient temperature, to boiling point and until cooling. The weight variations in time are assumed to be water loss of the material due to evaporation. The results in Figure 3.4 show that while getting the material to a boiling point of 67℃ a 2.4% water loss occurs at a faster rate than when cooling after the boiling point was reached. A total of 4.86% of material weight is loss in the process.

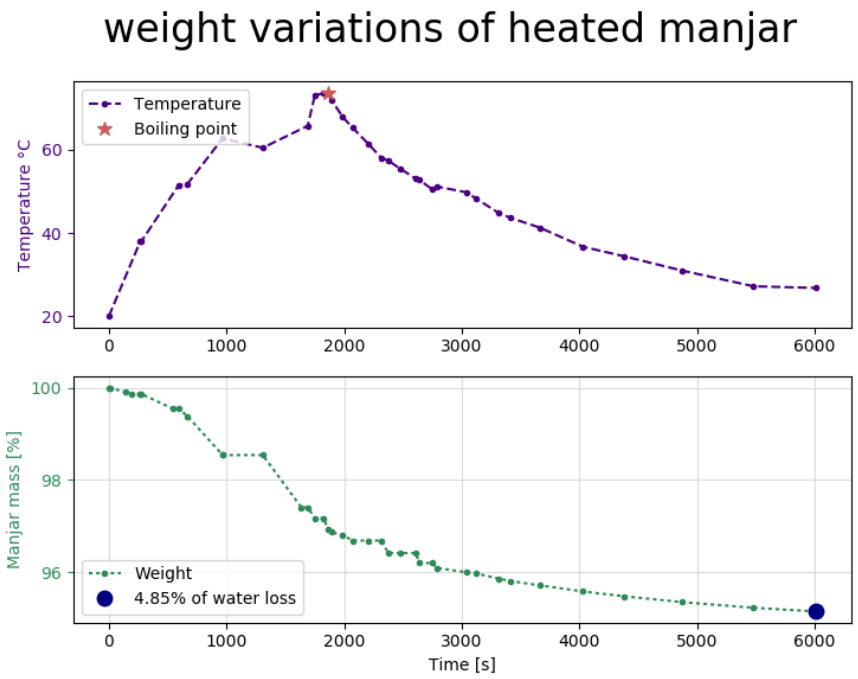

Figure 3.4: Percentage of water content variation in manjar with time and temperature.

Thermal properties

To estimate thermal properties of manjar, a portable instrument available in Centro de Excelencia en Geotermia de los Andes (CEGA) is used. A source of linear heat from an electronic probe applied to solids or very viscous materials and connected to the KD2 Pro Decagon Devices, Inc. shown in Figure 3.5 connected to a certain type of probe can make different readings of thermal properties. The probe used consists of the dual needle SH-1, a 1.3 (mm) diameter x 3 (cm) long with 6 (mm) space between needles, and when completely inserted in viscous manjar at ambient temperature of 21℃ and set in low power mode, it measures thermal conductivity, thermal resistivity, diffusivity and volumetric specific heat Devices (2011). A total of 33 point measures were made and the summary of gathered data is shown in table 3.2.

Figure 3.5: Two packages of 200 (gr) of manjar for measuring thermal properties with KD2 Pro, Decagon Devices with needle SH-1. Photo by the author.

Table 3.2: Thermophysical properties of manjar, all values measured at 21°C

Thermal Resistivity ($℃\ \frac{cm}{W}$)	**Thermal Conductivity** ($\frac{W}{mK}$)	**Volumetric Specific Heat** ($\frac{MJ}{m^3K}$)	**Diffusivity** ($\frac{m^2}{s}$)
290	0,34	3,2	1,00E^{-7}

3.2.2 Manjar rheology

The rheology of manjar was measured in a rotational rheometer Rheolab QC Anton Paar set up with a temperature control device Peltier C-PTD 180/AIR/QC as shown in Figure 3.6.

The machine is located in *Laboratorio de Reologia*, in the Civil Engineering Department of Universidad de Chile. This instrument consists of a static cup that must be filled up with the desired material before inserting a mobile concentric cylinder or vane connected to the device that rotates according to the input settings defined by the user. Considering measures of torque, T (μNm), and angular velocity, ω ($mrad$), required for the inner cylinder or vane to rotate at desired settings, the values of shear rate, stress and yield strength are estimated.

Figure 3.6: Rotational rheomether Anton Paar used in this work. Photo by the autor.

For measuring the yield stress, a four bladed vane immersed in a sample of the material rotates slowly at a constant rate to detect the yielding moment when the torque reaches a maximum value, according to Dzuy and Boger (1985). When the material is subject of shear stress it is assumed a uniform distribution everywhere on the cylinder, equal to the yield stress τ_y when the torque is at maximum T_{max}. The geometry of the vane is also considered for estimating the yield strength as shown in equation 3.2, where D and H represent the diameter and length of the vane, respectively.

$$T_{max} = \frac{\pi D^3}{2}(\frac{H}{D} + \frac{1}{3})\tau_y \tag{3.2}$$

The plot of torque versus deflection angle shows an increasing curve that reaches a peak, T_{max}, followed by stable value. The same test is made for 18 manjar samples at temperatures ranging from ambient to boiling, 23℃ to 70℃.

Next, with concentric cylinder cups, the rheometer generates an output of corresponding shear stress τ, shear rate $\dot{\gamma}$, viscosity and more. The outputs are based on the norm DIN ENISO 3219:1994 (1994) and equations 3.3 and 3.4, where R_1 and R_2, are the ratio of each of the cups, L, the length of the inner cup and finally on C_l, a correction factor that accounts

for the torque acting at the end faces of the measuring system that has been calibrated for this rheometer.

$$\tau = \frac{1 + (\frac{R_2}{R_1})^2}{2} \frac{T}{2\pi R_2^2 L C_l} \tag{3.3}$$

$$\dot{\gamma} = \omega \frac{1 + (\frac{R_2}{R_1})^2}{(\frac{R_2}{R_1})^2 - 1} \tag{3.4}$$

Given the non-Newtonian behavior of manjar, directly obtained output data from the rheometer as shear stress τ and shear rate $\dot{\gamma}$, are re-evaluated with previously estimated τ_y and presented as the difference between these two values, shown as τ_{rep} and $\dot{\gamma_{rep}}$ in equations 3.5 and 3.6.

$$\tau_{rep} = \tau - \tau_y \tag{3.5}$$

$$\tau_{rep} = k \dot{\gamma_{rep}}^n \tag{3.6}$$

With the resulting curve of τ_{rep} and $\dot{\gamma_{rep}}$, we proceed to estimate the rheological parameters of the fluid by adjusting the curve according to Herschel-Bulkley model that was presented in the previous chapter, which is the equivalent to a power law fit. The norm DIN ENISO 3219:1994 (1994) establishes the adjustment shown in equation 3.7 should be made. Considering the relevant range of deformation rates expected for manjar flows in experiments performed for this Thesis, this adjustment is made specifically between strain rates from 0 to 0,6 (s^{-1}). Equating the relationships shown in equation 3.5 and 3.6 results in the desired model and values of consistency and flow index are obtained. Rheometer output data is shown in Figure 3.7, as well as representative values here used and the power law adjustment applied for said strain rates also shown in dark blue.

$$\tau = f(\dot{\gamma}) \tag{3.7}$$

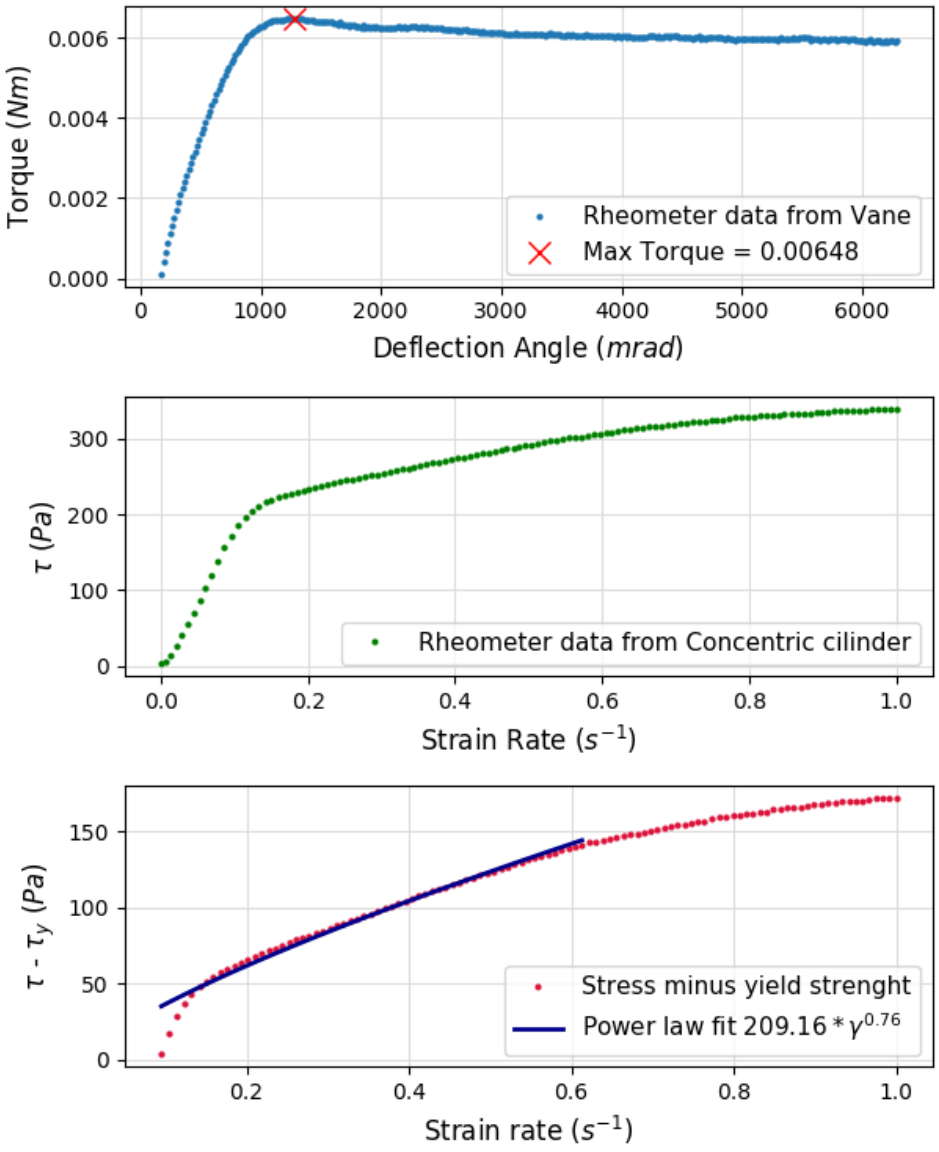

Figure 3.7: Rheometer output for estimating Yield Strength, Consistency and Flow Index for manjar at ambient temperature.

All obtained measuremments of consistency, flow index and yield strength are shown in Figure 3.8. For the chosen thermal range τ_y shows a very strong positive correlation with a power law fit, while, k and n data demonstrates poorer correlations with the best fits here presented. Consistency shows a negative dependence on temperature, with higher values at ambient conditions that decrease linearly as temperature increases. Flow index in temperature best fit is presented as a quadratic equation, with higher n values near 1 at ambient temperature that go down to 0.44 in temperatures from 35℃ to 45℃ and go up again near 0.7 for maximum temperature range used.

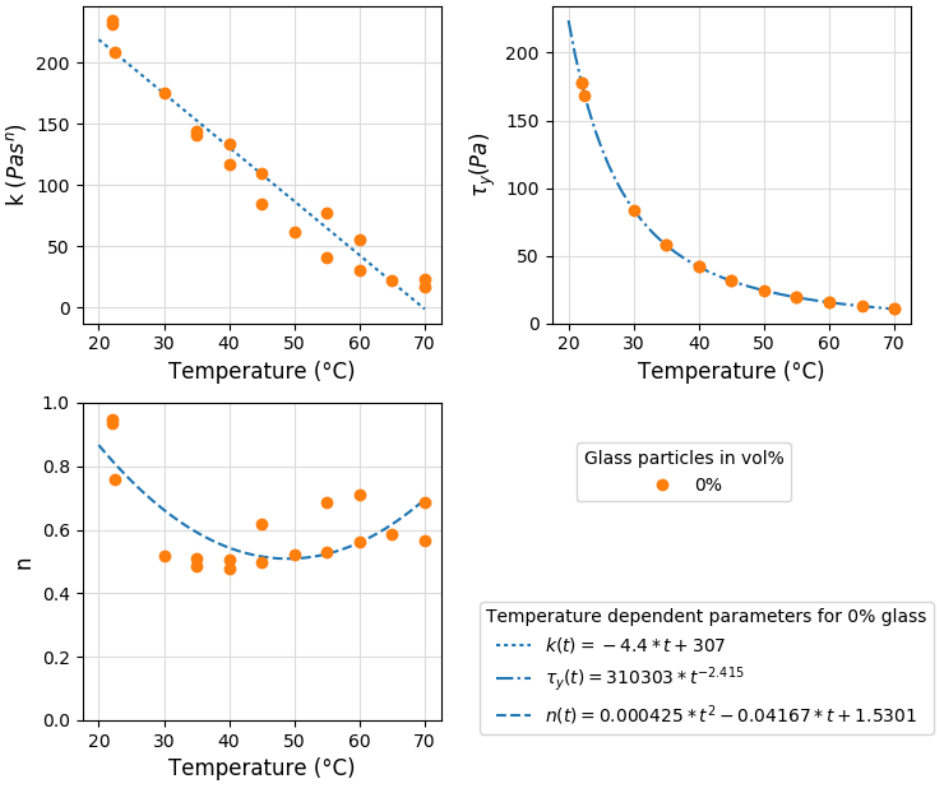

Figure 3.8: Yield strength, consistency and flow index versus temperature data and corresponding best fits for measurements made at strain rates from [0-0.6] (s^{-1}).

A second set of measurements were made including three mixtures of manjar and glass particles with concentrations of 20%, 30% and 40% in volume for each temperature, with shear rates going from [1-50] (s^{-1}), in order to obtain a broad spectrum of rheological properties. Glass particles have been previously used in experimental volcanology for simulating crystals Castruccio et al. (2010), and are known to modify the rheology of the magma depending on solid fraction concentration Costa (2005), shape and size Moitra and Gonnermann (2015). According to Stokes law, the settling time of this glass particles immersed in a viscous fluid like manjar allows for velocities of 0,0000784 (m/s). Compared to the time of the tests carried out, we assume there is no time for settling and this phenomena does not interfere with the results obtained. This topic has been discussed by Balmforth et al. (2014), who considers a key feature of viscoplastic fluids is that yield stress can prevent settling if the critical ratio of τ_y to buoyancy stress does not exceed the plastic limit, although this topic is still a matter of study because discrepancies have been found for multiple particles.

These results are compared to defined fits for k, n and τ_y in Figure 3.9. Yield strength shows decreasing behavior with temperature regardless of glass particle content, with a good correlation with previously found power lat fit, except for higher particle content measurements that appear to have higher τ_y values for temperatures below 40°C. Consistency values do not show a specific fit or correlation with our previous measurements, but remain in the same range of values obtained. Flow index results for manjar and glass particle mixtures reveal

a similar behavior with manjar with no glass particles, with higher values for lower temperatures that decrease as temperature increases, which could represent part of a quadratic fit as the one shown in light blue but as there is only a limited number of measurements per mixture this cannot be confirmed.

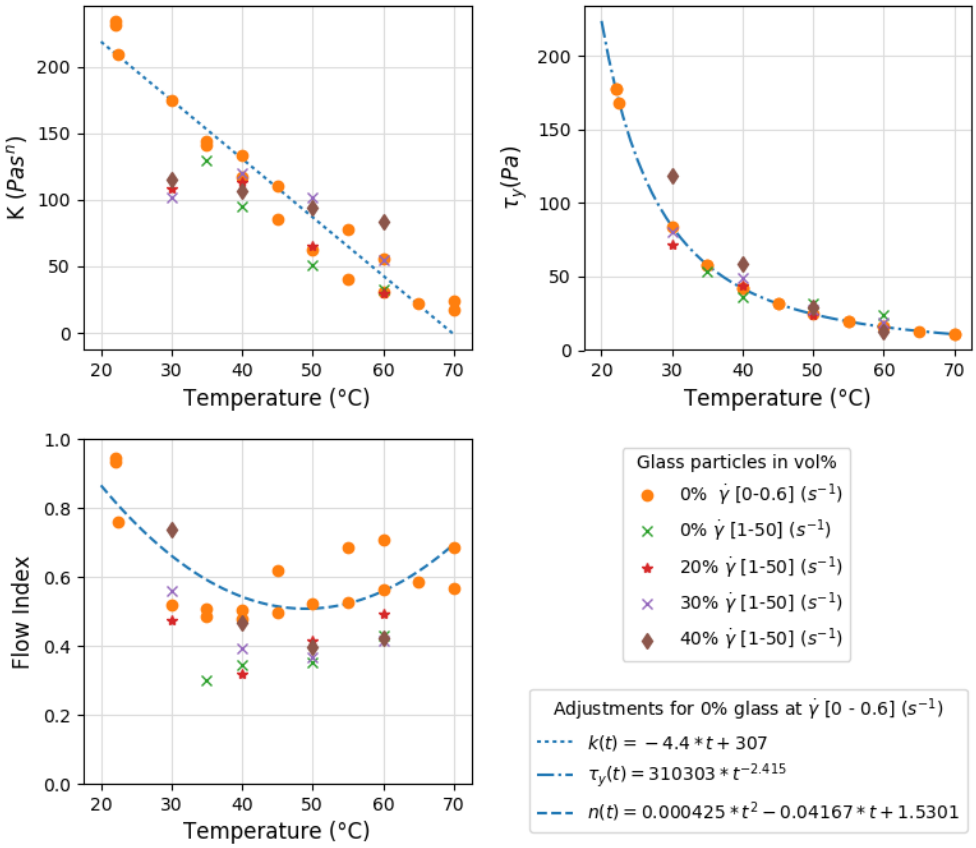

Figure 3.9: Here presented is Figure 3.8 plus rheological measurements obtained for manjar plus glass particle mixtures at higher strain rates.

The summary of consistency, flow index and yield strength obtained for all manjar measurements at four different temperatures and mixtures are shown in Table 3.3.

Table 3.3: Rheological data obtained from concentric rheometer of manjar at different temperatures and glass particle concentration

Measuring temperature ℃	**Glass beans** %	**Ty** (Pa)	**K** $(Pa\ s^n)$	**n**	$\dot{\gamma}$ (s^{-1})
35	0	53,3	130	0,303	[0-50]
40	0	36,5	95	0,346	[0-50]
50	0	31,7	51	0,353	[0-50]
60	0	23,8	32	0,432	[0-50]
40	0	42,0	134	0,506	[0-0.6]
45	0	31,6	110	0,619	[0-0.6]
55	0	19,4	78	0,688	[0-0.6]
60	0	15,8	55	0,710	[0-0.6]
70	0	10,9	24	0,685	[0-0.6]
70	0	10,9	17	0,567	[0-0.6]
65	0	13,0	22	0,587	[0-0.6]
60	0	15,8	31	0,564	[0-0.6]
55	0	19,4	41	0,529	[0-0.6]
50	0	24,5	62	0,522	[0-0.6]
45	0	31,6	85	0,497	[0-0.6]
40	0	42,0	117	0,478	[0-0.6]
35	0	57,9	144	0,510	[0-0.6]
35	0	57,9	141	0,485	[0-0.6]
30	0	84,1	175	0,519	[0-0.6]
22,5	0	168,4	209	0,759	[0-0.6]
22	0	177,8	231	0,934	[0-0.6]
22	0	177,8	235	0,946	[0-0.6]
30	20	71,8	109	0,476	[0-50]
40	20	43,8	114	0,321	[0-50]
50	20	23,6	65	0,416	[0-50]
60	20	15,2	30	0,492	[0-50]
30	30	80,5	102	0,559	[0-50]
40	30	48,8	120	0,394	[0-50]
50	30	27,4	102	0,367	[0-50]
60	30	18,4	54	0,416	[0-50]
30	40	119	115	0,740	[0-50]
40	40	58,4	106	0,469	[0-50]
50	40	28,9	94	0,399	[0-50]
60	40	12,9	83	0,422	[0-50]

Resulting rheogram for manjar at strain rates from 0.1 (s^{-1}) to 0.6 (s^{-1}) is shown in Figure 3.10.

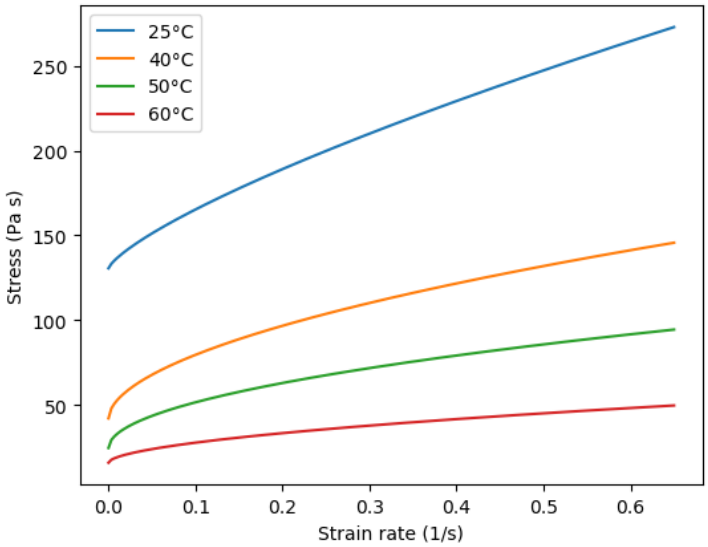

Figure 3.10: Manjar 0% glass particles, temperatures from 30°C to 60°C.

3.2.3 Relevant properties of lavas and analogue materials

With all gathered data and bibliography, a summary table of analogue materials properties relevant for studying the dynamics and final morphology of flows is compared with corresponding properties for silicic and basaltic lava compositions.

Table 3.4: Physical constants for lava flows of different compositions, glucose syrup and manjar.

Constants		Basaltic flows[a]	Silicic flows[a]	Wax-kaolin slurry	Syrup	Manjar
ρ	$(kg\ m^{-3})$	2700	2200	1450	1438	1340
μ	$(Pa\ s)$	10^2-10^4	10^5-10^{10}	0.78	10^5	10^5
τ_y	(Pa)	$0 - 10^4$	$10^4 - 10^6$	84	0	12 - 148
k	$(Pa\ s^{n-1})$	1 - 10^7	$10^8 - 10^{10}$	-	-	28 - 358
n		0.5 - 1	0.4 - 1	1	1	0.44 - 0.66

3.3 Scaled models of lava flows

A total of 33 experiments were carried out in the Laboratory of Experimental Volcanology in Laboratoire Magmas et Volcans of Blaise Pascal University, Clermont-Ferrand, France.

3.3.1 Experimental apparatus

The experimental device consisted of a manual system made of acrylic pieces simulating a syringe with a piston controlled by a crank with a screw that pushed the material in out of the reservoir through a plastic hose up to a flat and smooth inclined acrylic surface where extrusion took place as shown in Figure 3.11. This device was low cost, low maintenance and easy to use and clean considering the water soluble material for modeling the flows.

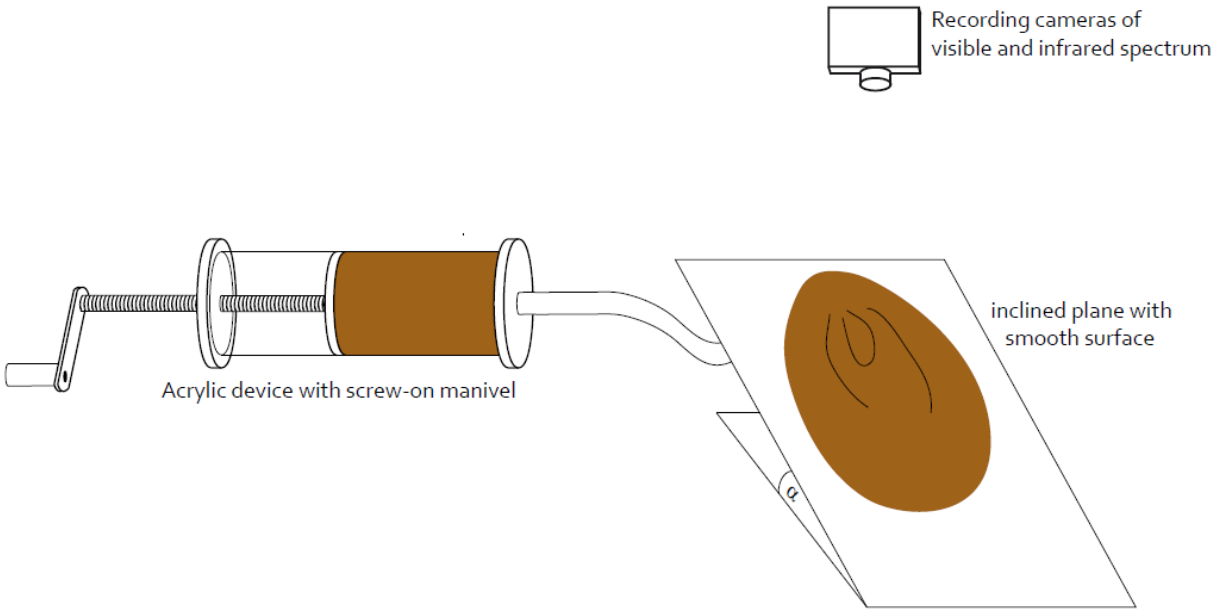

Figure 3.11: Sketch of the experimental device

Experiments were recorded from above with visible spectrum camera as video of 30 fps and an infrared camera as shown in Figure 3.12. Two different cameras were used for recording the visible spectrum videos according to availability at the time of performing the experiments. For most videos a Canon camera model DSC-HX7V recorded MTS files with dimensions of 1920 x 1080 pixels with a bit-rate of 16 Mbps. The second camera was a Nikon D3300 with a 18-55 mm Nikkor lenses, recorded MOV files with dimensions of 1280x720 pixels with a bit-rate of 20 Mbps. The infrared camera was a Forward Looking Infrared thermal imager system (*FLIR*) Thermacam 650 and recorded 22 of the 33 experiments carried out. *FLIR* system operates in 7.5 - 13 μm spectral range and records a 640x480 pixels image in which temperature is the output for each pixel in seq files. Temperatures registered from the *FLIR* camera are corrected with: 1) in situ humidity and air temperature measurements set with a portable weather station, and 2) distance between the camera and the flow at the beginning of each experiment. Image emissivity was set to 1. A number of experiments have type-k thermocouples data in the extrusion point or in 10 (cm) steps from this point directly downslope. Slopes were set to 15° for the first 5 experiments and 10° for the remaining. The volume of material extruded was set constant, a total of 2 (kg) of manjar per experiment with a volume of approximately 0,00143 (m^3) that was re-used for up to three times, but mostly twice. Specific settings for all experiments are indicated in the tables from section 4. Manjar density used for all calculations measured at 23℃ is 1340 (kg/m^3).

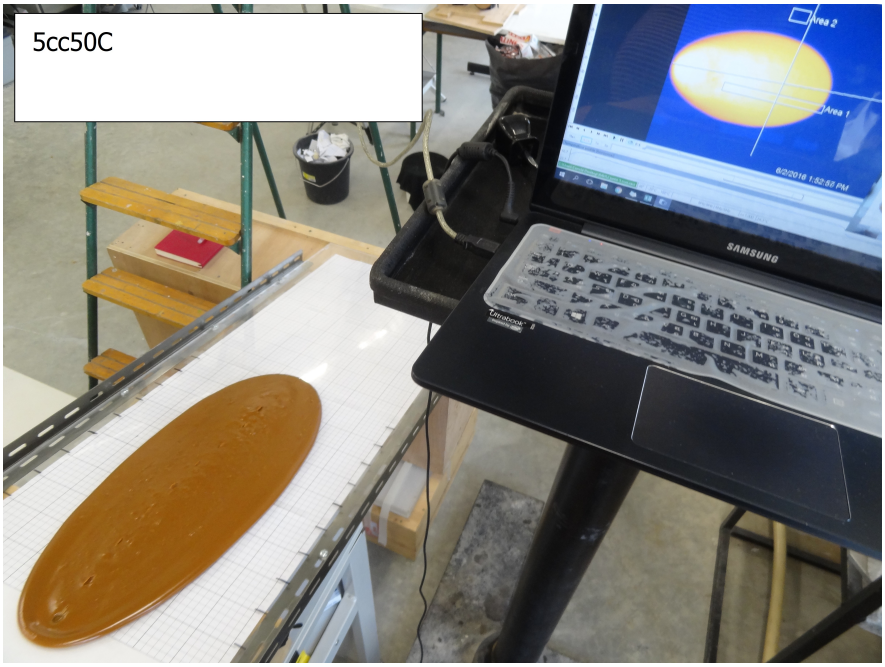

Figure 3.12: Perspective view of experimental setup with ongoing flow of 5 (cc/s) and initial temperature of 50℃. On the top right the notebook connected to the *FLIR* camera shows live recording of flow temperature, white area represents hotter material and yellow to orange the cooler material. On the left bottom, the flow in the inclined channel with a 15° slope moves slowly until it reaches the steady state. The extrusion point is on the left lower corner of the image and the downslope extent reaches out to the center of the picture.

The sketch in Figure 3.13 shows a map and side view of the flows, identifying relevant corresponding distances measured, nomenclature that will be used further in this work. The dynamical evolution of the flows is given by the spreading of manjar from the extrusion point, used as the origin of the reference system, with downslope length denoted as X_{max}, upslope length as X_{min} and the maximum cross-slope length as Y_{max}. Total length is considered as downslope plus upslope length.

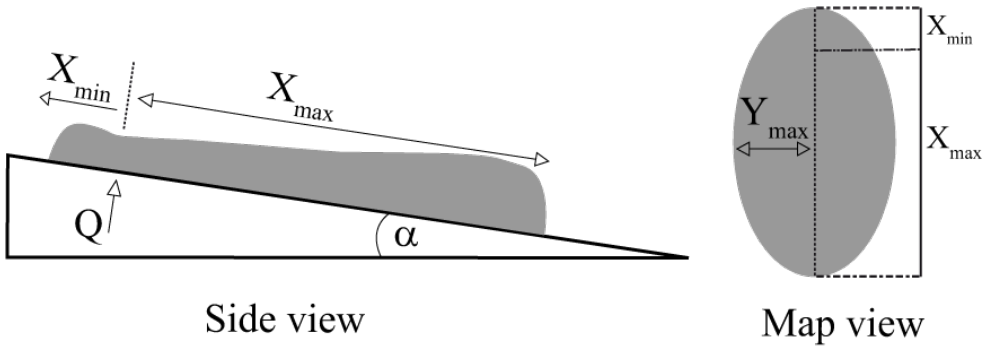

Figure 3.13: Sketch of flow geometry and concepts used for describing the temporal evolution of the flow. Image modified from Cordonnier et al. (2016).

3.3.2 Material extrusion

A total of 4 different flow rates were used: 1, 5, 10 and 25 (cc/s) which led to extrusion times from 2.4 to 26.4 (min). This extrusion times, ζ_Q are used in the following chapters with the corresponding values as shown in table 3.5.

The manually controlled handle pushed 2mm of material in the reservoir of 4.6 (cm) of diameter in every 360° turn. Desired flow rate, Q, calculated with equation 3.8 shows v is velocity and A the transversal area where the flow gets through. The area of the reservoir is estimated from the inner diameter, 9.2 (cm).

$$Q = vA \tag{3.8}$$

The needed velocity for the lowest flow rate is 4.5 turns of the handle in 1 minute. For maintaining a constant velocity a metronome was set to 18 beats per minute and by each beat the crank was moved in 90° or one quarter of a turn. The same procedure is followed for determining each of the metronome beats per minute to obtain the desired flow rate with resulting velocities shown in table 3.5.

Table 3.5: Breakdown of flow rates and estimated velocities with corresponding crank turns for obtaining a constant supply of material.

Q (cc/s)	**velocity** (mm/s)	**bpm**	**turn** °	ζ_Q (s)
1	0.15	20	90	1430
5	0.75	45	180	290
10	1.5	90	180	145
25	3.75	112	360	70

3.3.3 Thermal settings

In order to determine the effects of cooling on the resulting flows, two types of experiments are made: cooling and isothermal. Given the temperature dependent rheology of manjar, cooling flows evolve with distance and time from extrusion continuously, which according to measurements implies an increasing consistency and yield strength with temperature and a decreasing flow index. A similar evolution is thought for lava flows, although there are more variables into this process such as crystallization, degassing, differences in strain and more, which makes it far more complex. Still, this is a good attempt at recreating this rheological evolution considering the Herschel Bulkley model and has not been previously used in reviewed literature for this thesis. The isothermal flows are given by two experiments that had no previous heating and were directly put in the reservoir from the package that was stored at room temperature in the same area as where the experiments were carried out. These flows had extrusion rates of 1 and 10 (cc/s), and a non-Newtonian rheology that is considered constant throughout the experience.

3.3.4 Data acquisition

Flow velocities were estimated from visible spectrum videos with PotPlayer by determining the frame in which the flow reached the rules installed below the acrylic surface the flow was ejected in. The rules were drawn every 1 (cm) and bolder lines were placed every 5 (cm). This was done with downslope and upslope distances. The cross slope distance was measured by determining the widest transversal distance and then divided by two. As seen in the pictures in the following chapters, the nature of manjar and the deep brown color that characterizes it, along with the range of viscosities that shows for the temperatures chosen, allows for very accurate determination of distance in time with a setup like this, with clear margins and convenient velocities well captured by the camera.

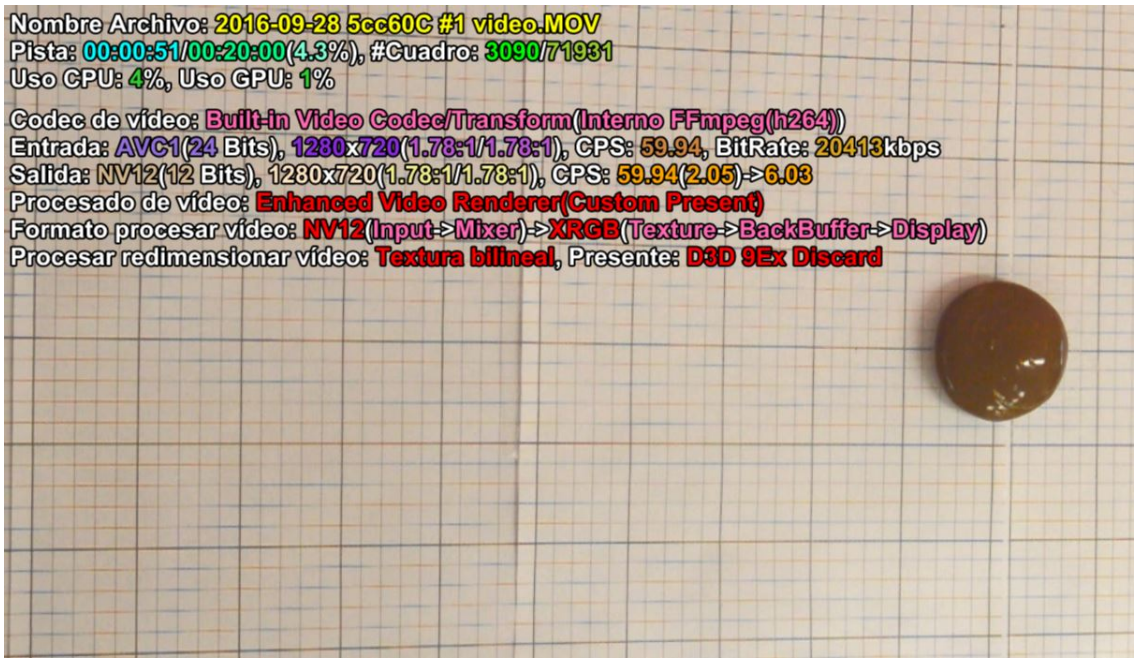

Figure 3.14: Screen caption of the software used in video analysis

In regard of thermal imaging, flow temperatures from the .seq files are exported to .xlxs files with the corresponding software of the *FLIR* camera, in order to be filtered by the minimum temperature of the flow and only consider the hot surface of the flow, from which it possible to obtain a series of selected measurements that will be shown in the following chapter.

3.3.5 Flow geometry estimates

Acquired data through both thermal and regular videos allows for estimating approximate values of maximum flow depth in time, assuming the volume of the flows represent half an ellipsoid, with an ellipse as basal area where total volume can be obtained due to the constant flow rate in time. As shown in Figure 3.15, the longitudinal extent is represented by 2 b, the transversal extent by 2 a and maximum depth or thickness by c. The volume of half the ellipsoid is represented in equation 3.9.

$$V = \frac{2}{3}\pi abc \tag{3.9}$$

There are two methods for estimating basal area of the flow in order to estimate the maximum thickness in time. First, based on the advance of the flows from visible video recordings as follows. The cross slope measure in time represents the smaller axis, a, while half the downslope plus upslope extent represent the longer axis, b. With these two axes it is possible to estimate a basal area of the ellipsoid according to equation 3.10

$$Area = crossslope\frac{(downslope + upslope)}{2}\pi = ab\pi \tag{3.10}$$

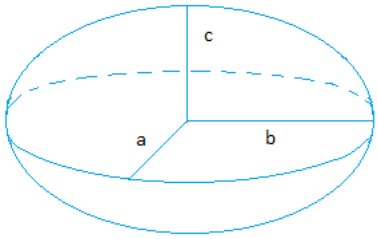

Figure 3.15: Reference diagram of an ellipsoid, b represents the mayor radius, a the intermediate and c the minor. Notice the scaling of the diagram may differ from the values discussed in this section.

The second method consists in estimating the ratio between the total number of pixels read beyond a filter temperature for each frame of the thermal image, eliminating the background of the image which represents cold smooth inclined surface over which it is being poured, and the number of pixels that correspond to 1 (m^2) estimated for each video, with an average value of 1020100. The result is the basal area of the flow, that is approximated as the basal area of an ellipsoid.

With estimates of basal area of the flows in addition to known volume extruded in time, we use geometry to estimate maximum heights in time, with the assumption that c axis represents this value. The $FLIR$ images result in data that follow a continuous and smooth evolution in time, because of the resolution given by one frame per second video, but are available for a limited number of experiments performed, and compared to the other method where data was acquired manually for every 1 (cm) of advance of the flows is much denser. The evolution of areas and heights in time obtained by different methods are compared for the same experiment in the Results section in **Chapter 4**.

3.3.6 Digital elevation model

With the Structure from Motion technique it is possible to obtain a 3D imaging estimate from a sequence of 2D images that are coupled with a software. This tool is used to obtain digital elevation model, *DEM*, from the resulting flows from pictures taken when the fluid seems to be static and presents no further motion. Pictures are taken with the needed specifications

by the software used, Agisoft PhotoScan. With the *DEM* obtained as shown in the Results section in **Chapter 4**, relevant information can be acquired, in this case it is important to determine if the flows present structures similar to those defined in lava flows like the central channel, leveés and more.

Chapter 4

Results

The experimental matrix consisting of 33 experiments is shown in Tables 4.1 and 4.2, indicating the set of initial conditions for each experiment and type of data gathered, whether *FLIR* video is available, type of thermocouples measurements and other observations. Each experiment can be referred to individually with the corresponding name shown in these tables, and are composed of extrusion rate plus the maximum measured initial temperature of material.

Evolution data was gathered from video recordings for each of the flows from the beginning of material extrusion until the flows presented no motion for a given period of time. Given the very viscous behavior of manjar, it turned out that for the majority of the flows the video recordings ended prior to the absolute end of motion, because velocities were so low that bare eye could not distinguish any movement at all. For 11 out of 33 experiments the last measured velocity registered is equal to zero, fact that we use as criteria for determining the flow reached a standstill. For the remaining 22 experiments registered data does not show the complete evolution of the flows until material came to a halt, having final velocities larger than zero, with the largest final velocity measured being $8,4 \times 10^{-5}$ (m/s). For this reason, the lengths shown for mentioned experiments cannot be assumed as final, likewise flow thicknesses, although cross-slope and upslope stabilize early and reach their maximum lengths for most experiments. Corresponding information about distances versus time will be used only for retrieving relevant dynamical data and estimated ratios between mentioned values in case the experiment presents final velocities larger than zero.

Resulting flows show similar and regular geometries with well defined perimeter. Total flow lengths range from 0,2 (m) to 0,7 (m), with maximum widths from 0,24 (m) to 0,31 (m), and maximum depths from 0,014 (m) to 0,028 (m), which lead to aspect ratios from 0,04 (m) to 0,1 (m). The final shape of the flows can be approximately described by half an ellipsoid with the basal area of an ellipse, as indicated in **Chapter 3**, with the longest extent found throughout the downslope direction. Textural classification described in Tables 4.1 and 4.2 was made based upon three qualities shown in all experiments: luster, lumpiness and porosity. Despite the classification, these qualities showed no relation whatsoever with controlled factors for each experiment such as flow rate, initial temperature or times of use. There are observable bubbles in a number of experiments that are thought to be a product of pouring manjar in the reservoir with little care, although given the high viscosity of the

material there was small chance of avoiding the formation of bubbles in settings as the one used. There is an example of these bubbles in Figure 4.1, showing a close up image of the flow front for one manjar experiment where elongated bubbles can be seen as a result of differential strain and stress states in the outer regions of the flow.

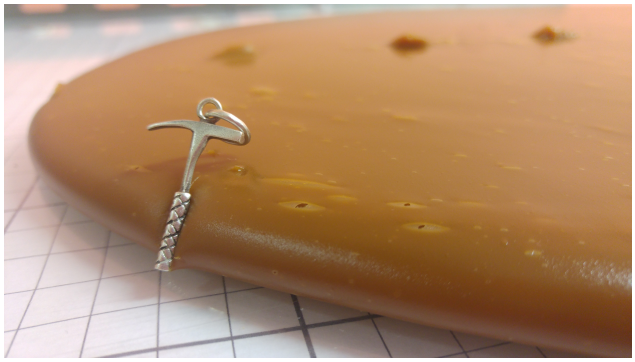

Figure 4.1: Close up of the flow front of manjar. It shows smooth edges and elongated bubbles due to strain. Small hammer of 3 (cm) length for scale, and the square grid on the surface represents an area of 1 (cm^2) per square.

In order to ease data view from the following sections, all experiments are presented with a color legend that corresponds to a different shade of red, referring to a certain thermal range indicating maximum initial temperature as stated in their name. When figures are composed by markers, each marker corresponds to a different flow rate and experiments performed on slopes of 15° are either colored black markers or use a dotted line with the corresponding shade of red according to initial temperature, depending on the type of chart. This is valid for all figures that involve a number of experiments plotted, as shown in Figure 4.2. Most figures present the mentioned legends, although in some cases legend has been omitted but follows the same considerations. In case the figure presents the evolution in time of any property of the flows, these considerations do not apply. In this case each figure presents a legend identifying all variables plotted.

(a) Color legend

(b) Markers legend

Figure 4.2: Color and marker legend used in this work.

Table 4.1: Experimental conditions for flow rates of 1 and 10 (cc/s).

Name	V_{final}	**Thermocouple**	**Slope**	**Observations**	**Texture**	#	U_m	t_{max} (^oC)
10cc24C	0	no	10,5	no flir data	smooth, lumpy	25	1	23,8
10cc49C	3,1E-05	extrusion point	10	-	smooth, porous, lumpy	15	1	49,6
10cc50C	0	four points	10,5	-	smooth, porous	31	2	50,2
10cc55C	0	no	10,6	-	smooth	22	1	55
10cc57C	0	no	10,3	-	smooth, porous	24	2	57
10cc59C	3,4E-05	extrusion point	10	-	smooth, porous	12	2	59,9
10cc60C	8,4E-05	no	15	no flir data	smooth, lumpy	4	1	60
10cc67C	2,4E-05	extrusion point	10	-	smooth, lumpy	11	1	66,6
1cc24C	1,6E-07	no	10,5	-	smooth	23	2	24,1
1cc47C	6,9E-05	extrusion point	10	-	smooth, lumpy, porous	7	2	46,7
1cc48C	0	no	10,5	no dynamic data	smooth, porous	28	1	47,5
1cc51C	0	no	10,4	-	smooth, porous	29	2	51
1cc52C	7,2E-07	four points	10,2	very viscous stored manjar	rough, lumpy	33	1	52
1cc54,7C	0	four points	10,4	very viscous stored manjar	rough, porous	32	1	54,7
1cc54C	7,4E-05	no	15	no flir data	smooth, lumpy	2	1	54
1cc55C	6,6E-05	extrusion point	10	-	smooth	8	1	54,4
1cc59C	4,3E-05	no	10	no flir data	rough, lumpy, porous	6	3	58,9
1cc62C	5,7E-05	extrusion point	10	flir data too big	rough, lumpy, porous	17	3	61,6

Table 4.2: Experimental conditions for flow rates of 5 and 25 (cc/s).

Name	V_{final}	**Thermocouple**	**Slope**	**Observations**	**Texture**	#	U_m	t_{max} (^oC)
25cc50C	1,3E-05	extrusion point	10	material loss in the first seconds	smooth, porous	21	2	50,4
25cc54C	9,5E-06	no	15	no flir data	smooth	3	2	54
25cc58C	1,7E-05	extrusion point	10	-	smooth	9	2	58
25cc60C	2,4E-05	no	15	no flir data	smooth, lumpy	5	2	60
25cc62C	2,0E-05	extrusion point	10	no flir data	smooth, lumpy	16	2	62,1
25cc70C	2,4E-05	extrusion point	10	-	smooth	10	1	69,7
5a25cc56C	1,7E-05	extrusion point	10	PLOT	smooth, lumpy	19	1	55,8
5cc48C	0	four points	10,5	-	smooth, porous	30	1	48
5cc50C	2,8E-05	no	15	no flir data	smooth, lumpy	1	1	50
5cc53C	1,5E-05	extrusion point	10,2	-	smooth, porous	18	-	53,1
5cc55C	0	no	10,2	-	smooth, porous	26	2	55,1
5cc57C	0	no	10,1	-	rough, lumpy, porous	20	1	56,9
5cc58C	0	no	10,2	-	smooth	27	1	58
5cc59C	3,9E-05	extrusion point	10	-	smooth, lumpy	14	1	58,6
5cc63C	2,8E-05	extrusion point	10	flir data too big	smooth, lumpy	13	1	63,1

4.1 Description of flow regime and dimensions obtained

According to Balmforth et al. (2002), the initial regime of the flows should be controlled by the growth of an axisymmetric flow until gravity takes effect and extends the downslope direction further, stabilizing the cross-slope moments after the upslope. A few experiments present initial evolution with very noticeable axisymmetric growth, like 1cc54,7C or 10cc55C. The great majority shows erratic behavior in the initial phase of the extrusion, with variable velocities and non-related slopes. This is particularly notorious for experiments with the highest flow rate, 25 (cc/s), where complete extrusion of material was over in less than 3 minutes. The crank had to be moved faster in these experiments, in order to reach a high velocity extrusion, causing small variations in flow rate, reflecting all distances versus time slopes with sudden changes and irregularities. Temporal evolution of the flows is shown in detail for a number of experiments in Figures 4.3 and 4.4 for all experiments that reached their maximum lengths in Figures 4.6, showing data gathered for X_{max}, X_{min} and Y_{max}. The vertical line shows the time ζ_Q, the end of material extrusion, and the pink point represents (t^*, L^*), a transition point that is recognized in all flows as the point where the dynamical regime of the flows slows down remarkably and which happens to occur near ζ_Q for most experiments, specially those that undergo cooling, as will be discussed further in this chapter and the following. Dotted colored lines in Figures 4.3 and 4.4, represent the power law fit that can be adjusted to each curve, the fit prior to ζ_Q corresponds to the early time regime, where the majority of experiments approach their transition point at highest velocities. It is followed by the long time regime. Upslope and cross-slope lengths have already been stabilized and downstream continues to develop further at low velocities until reaching their run-out length.

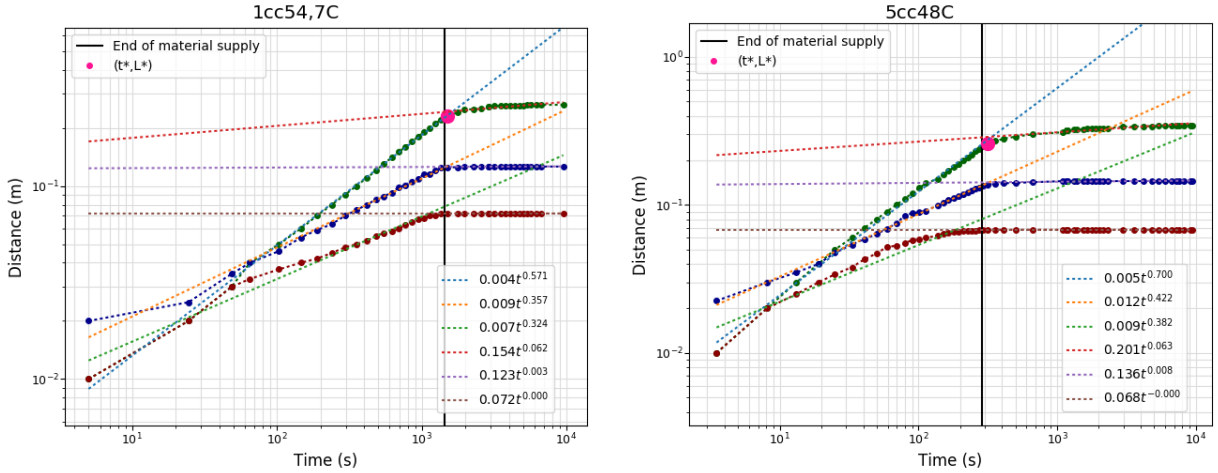

(a) Experiment 1cc 54,7℃.

(b) Experiment 5cc 48℃.

Figure 4.3: Example of power law fit in experiments for X_{max} in green markers, Y_{max} in blue markers and X_{min} in dark red markers.

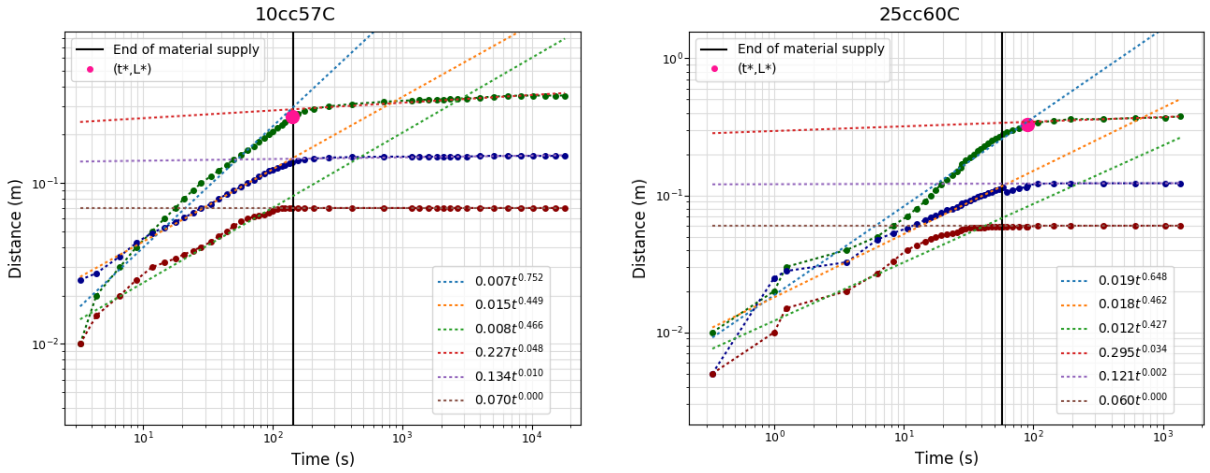

(a) Experiment 10cc 57℃.

(b) Experiment 25cc 60℃.

Figure 4.4: Example of power law fit in experiments for X_{max} in green markers, Y_{max} in blue markers and X_{min} in dark red markers.

Resulting power law exponents for the early phase regime, prior to the transition point, obtained for all flows are presented in Figure 4.5, with detail for upslope, cross-slope and downslope extent, which represent the exponent to obtain the curves shown with blue, yellow and light green pointed lines in Figures 4.3, 4.4. According to Tables 2.2 and 2.1 our experiments lay in between of all mentioned time regimes and do not accurately represent a single fit.

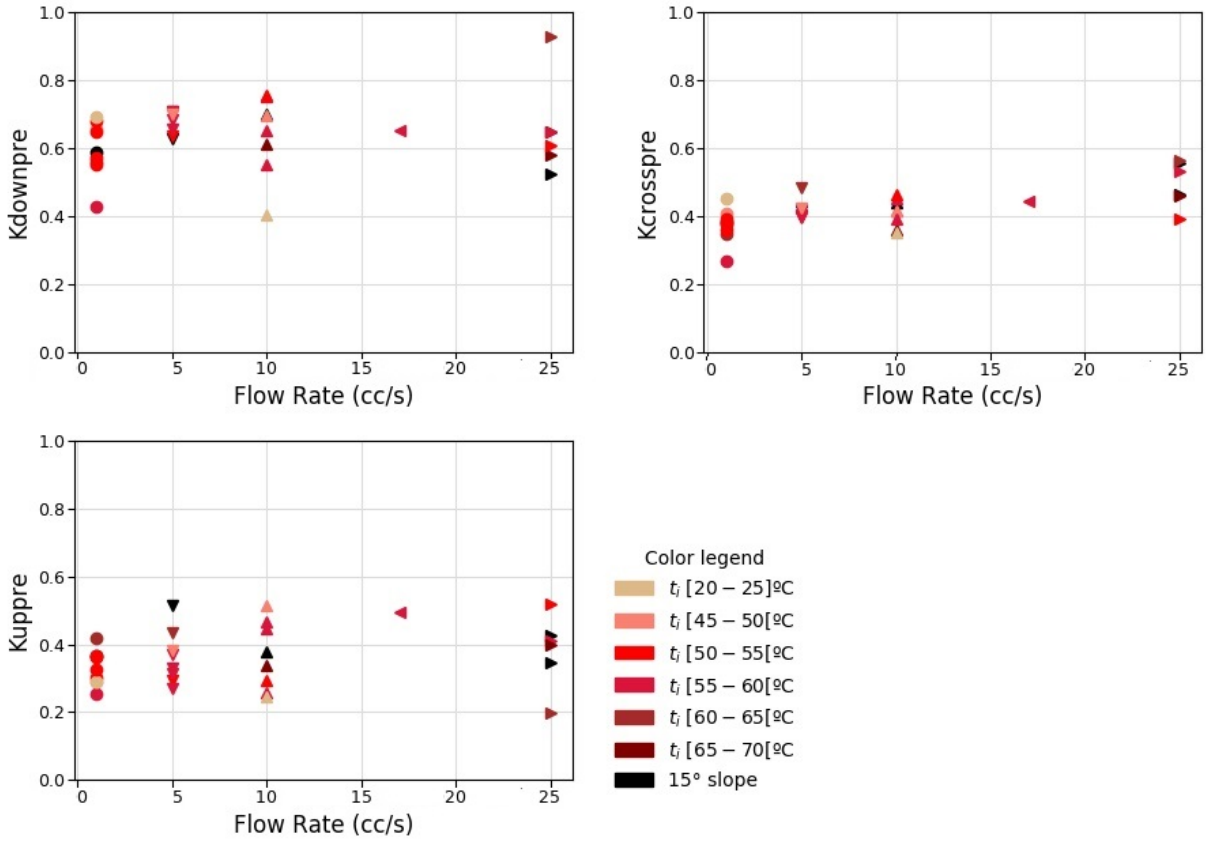

Figure 4.5: Time exponent for downslope, upslope and cross-slope lengths for early regime estimated from the first data point up until transition point.

The evolution in time for downslope, upslope and cross slope distances shown in Figure 4.6 are presented in green, blue, and deep red markers, respectively. The black vertical line represents the time when material extrusion is over, ζ_Q, and total volume of manjar is part of the flow. A pink round marker over the green line represents the transition time and length point defined as (t^*, L^*). The proximity between the black vertical line and the pink dot is part of the discussion topic regarding the difference between cooling and isothermal regimes, as the only flow that shows a great time difference between these events is experiment $10cc24C$. Also, these experiments also illustrate the fact that distance seems to follow a power law fit over time for most flows with a breaking point marked by the transition point (t^*, L^*).

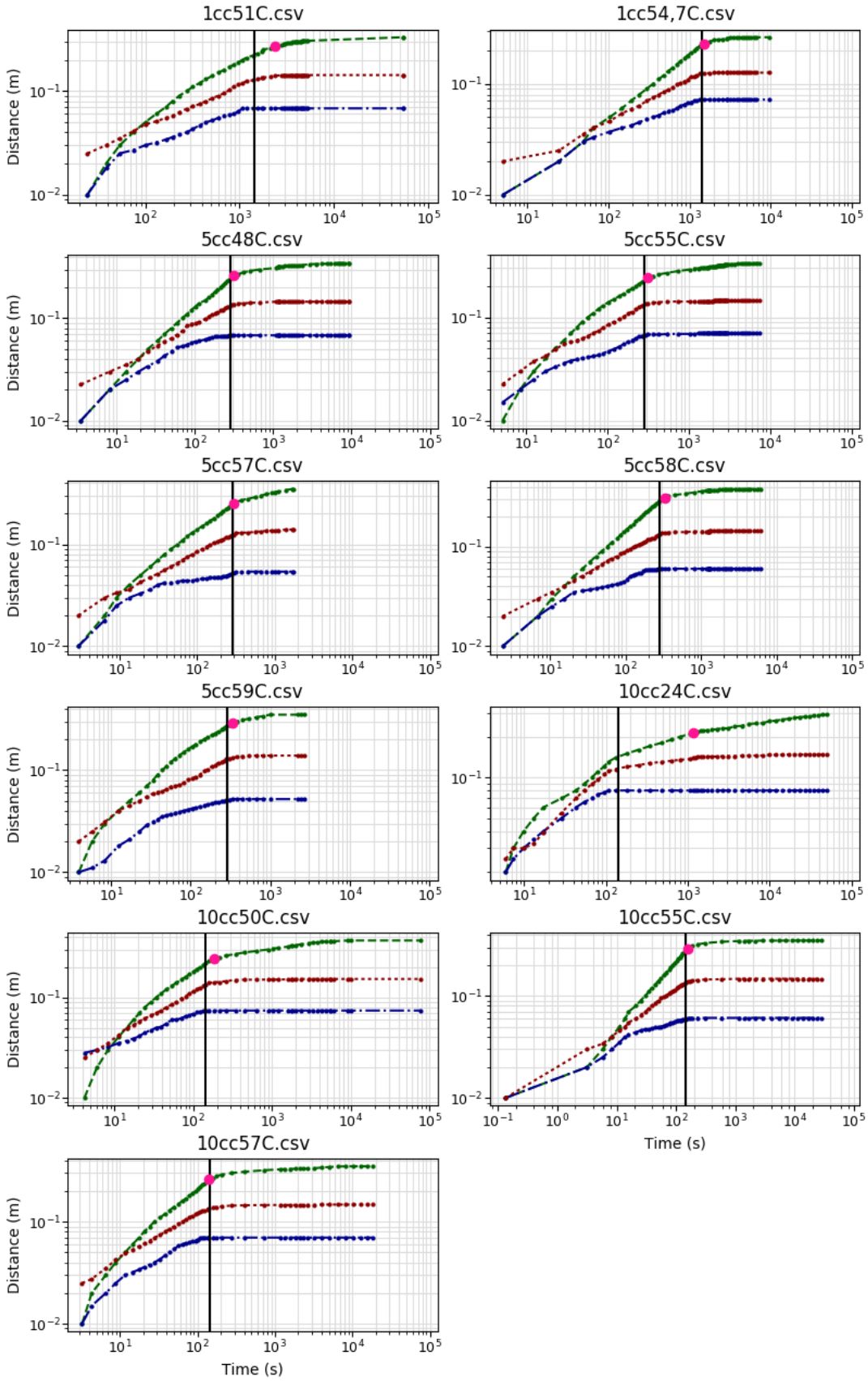

Figure 4.6: Resulting flow dimensions for experiments that reached maximum downslope lengths. Each name represents the experiment flow rate followed by initial temperature.

For one experiment a variable flow rate in time was achieved by increasing rate from 5 (cc/s) to 25 (cc/s) during extrusion,, as shown in Figure 4.7. This graph shows that dynamics are strongly controlled by flow rate as a sudden increase in flow rate presents as well, a sudden increase in velocity when trying to determine a power law fit to our data.

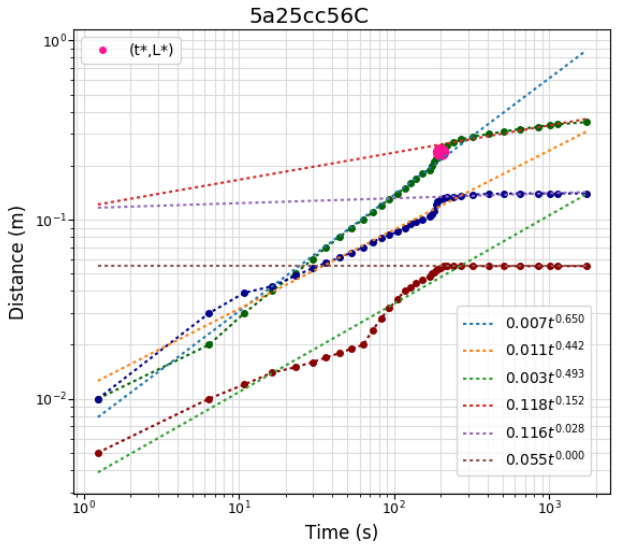

Figure 4.7: Dynamic evolution for experiment 5a25cc54C.

The velocity used for estimating dimensionless quantities, viscosities and other relevant parameters in this section was approximated with two approaches: V_1 as the slope between better-fitting points with the power law fit for the early time regime, also referred to as v_1. Secondly we have vel, which was estimated from the slope between the fifth point of X_{max} evolution until (t^*, L^*). Values of the fifth point of distance versus time were chosen arbitrarily by the author due to the stabilization of extrusion rates, eliminating the first distance versus time points measured that reflect small irregularities in flow rate due to manual extrusion. Both velocities are shown in Figure 4.8. It is evident that higher flow rate leads to higher velocities regardless of the estimation method, showing similar orders of magnitude for rates from 1 (cc/s) to 10 (cc/s). Experiments with rates of 25 (cc/s) show a larger range of velocities when estimated as V_1, while vel shows a collapse in velocity for most of 25 (cc/s) experiments.

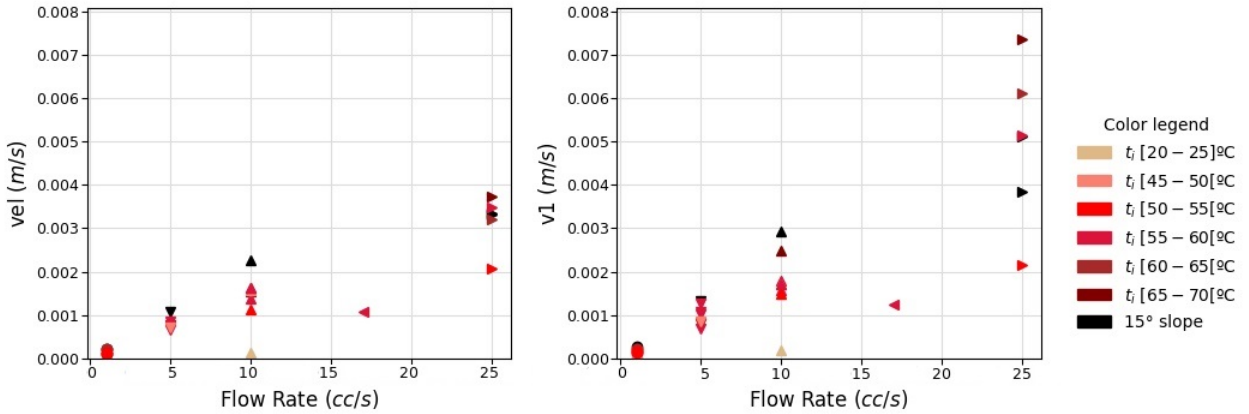

Figure 4.8: Estimated average velocities for X_{max} versus corresponding flow rate. Values of V_1 are estimated from slope between better fit between results and power law fit, while values of *vel* correspond to the slope between the fifth value of distance versus time and the transition point (t^*, L^*).

Next, we are able to compare how accurate our dynamic data is compared to the area registered by *FLIR* recordings. Figure 4.9 for each experiment that has *FLIR* data available the resulting total area of the flow in time given by filtering images as indicated in **Chapter 3**. This information is compared to the area approximation given by using X_{max}, X_{min} and Y_{max}, detailed in that same section. Purple points represent A_{FLIR}, and green points A_{dynamic}. Experiments with $V_{final} = 0$ are marked with an asterisk in the lower right end of each subfigure. For the first few points the evolution of basal area is most inaccurate for the great majority of the flows, probably due to manual retrieval of data points by video recordings, but for most flows after the first few centimeters of advance, areas are very similar until stabilization. There are several factors influencing the difference between curves, such as pixel count in *FLIR* video and manual retrieval of flow advance from video recording for estimating evolution in time. Experiment 5cc55C shows the greater inconsistencies between curves, with A_{flir} growing larger during early regime. For experiments with the highest flow rate we note the curves show different slopes as in 25cc50C and 25cc58C.

The evolution of the flows maximum depth is estimated for both basal area approximations just mentioned, which gives us ξ_{din} and ξ_{flir}, the maximum points as plotted in Figure 4.10. Given our methods, these maximum depths are reached at ζ_Q for each of the experiments. Grey lines represent maximum measured depth. Data from ξ_{flir} is presented in purple and ξ_{din} in green. The fit between curves is good for most experiments, although some experiments like 5cc55C, 5cc57C and 10cc67C show similar but scaled profiles for di$n$ data that translates in larger depths, coinciding with smaller areas shown in the previous figure. This is most likely due to scaling measurements with $FLIR$ images because of the similarity between profiles. For flow rates of 1 (cc/s), this figure shows great difference between final measured depth and estimated depths at times of 1500 (s), which is about 3 minutes after ζ_Q has been reached, for longer times the curves should approximate ξ_{d} just like experiments with larger Q shown in this figure.

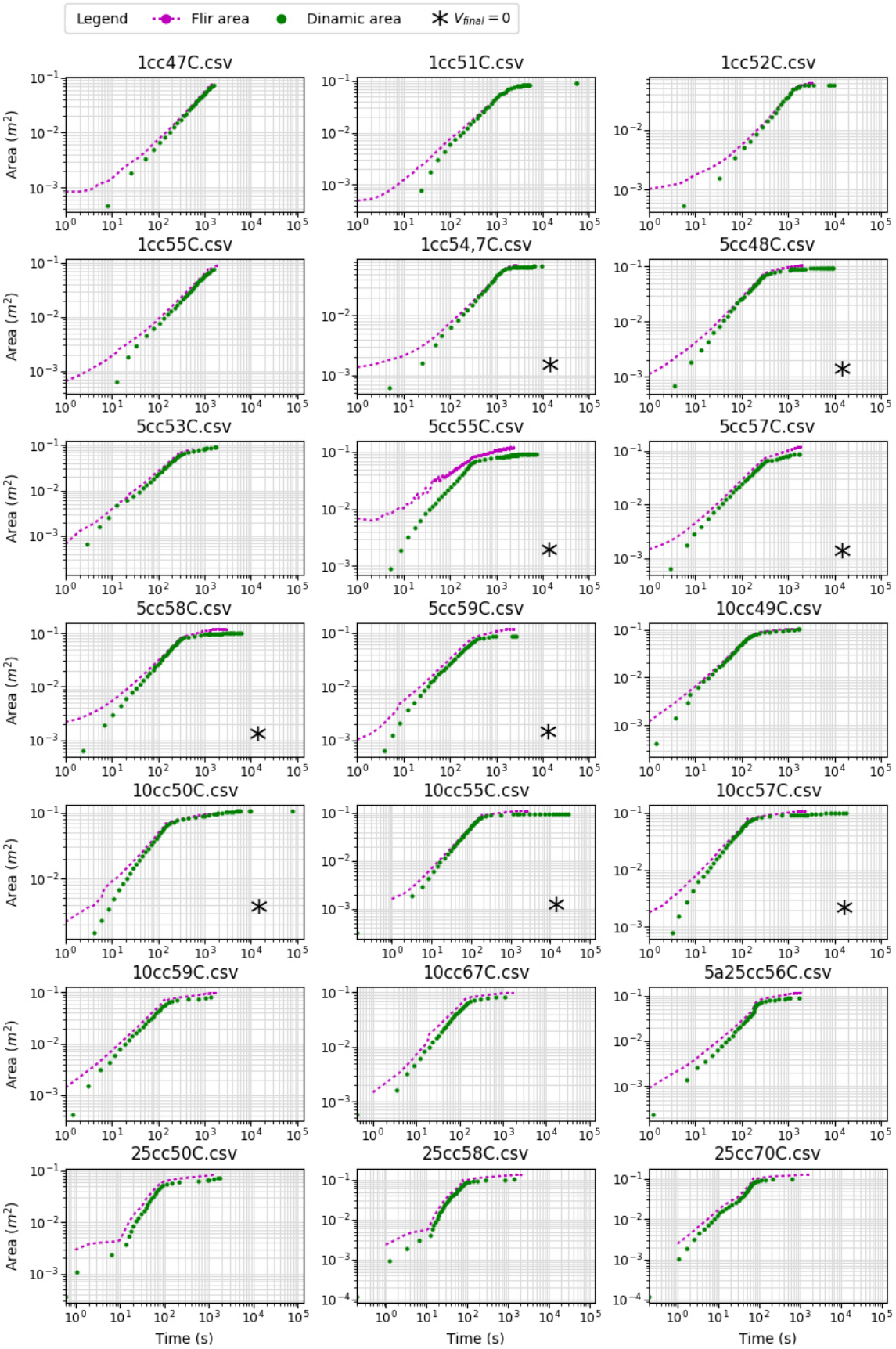

Figure 4.9: Area versus time for experiments with *FLIR* data plotted against estimated area with dynamic data. Purple dotted line represents *FLIR* values and green round markers show estimated area from dynamic data.

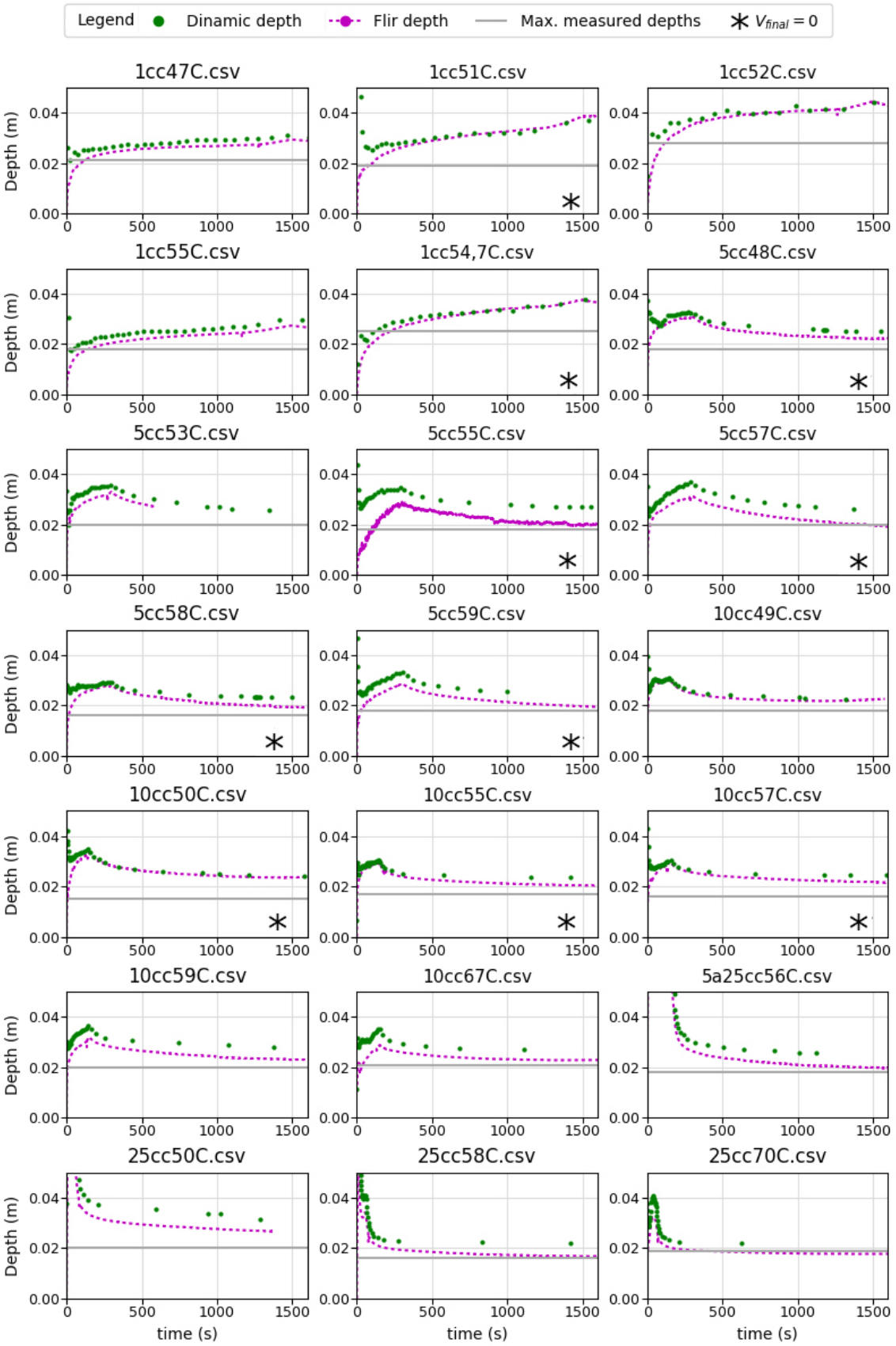

Figure 4.10: Estimated depth by *FLIR* and dynamic data. Purple dotted line represents *FLIR* values and green round markers show estimated area from dynamic data.

With estimated velocities and depths we found multiple definitions of flow deformation in time, as shown in Figure 4.11. Deformation rates with dynamic and *FLIR* data use the maximum depth estimated in time which occurs near the end of volume extrusion according to Figure 4.10 with velocities estimated from *vel* or V_1. A third value of deformation rate is estimated from final measured depth as well, represented in the charts on the right end of the figure. Deformation rates estimated with final measured depths are orders of magnitude larger than those estimated for maximum depths in time according to our geometric assumptions, and also seem to decrease as flow rate increases, showing that final measured depths for experiments with larger flow rates are smaller than those of lower flow rates. The opposite is found when using maximum estimated depths with *FLIR* or dynamic data. Between these four possible estimates and given that for each flow rate the deformation rates cover about the same orders of magnitude, regardless of velocity or depth estimate used, we find useful to stick to dynamical data because this information is available for all flows, unlike *FLIR* data that is only available for a number of experiments. We estimate both numbers mainly to compare the feasibility of our data gathering.

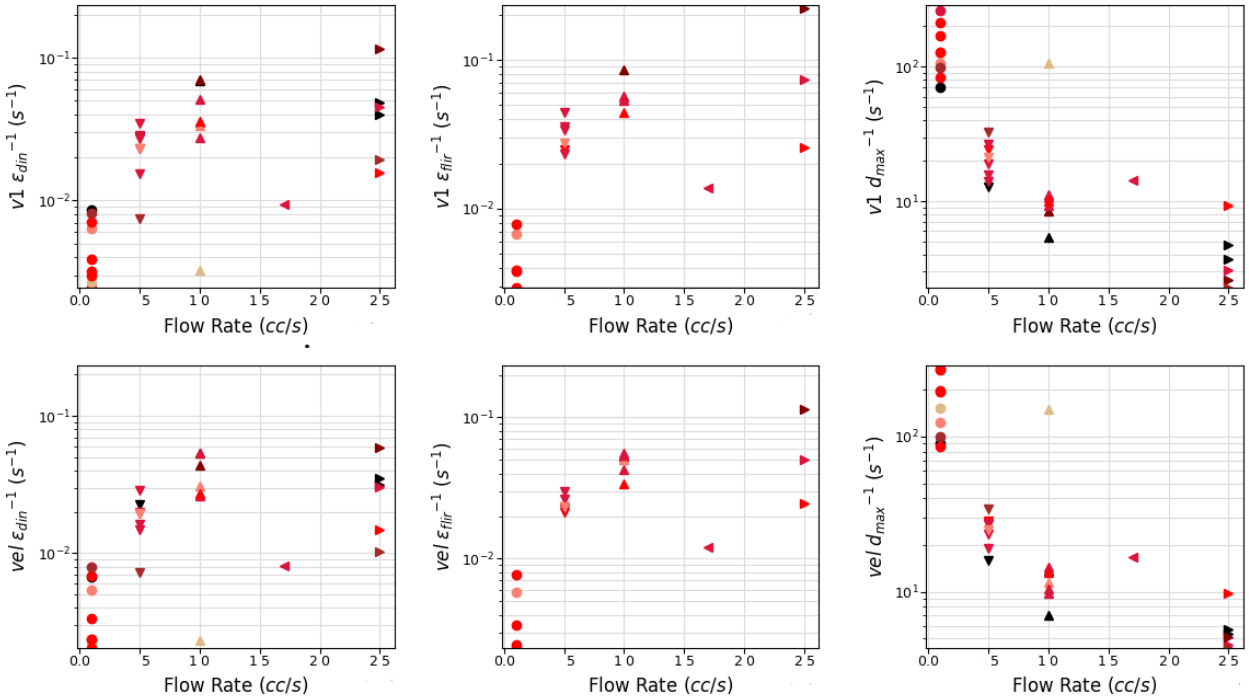

Figure 4.11: Deformation can be approximated by dividing a chosen velocity with its corresponding depth. For our experiments we have 3 possible depths to use with two estimated velocities.

Velocity and deformation estimates are used for different types of viscosity estimations. In Figure 4.12 all possible Jeffreys viscosities are shown, with velocities *vel* and V_1 and three mentioned depths. Viscosities estimated from final measured depths are smaller than those estimated with possible maximum depths previously shown.

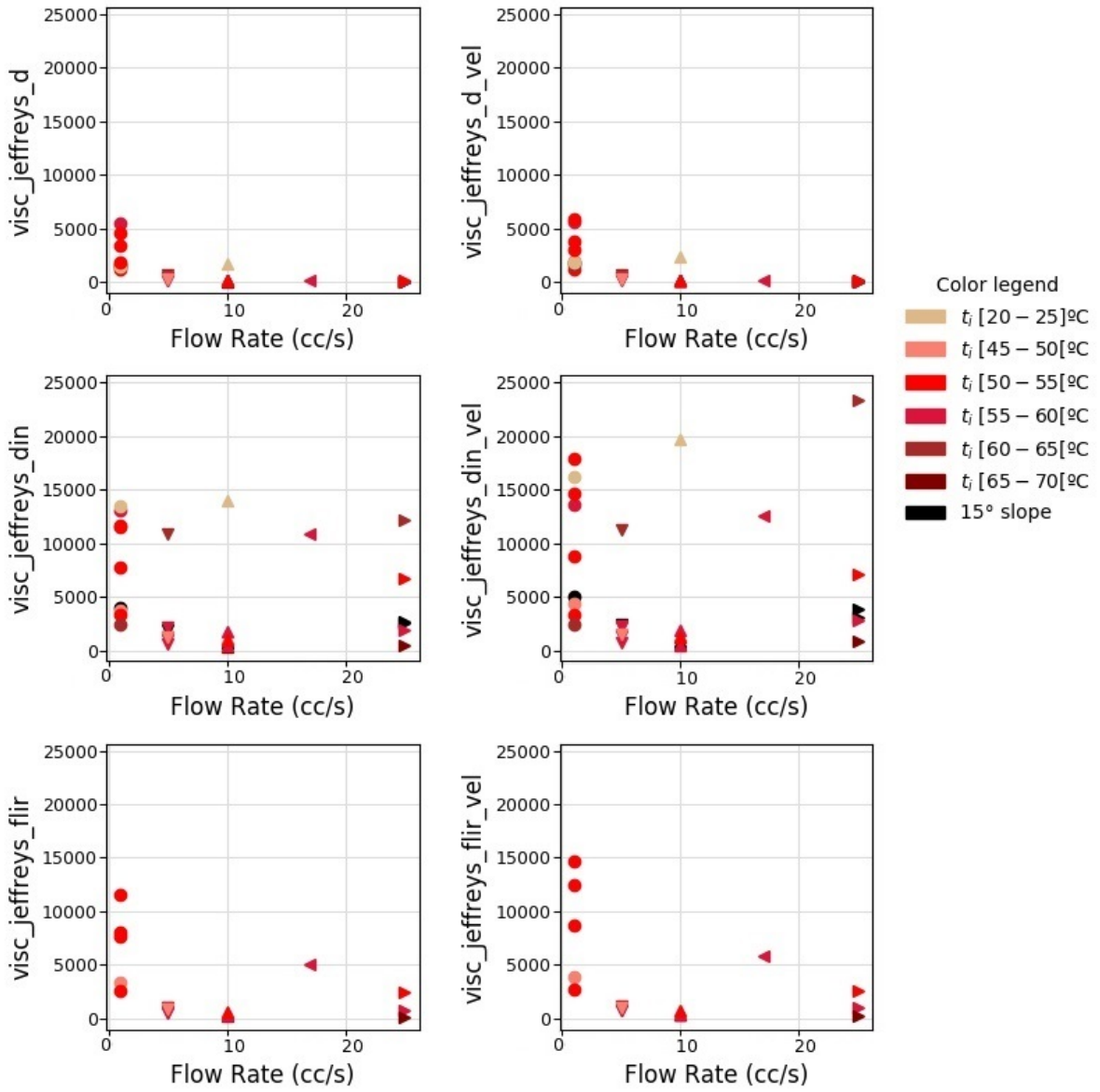

Figure 4.12: Estimated newtonian viscosities for velocities V_1 and *vel* with depths for *FLIR*, dynamic data and final measured depth.

Viscosities can also be estimated with rheological data available, given deformations from *FLIR* and dynamic data along with V_1 and *vel*, following the formula shown in equation 4.1.

$$\mu_{app} = \tau_y \gamma^{-1} + \kappa \gamma^{n-1} \tag{4.1}$$

Orders of magnitude remain similar even for different velocities, and once again it results convenient to consider dynamic data as it is available for all experiments.

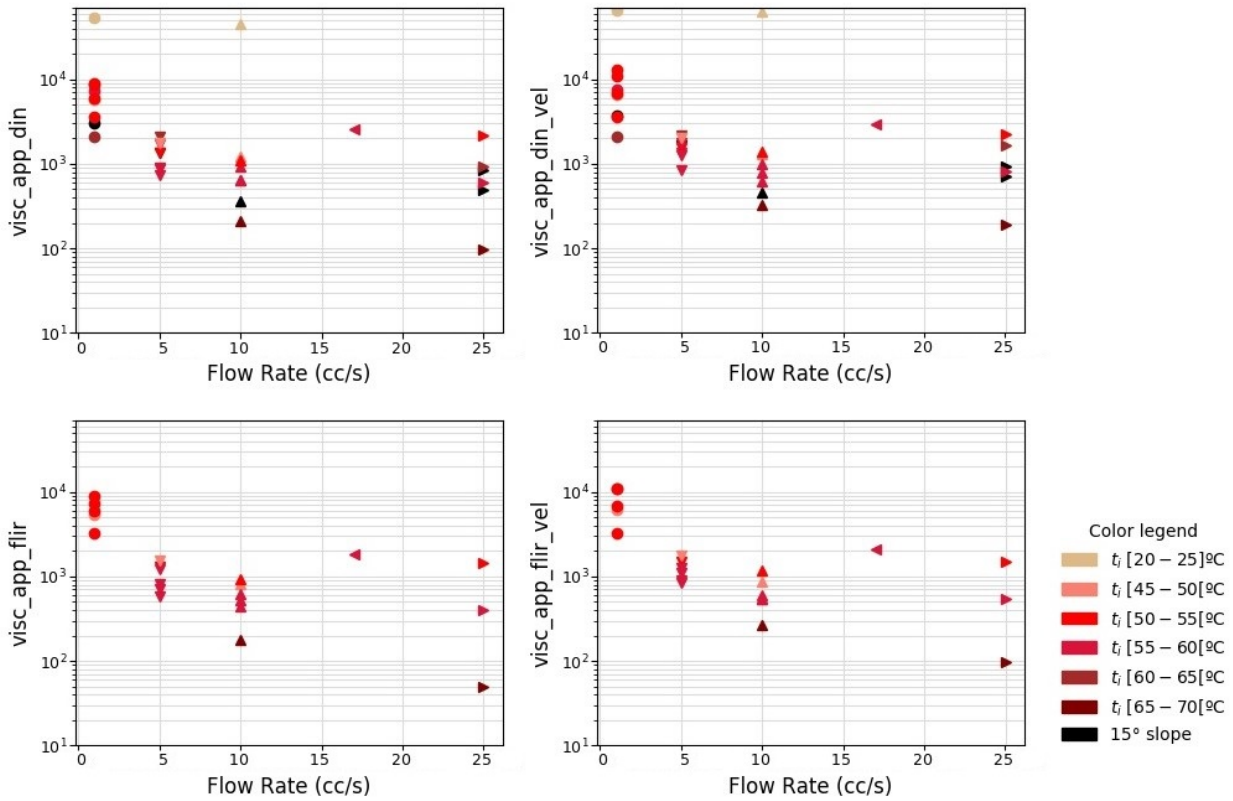

Figure 4.13: Approximated viscosities with rheological parameters at maximum temperature.

4.2 Trends with slope, flow rate and temperature.

Variation of slope and flow rate show important control over a number of flow features, involving final dimensions and relevant times of emplacement, for example, width stabilization time, revealing the auto-confinement stage. For this subsection, all experiments are plotted of a certain color that represents the initial temperature of the flow, even though results show it does not play a role controlling any geometrical or dynamic properties for our flows. The geometry of the markers indicate flow rate and black markers show experiments performed on a 15° slope.

Relevant lenghts and corresponding times of stabilization are shown in Figure 4.14. Experiments performed on higher slopes, represented by black markers, reach longer transition lengths and smaller upslope distances for flow rates from 1 (cc/s) to 10 (cc/s), while cross-slope distances are the shortest regardless of flow rate. Hence, slope plays an important role determining downslope advance of the material, with narrower widths and smaller upslope lenghts.

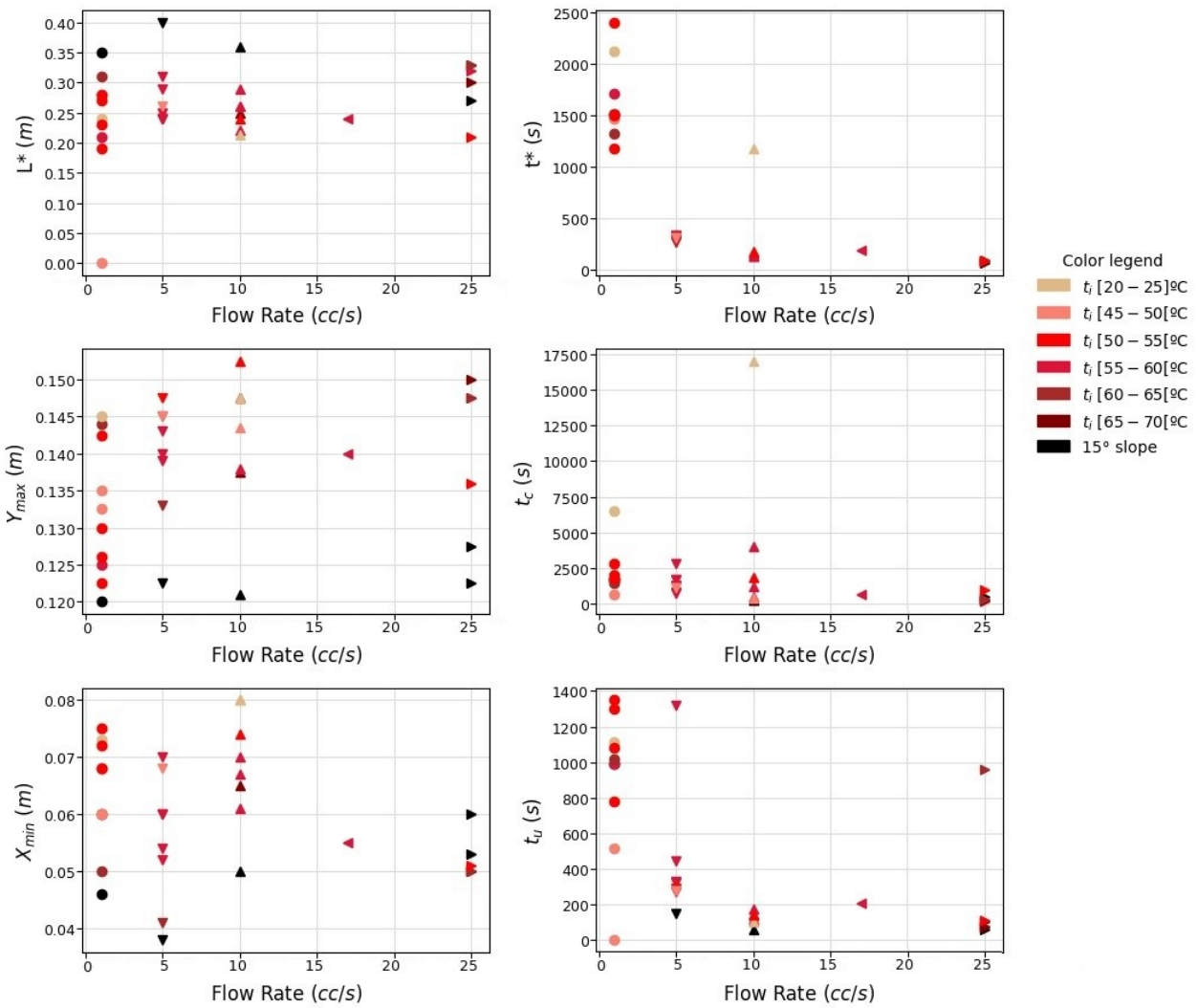

Figure 4.14: Corresponding relevant lengths, and times, for all experiments. Transition point (t^*, L^*), and maximum upslope and cross-slope lengths paired to their corresponding stabilization time.

The moment at which these lenghts reach their maximum distances are presented as t^*, t_c and t_u, and the detail of distance versus time allows for determining possibly different dynamical regimes of the experiments.

Transition point, (t^*, L^*), is shown in Figure 4.15. Straight vertical lines that represent ζ_Q for all flow rates. All experiments performed at higher flow rates, 25 (cc/s) reach their transition lenghts at times greater than ζ_{25}, hence continue to move at higher velocities during a period of time after all material has been extruded, regardless of slope. On the other hand, experiments with lower flow rates show transition times very similar to ζ_Q, determining the velocity of the flows is dependent of material injection, thus suddenly lowering the advance velocity once all material has been extruded.

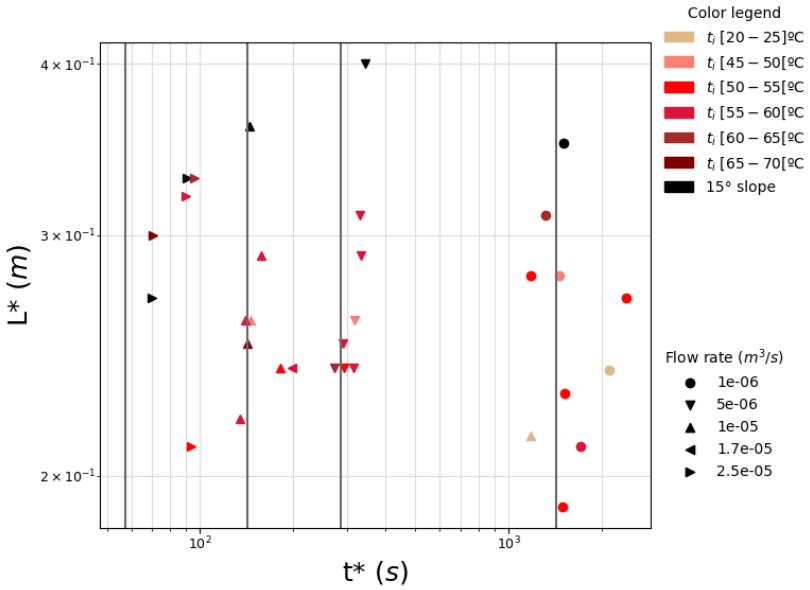

Figure 4.15: Detail of transition points for each experiment. Vertical lines represent corresponding ζ_Q for each flow rate used.

Figure 4.16 of maximum cross-slope length versus stabilization time, reveals that in isothermal conditions the spreading of the flows is slower regardless of the flow rate and continue to grow for longer periods of time, although maximum cross-slope lengths remain in the same scale than their cooling counterparts. It also reveals slope plays an important role in auto-confinement, or channelization, as flows stabilize their maximum cross-slope lengths at smaller distances but around the same time as their lower slope counterparts, growing mostly downwards.

All maximum upslope lengths are present in the same range value regardless of flow rate on Figure 4.17. Higher flow rates reach this lenght at shorter times, determining an axisymmetric regime that ends sooner than their higher Q counterparts, but still at longer times than their ζ_{25}, meaning the flow continues to spread axysimmetrically even after all material has been extruded. For Q from 5 to 10 (cc/s), the spreading occurs until their corresponding ζ_Q approximately. The opposite occurs for slower flow rates of 1 (cc/s), where upslope lengths are reached prior to ζ_1 and remain stable even though material extrusion is still on course.

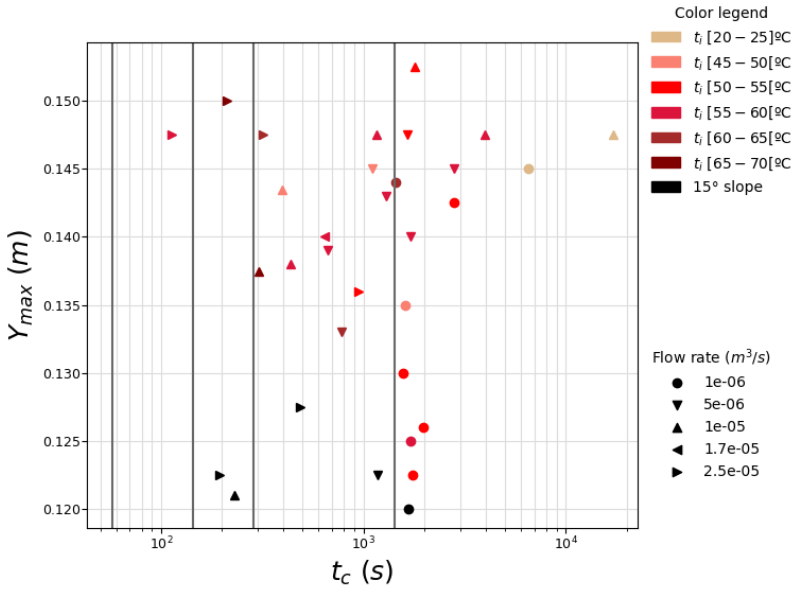

Figure 4.16: Detail of maximum cross-slope lengths measured versus corresponding stabilization time for each experiment. Vertical lines represent corresponding ζ_Q for each flow rate used.

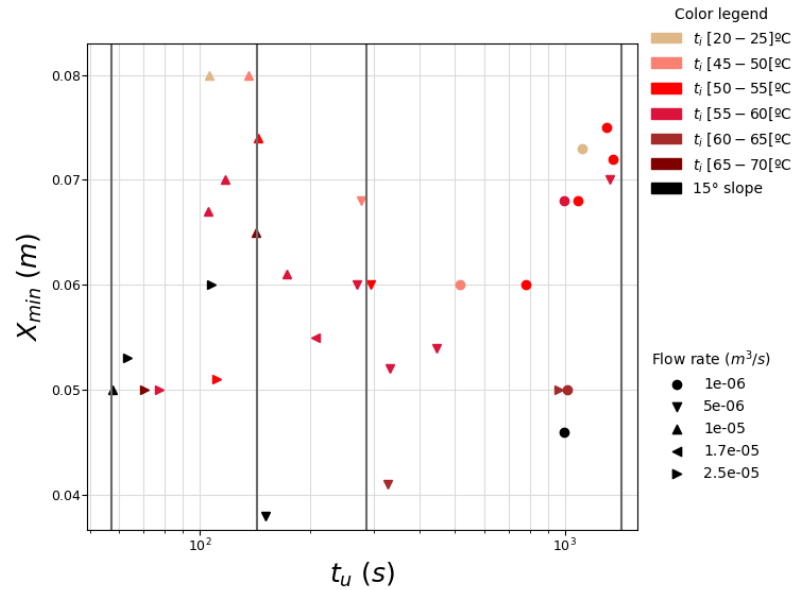

Figure 4.17: Detail of maximum upslope length versus corresponding stabilization time for each experiment. Vertical lines represent corresponding ζ_Q for each flow rate used.

When comparing flow dimensions, the ratio between transition and final measured downslope lengths, on Figure 4.18, shows that higher slopes result in larger ratios. On the other hand, lower flow rates, represented with circle markers, present larger transition lengths with respect to x_{max} when compared to higher flow rates, which show smaller transition lenghts for similar x_{max} lenghts.

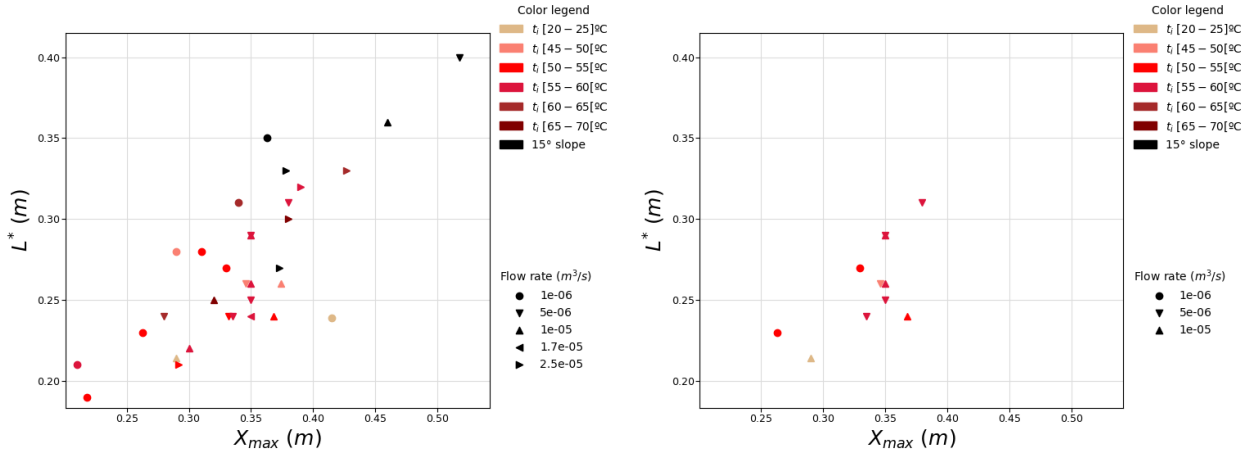

(a) Transition length versus maximum measured X_{max} for all experiments

(b) Transition length versus maximum measured X_{max} for all experiments with $V_{final} = 0$

Figure 4.18: Transition versus final X_{max} lengths measured for all experiments in figure a) and for experiments with $V_{final} = 0$ in figure b).

The ratio found for upslope versus downslope distances shows a number of clusters in Figure 4.19. First, higher slopes have the shortest upslope lengths with further downslope development, as previously mentioned in this section. Second, there is a cluster of experiments of all temperatures and flow rates that fall within the same range of upslope and downslope distances, and finally, five experiments with Q of 1 (cc/s) seem to have very similar ratios between these distances.

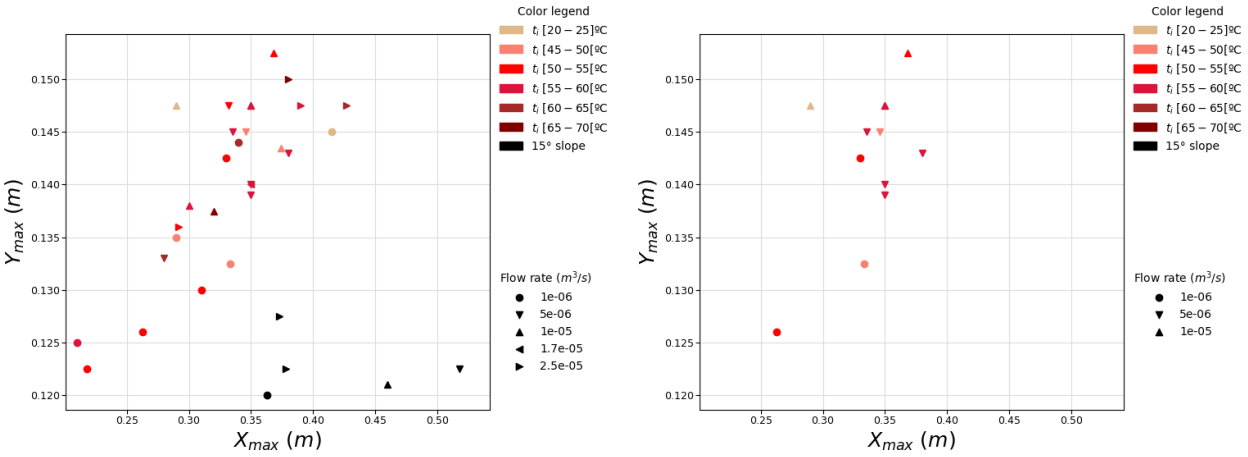

(a) Maximum downslope versus cross slope lengths for all experiments.

(b) Maximum downslope versus cross slope lengths for all experiments with $V_{final} = 0$

Figure 4.19: Maximum downslope versus cross slope lengths.

The influence of flow rate in final dimensions of the flow shown by our experiments lays

mostly in the aspect ratio given that final lengths do not determine any tendencies, and shows that lower flow rates translates into vertical growth, showing smaller cross-slope lengths and higher depths, while higher flow rates reach greater cross-slope lengths with lower depths, hence lower aspect ratios. Detail shown in Figure 4.20.

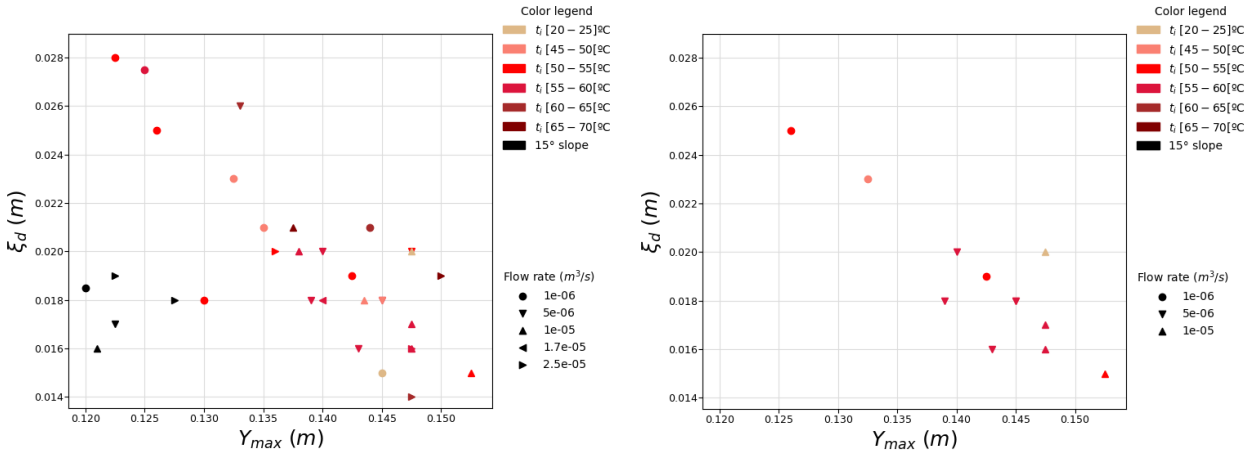

(a) Maximum downslope versus cross slope lengths for all experiments.

(b) Maximum downslope versus cross slope lengths for all experiments with $V_{final} = 0$

Figure 4.20: Final aspect ratio of the flows, maximum measured depth compared to maximum widths. This graph contains data for all experiments, although some of them did not reach final lengths, meaning final depths here described could be even lower. Widths here indicated reached a stable and final value for all experiments.

Aspect ratio between maximum measured depth and cross-slope are shown in Figure 4.21. Although experiments show a persistent range of aspect ratios from 0.05 to 0.08 regardless of flow rate, for Q of 1 (cc/s) this ratio can go even higher, up until 0.11, following the same idea as the previous figure.

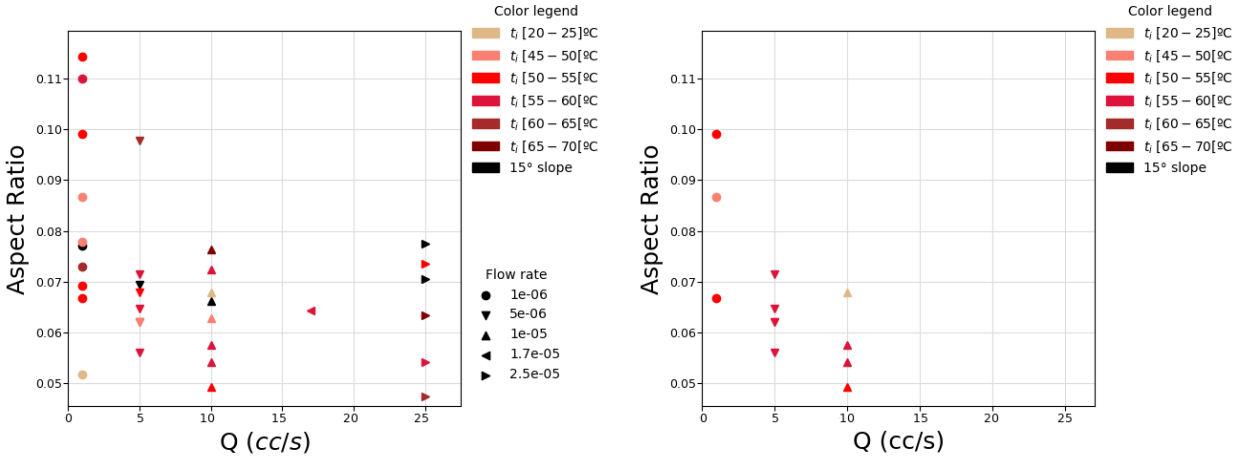

(a) Maximum downslope versus cross slope lengths for all experiments.

(b) Maximum downslope versus cross slope lengths for all experiments with $V_{final} = 0$

Figure 4.21: Final aspect ratio of the flows versus flow rate.

Final shape of the experiments indicates inflated flow front with a depressed zone in the extrusion point area. Measures of the longitudinal profile, from maximum upslope to downslope distance, going through the extrusion point, were made at the final stage of data gathering for each experiment. In Figure 4.22 are summarized all measured profiles for the 33 experiments grouped by flow rate. The extrusion point is represented by point 0,0 in the horizontal and downstream corresponds to the positive end of this axis. A number of experiments lack X_{min} measurements. Continuous lines show experiments with slopes of 10° and dashed lines represent experiments with slopes of 15°. For flows with Q of 1, 5 and 10 (cc/s) the maximum lengths are reached with higher slope of 15°, which are greater by almost 20% to 100% of total length for the remaining flows. For Q = 1 (cc/s) the maximum length is followed by the isothermal experiment. This isothermal experiment, we refer to it as 1cc24C, was left to spread overnight, it reached 0,41 (m) by 6,657 hours from extrusion and a total of 0,415 (m) by the last measure performed 15,296 hours from extrusion. We are not certain whether manjar spread continuously and slowly until the last measure or if it stopped somewhere in between. The shortest two experiments present in flow rates of 1 (cc/s) were performed with manjar that was stored in the laboratory for six months time in their sealed foil packages.

All experiments, except 3 found in the group of 1 (cc/s), present the same profile tendency with depressed depths in the vicinity of extrusion point and their thickest portion found near the right end of the axis which corresponds to the flow front portion of the flows. The three experiments that do not present this features are 1cc52C, 1cc54,7C and 1cc59C. The first two are also the shortest, also mentioned above as those performed with months stored manjar. The latter is manjar that was used by the third time as mentioned in Table 4.1.

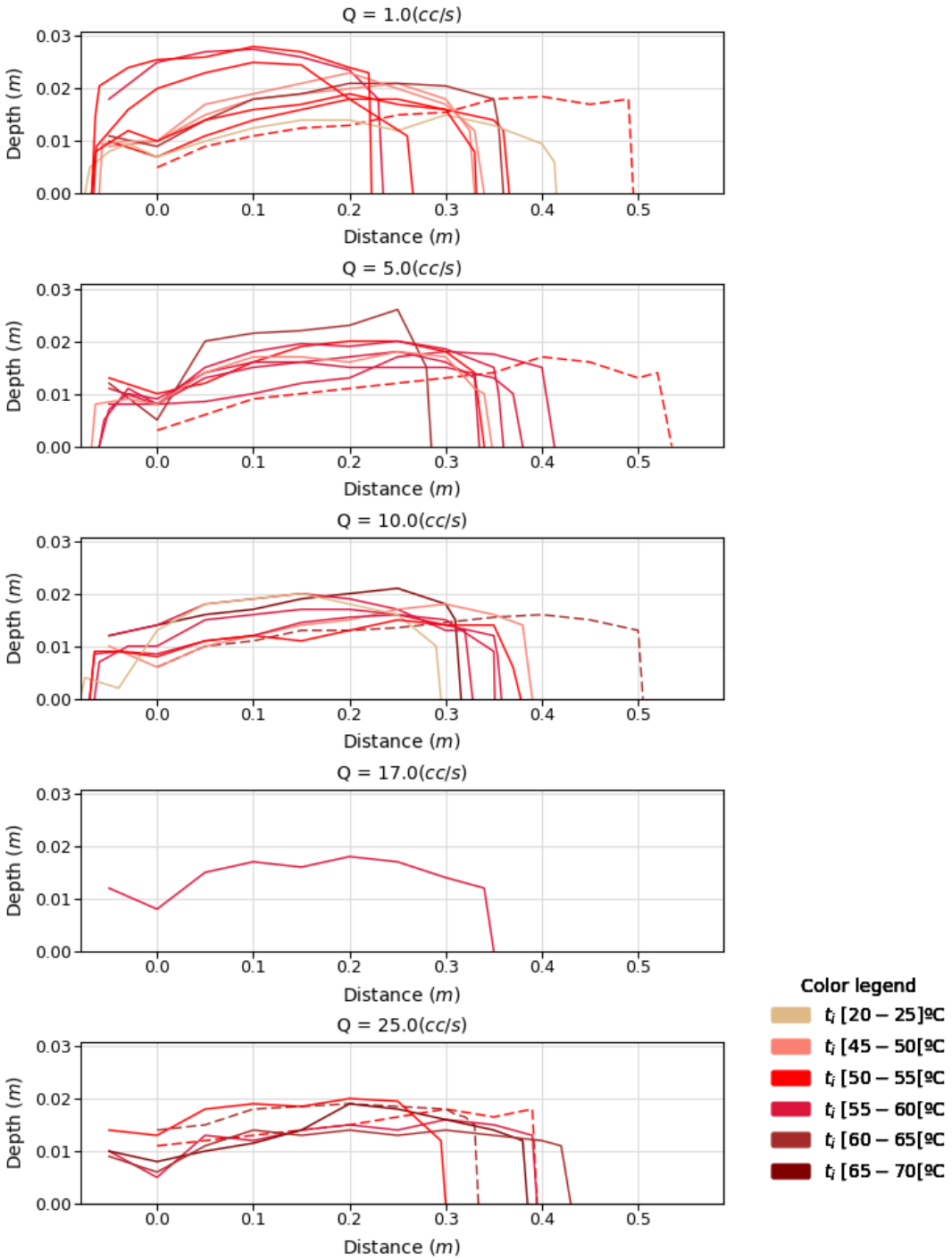

Figure 4.22: Final profiles for each experiment grouped by flow rate and colored by initial temperature. Axes are set to fixed values for all flow rates for ease of comparison. Flow rate expressed as 17 cc/s represents an increasing flow rate from 5cc/s to 25 cc/s.

As previously mentioned, manjar was re used for two or even three times when performing these experiments. Figures 4.23 show final cross and upslope distances and measured downslope length for all experiments against number of uses of the material. At a first glance, it appears that the number of uses of manjar could be narrowing the distance gap between

maximum and minimum values obtained in the first use. Trends with slope and Q seem to prevail in these figures, as maximum downslope distances are bigger for experiments performed on higher slope, while cross and upslope distances remain the shortest, independent of number of uses of manjar. For experiments on a 10° slope we find a possible homogenization of final lengths for manjar used twice due to narrower ranges found in upslope and downslope distances regardless of slope, temperature or flow rate, but we consider our information is not enough to determine this correlation. On the same note, experiments performed with re-used manjar for the third time remain in the same range of lengths reached by manjar used for the first time, which leads us to consider that properties of the material remain somewhat similar throughout all experiences.

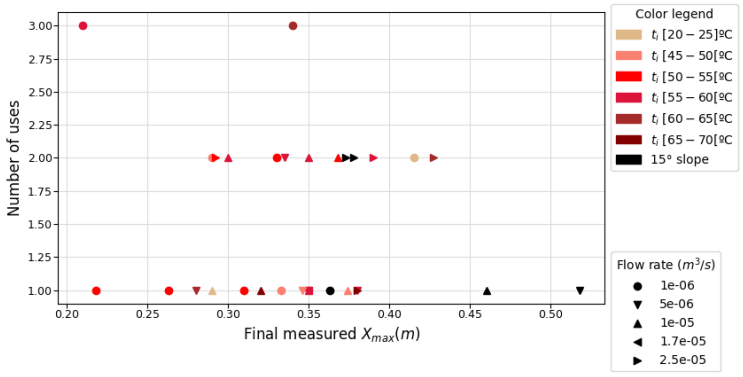

(a) Maximum downslope length measured versus number of uses of manjar.

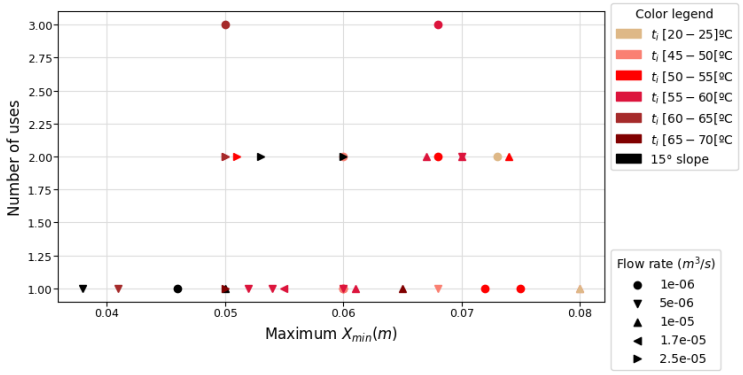

(b) Maximum upslope length versus number of uses of manjar.

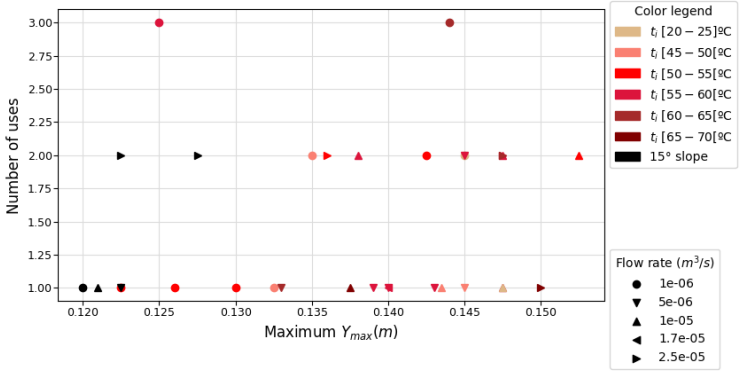

(c) Maximum cross-slope length versus number of uses of manjar.

Figure 4.23: Number of uses of manjar versus final measured lengths.

Textural classification for all flows has been already specified in the experimental matrix Tables 4.1 and 4.2, referring to a 3 stage state going from smooth and silky to rough and porous or lumpy surface, which could represent the breaking of manjar given that is a dairy product. Results shown in Figure 4.24 reveal that flows with smooth texture, 0, and rough and lumpy or porous, 2, present a range of lengths similar for all mentioned distances. It appears that texture smooth with porous or lumpy surface shows constrained lengths, with a small range of downslope and upslope distances, with larger cross-slopes. For Figure 4.24a, we must mention that the three experiments with shortest lengths presented with highest texture rating, 2, consist of the two experiments performed with long stored manjar and manjar used for the third time according to the previous graph.

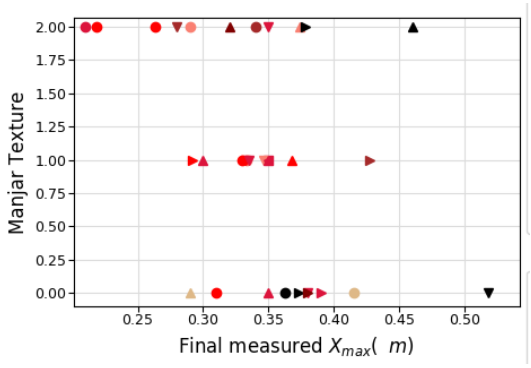

(a) Maximum downslope length measured.

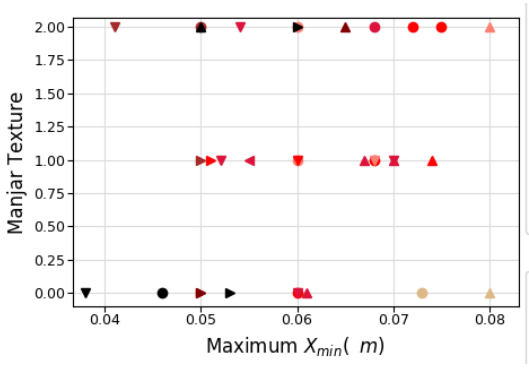

(b) Maximum upslope length.

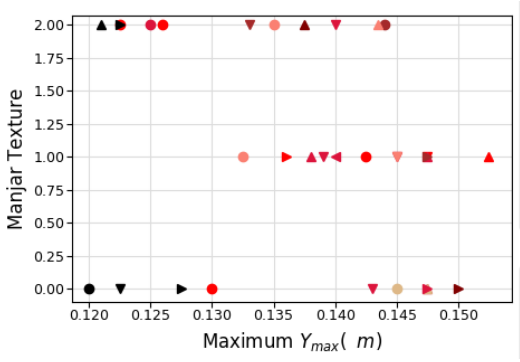

(c) Maximum cross-slope length.

Figure 4.24: Textural classification of flows versus versus final measured lengths. Values 0 represent smooth, 1 equals smooth plus porous or lumpy and 2 are rough plus porous and/or lumpy.

By the end of this Chapter, in Figures 4.42, 4.43, 4.44, and 4.45, pictures of each of the flows are available and these qualities are easy to observe, although qualification is made according to author perception. Throughout this section we have also noted that for the number of experiments we performed, with the characteristics here mentioned, the precise initial temperature of the flows does not pose an influence over any dimensional or dynamical feature here described.

4.3 Cooling and isothermal flows.

There are two types thermal recordings for the flows, FLIR measurements of surface heat variation in time for 22 of the experiments, and thermocouples with measurements of thermal evolution in different areas of some of the flows, recording inner temperature. Two experiences had no previous heating of the material, representing isothermal dynamics of the flow for constant flow rates of 1 (cc/s) and 10 (cc/s) as shown in Figures 4.25a and 4.25b. The thermal evolution of the flows is shown as an T_{index}, equation 4.2. Temperature index shows the amount of heat loss as shown in equation 4.2.

$$T_{\text{index}} = \frac{T_{measured} - T_{ambient}}{T_{max} - T_{ambient}} \tag{4.2}$$

With our data, we find relevant temperatures that will be presented as $T_{measured}$:

- from *FLIR* files: flow front, extrusion point, fixed point of choice.

- from thermocouples: extrusion point or fixed point of choice.

In Figures 4.26a and 4.26b the index is estimated from *FLIR* data. Two portions of the flow that represent different thermal states of the material are shown as purple and red line. The first is the ejection point, area, where new material is being supplied, reflecting reservoir temperature. The second area measured is the flow front, the portion of flow that holds the material that has been exposed to ambient conditions for longer time.

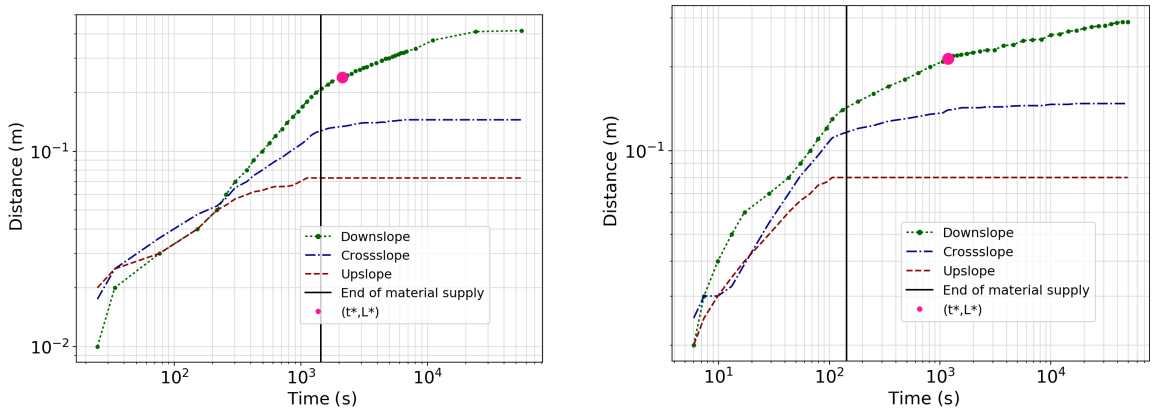

(a) Flow evolution for Experiment 22, 1 (cc/s) with isothermal conditions

(b) Flow evolution for Experiment 24, 10 (cc/s) with isothermal conditions

Figure 4.25: Isothermal flow dynamics for experiments $1cc24C$, and $10cc24C$.

These images reveal there are different dynamical regimes governing flows that undergo cooling when compared to isothermal conditions. All 4 experiments detailed here show an initial regime close to axisymmetrical evolution followed by lateral and downslope spreading, elements that show constant evolution in time until reaching the end of material extrusion as evidenced by black or blue vertical lines. After this event, differences between isothermal and cooling flows become evident for downstream evolution, where transition points are placed immediately after ζ_Q in cooling experiments followed by a sudden decrease in velocity that

leads to complete end of motion of the flow at final distances not much larger than corresponding L^*, whereas isothermal flows continue to grow at a smaller rate after ζ_Q until reaching what we assume to be a transition point (t^*, L^*) although arbitrarily chosen as the next slope change after ζ_Q, although a series of slope changes occur after this time, none of these two experiments have a sudden decrease in flow velocity until reaching maximum downslope extent, but rather continue to advance at higher velocities, compared to their cooling counterparts, until suddenly coming to a halt. Dynamical behavior just as described is seen in all cooling experiments as has been shown in figures from the first section in this chapter.

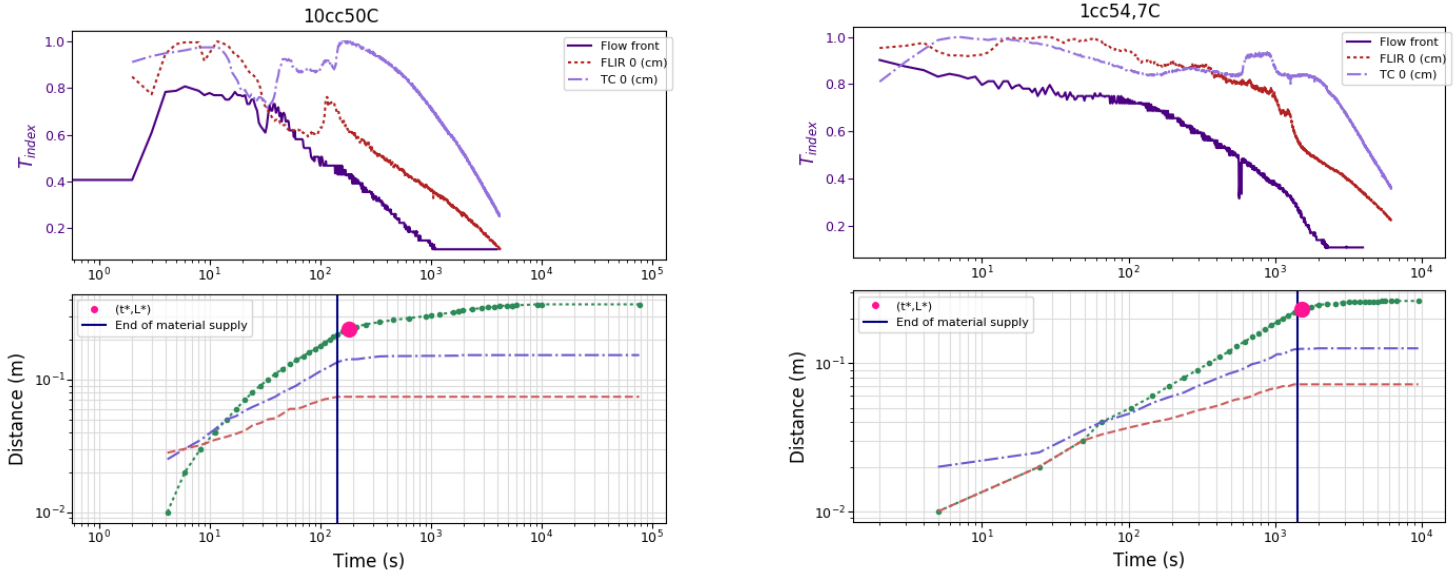

(a) Flow evolution for Experiment 30, 10(cc/s) with cooling from 55 degrees celsius

(b) Flow evolution for Experiment 31, 1 (cc/s) with cooling from 55 degrees celsius

Figure 4.26: Cooling flow dynamics. Temperature index shown for flow front region in deep blue, for *FLIR* data from surface temperature over the extrusion point in crimson and for thermocouple measurement for inner temperature of extrusion point in soft blue.

Cooling evolution of the flow seen in Figure 4.27 shows three curves representing thermocouple and *FLIR* data as T_{index} with measured temperatures represented by different colors: purple line shows surface temperature over extrusion point in time, green line shows thermocouple measurement of temperature in extrusion point corresponding to inner thermal evolution of manjar and finally red line represents surface thermal evolution of flow front. Figure 4.27a shows a close up from 0 to 800 (s), by this time experiments of flow rate from 5 to 25 (cc/s) had already reached their ζ_Q. Most of these experiments present a heat loss of up to 85% in the flow front, followed by almost a 50% heat loss in the flow surface right above the extrusion point. For thermocouple index results show variability, although most present that inner temperature of the flows drops less and more slowly than surface temperature, confirming there is a temperature profile in the flows. On the other hand, experiments of $Q = 1$ (cc/s) present heat loss of up to 50% by 800 (s), almost half their ζ_Q and purple and green curves drop only a 10 to 20%, which indicates that material is coming out at temperatures a bit lower than initial. Figure 4.27b includes ζ_Q for experimentss of $Q = 1(cc/s)$, presenting a sudden decrease in surface temperature with respect to inner temperature around this time. Flow front temperature drops to T_{index} around to 0.2 and for experiments of higher Q this number goes even lower.

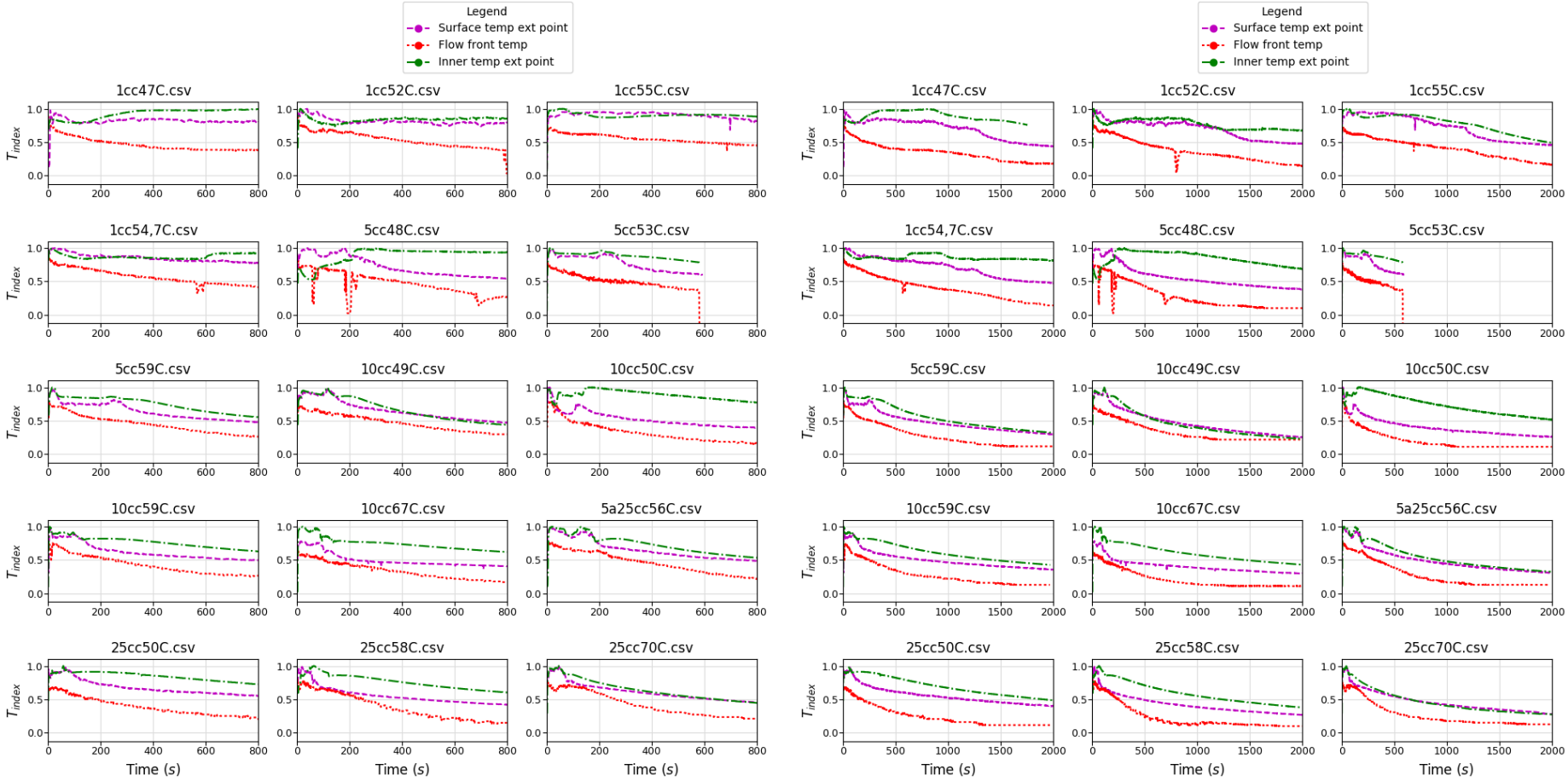

(a) Detail up to 800 (s) of flow evolution.

(b) Detail up to 2000 (s) of flow evolution.

Figure 4.27: Cooling evolution of three different portions of the flow for 11 experiments: green curve shows temperature index for thermocouple measurements in extrusion point, purple curve shows temperature index of superficial temperature over extrusion point, red curve shows temperature index for flow front.

The cooling evolution in Figure 4.28 shows T_{index} for experiments with *FLIR* data only, also for time 800(s) and 2000 (s). Results show by 800 (s) all flow fronts reach T_{index} close to 0.25 or lower, including 1cc51C, and it is always lower than the index corresponding to surface temperature over extrusion point.

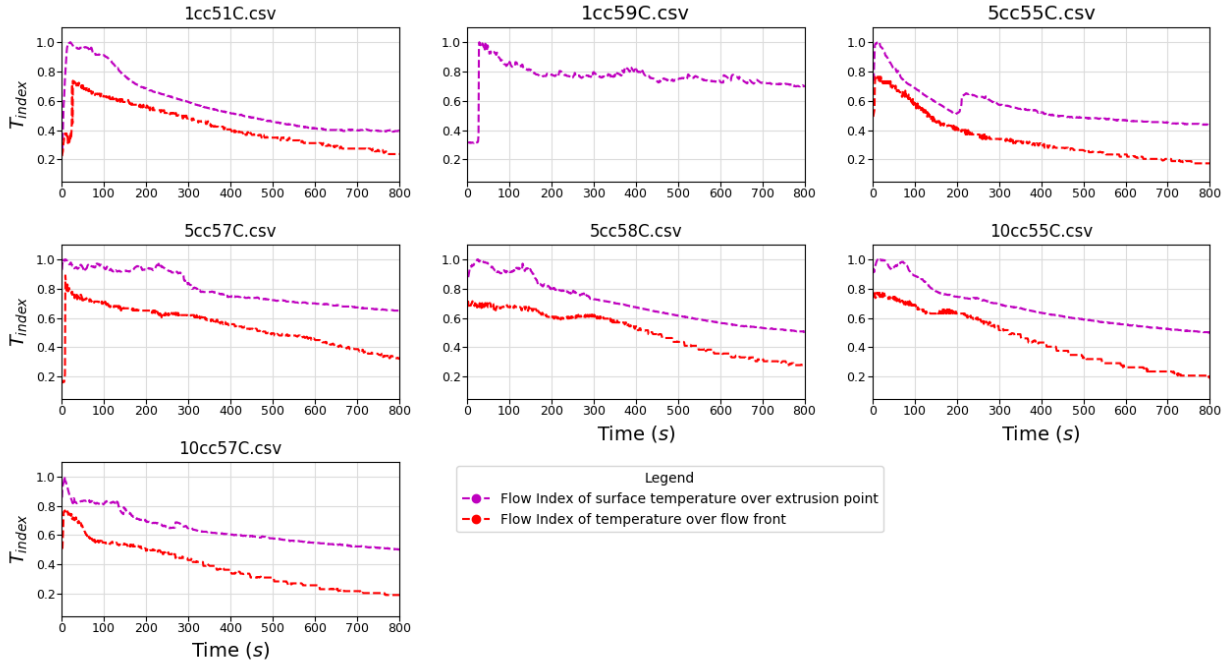

(a) Temperature index at flow front and of surface over extrusion point until 800 (s).

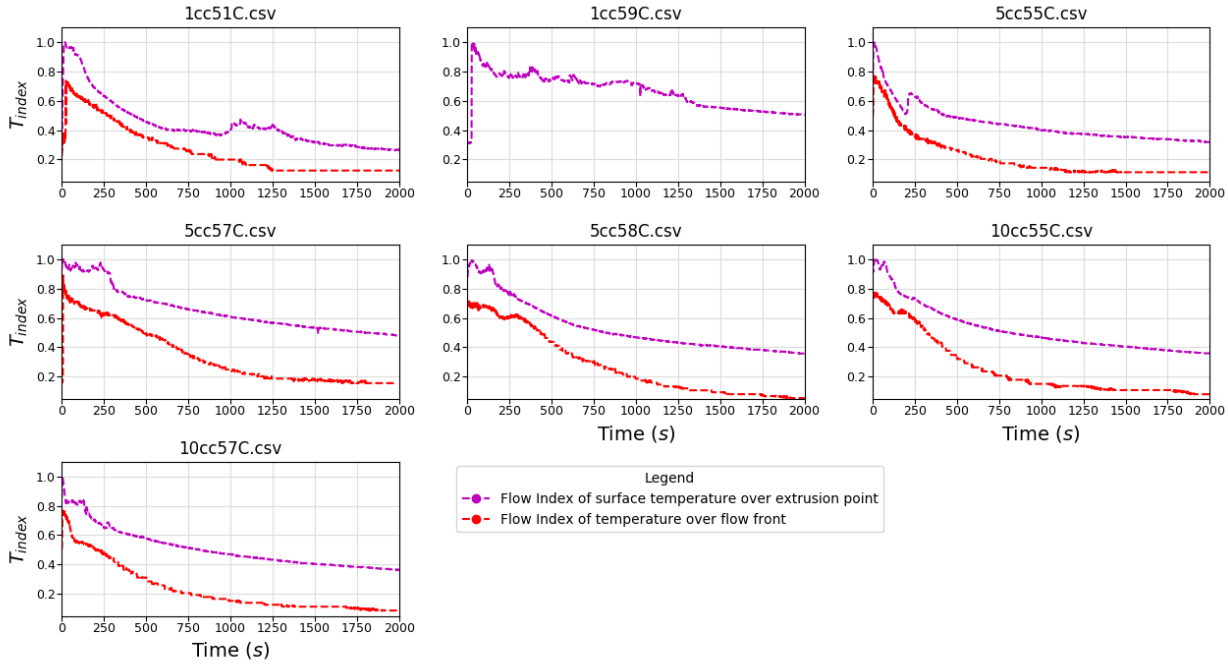

(b) Temperature index at flow front and of surface over extrusion point until 2000 (s)

Figure 4.28: Temperature index at flow front and of surface over extrusion point.

Next, temperature indexes are grouped by flow rate. In Figure 4.29 the T_{index} of flow front is shown. By 800 (s) flows with $Q = 5, 10$ (cc/s) have reached indexes lower than 0.5, closer to 0.25, while flows of $Q = 1$ (cc/s) shows higher indexes close to 0.5, except one line that should correspond to 1cc51C that lies above all being close to 0.75, but still appear larger due to the fact that extrusion is still on course by this time and only about half total material is out. There is still heat input from reservoir as shown by the lower indexes presented by the remaining experiments that have already been completely extruded and are subject to temperature loss from the surface with no new material at higher temperature being injected. Experiments of rates higher than 1 get their T_{index} to plateau near the value of 0.2 by 1250 (s). At 2000 (s) flow front index for all experiments reach a value of 0.2 or lower regardless of flow rate.

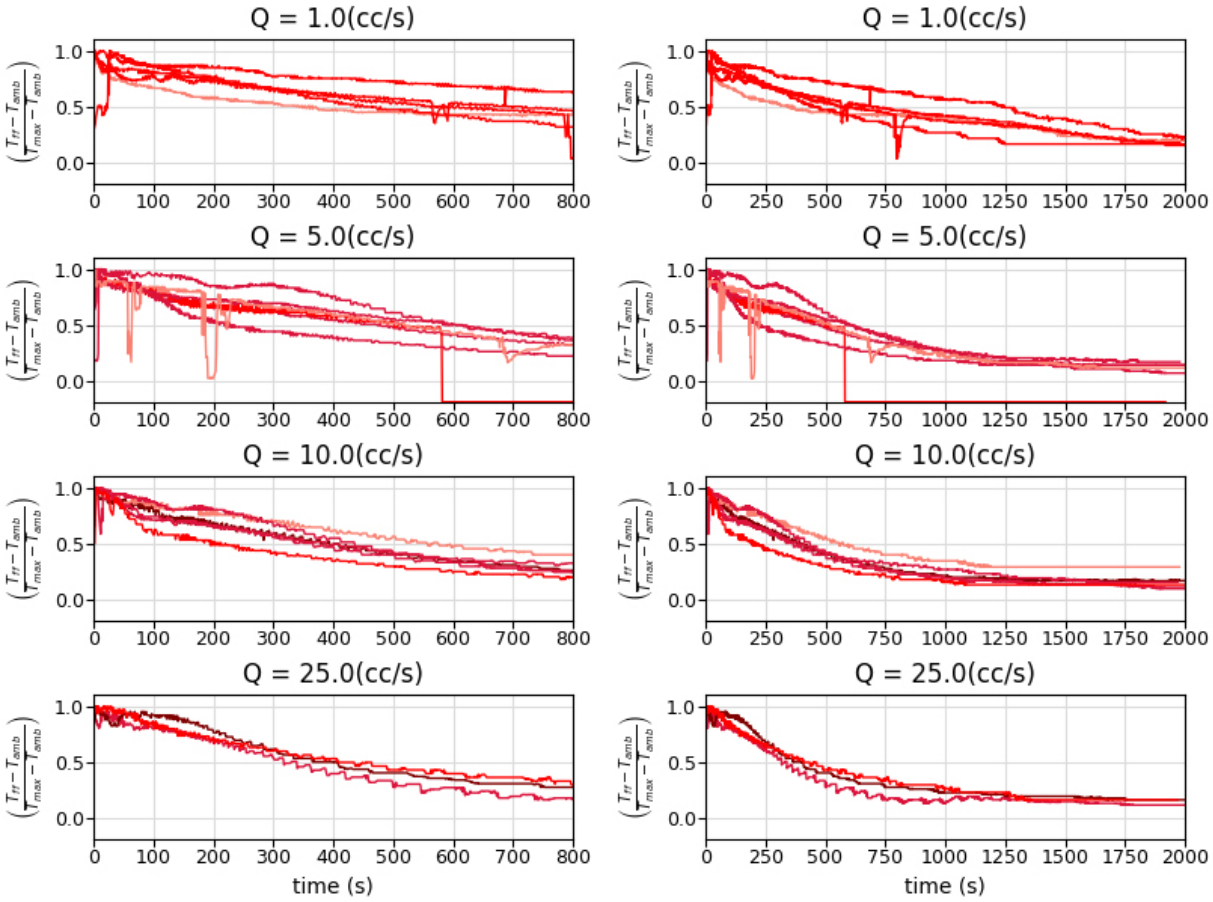

(a) Close up from 0 to 800 (s).

(b) From 0 to 2000 (s).

Figure 4.29: Temperature index at flow front grouped by flow rate.

Temperature index for surface over extrusion point from *FLIR* data in Figure 4.30 reveals that for at least 1 experiment in each of the flow rates the heat inside material reservoir was heterogeneous, showing a rapidly decreasing T_{index} that plateaus and then goes back up shortly before going down again. These experiments are 1cc51C, 5cc55C and 10cc50C. These figures also show that T_{index} decreases slowly while fresh material is being poured out of the reservoir and presents a sudden drop at ζ_Q for all flows, reaching values that go from 0.45 to 0.25 by 2000 (s). All these indexes are higher than the previous index shown for flow front

region, showing that heat loss is greater in that zone due to fresh material being poured from the extrusion point at higher temperatures while older material accumulates in the perimeter of the flow, being front zone and borders of the flow.

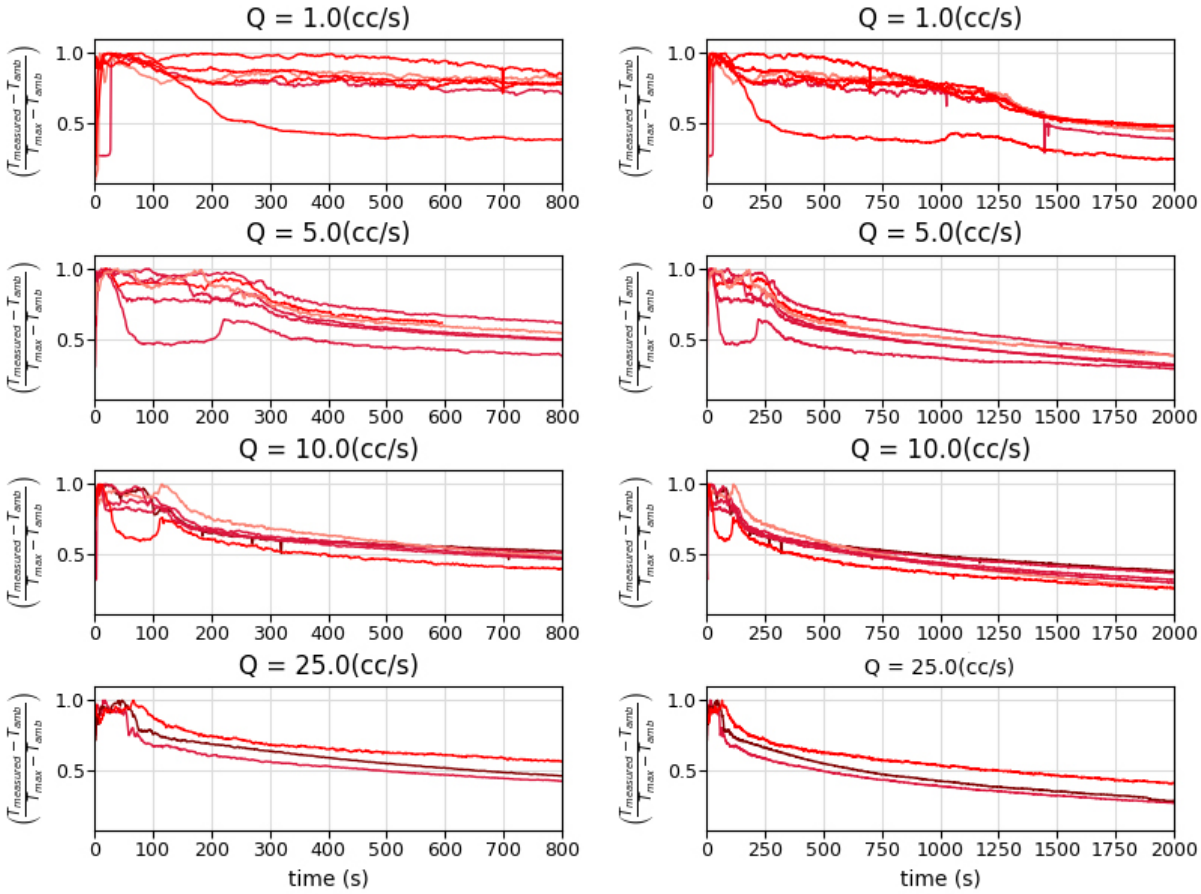

(a) Close up from 0 to 800 (s).

(b) From 0 to 2000 (s).

Figure 4.30: Temperature index of surface over extrusion point grouped by flow rate.

Figure 4.31 shows T_{index} of thermocouple measurement in the extrusion area that remains covered in manjar during material ejection and after spreading, representing the inner temperature of the flow. It shows greater dispersion than prior indexes, but the bigger picture reveals consistent results as for higher flow rate the index decreases faster than for lower flow rates, and by 2000 (s) T_{index} is lower for Q = 25 (cc/s), showing the material is cooler because it has been subject to ambient temperature for longer times than their lower Q counterparts.

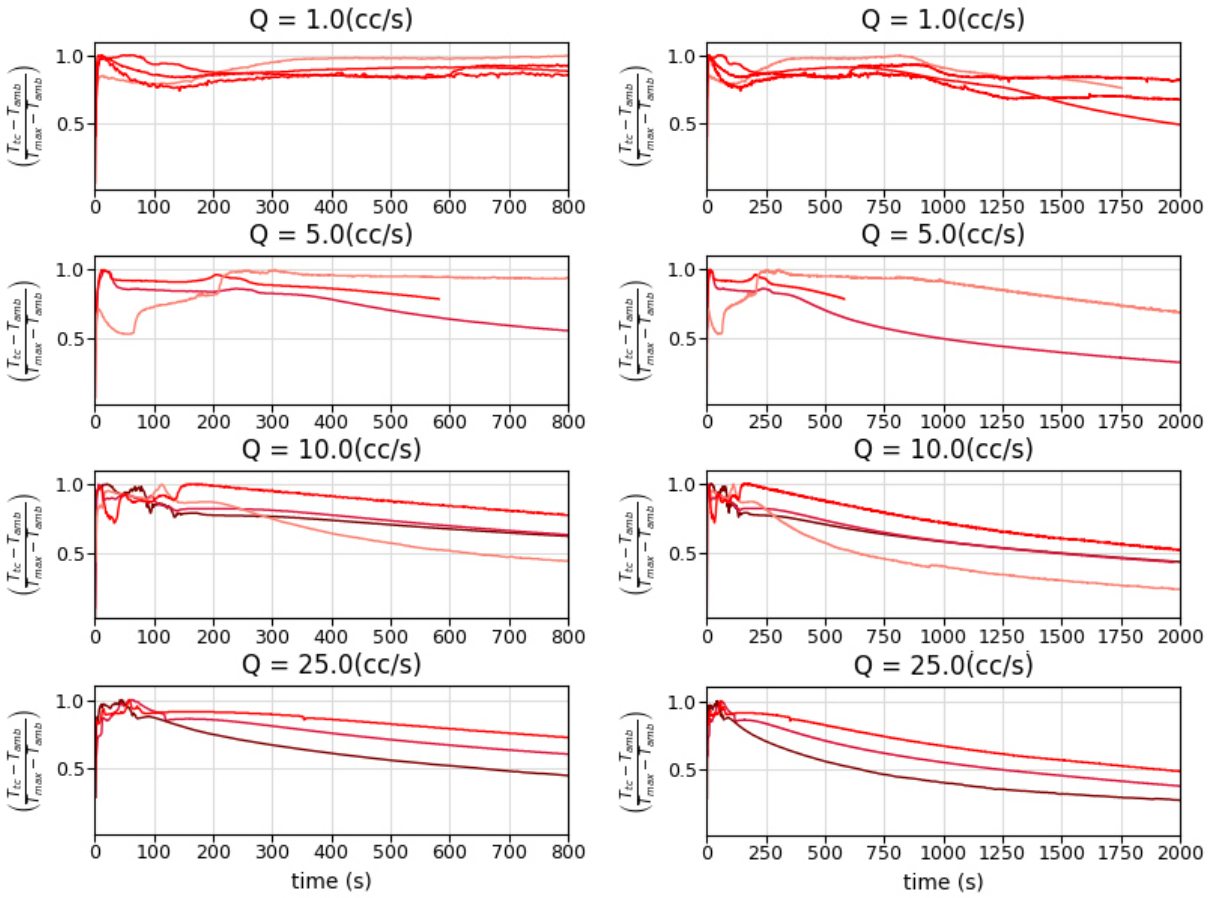

(a) Close up from 0 to 800 (s).

(b) From 0 to 2000 (s).

Figure 4.31: Flow index of thermocouple placed over extrusion point grouped by flow rate.

4.4 Dimensional Analysis

4.4.1 Flow dynamics

For analyzing all gathered data of advance of flows in time, we find an estimate of time and length scale from known parameters of the flow as g, gravity acceleration, ρ, material density, Q, flow rate and μ_{app}, the estimated viscosity shown in equation 4.1. With these parameters we find two dimensionless numbers, π_1 and π_2, that represent time and length scales shown in equations 4.3 and 4.4, and plotted in Figure 4.32 for every experiment performed in the laboratory. This shows that the dynamical evolution of the flows involving cooling present similarities regardless of flow rate or underlying slope, showing two main regimes divided by a transition point (t^*, L^*) plotted in Figure 4.32 with a blue circle.

$$\pi_1(L) = (\frac{L^5 g}{Q^2})^{\frac{1}{5}} \tag{4.3}$$

$$\pi_2(t) = (\frac{\mu_{app}}{\rho})^3 \frac{t}{Q^2} \tag{4.4}$$

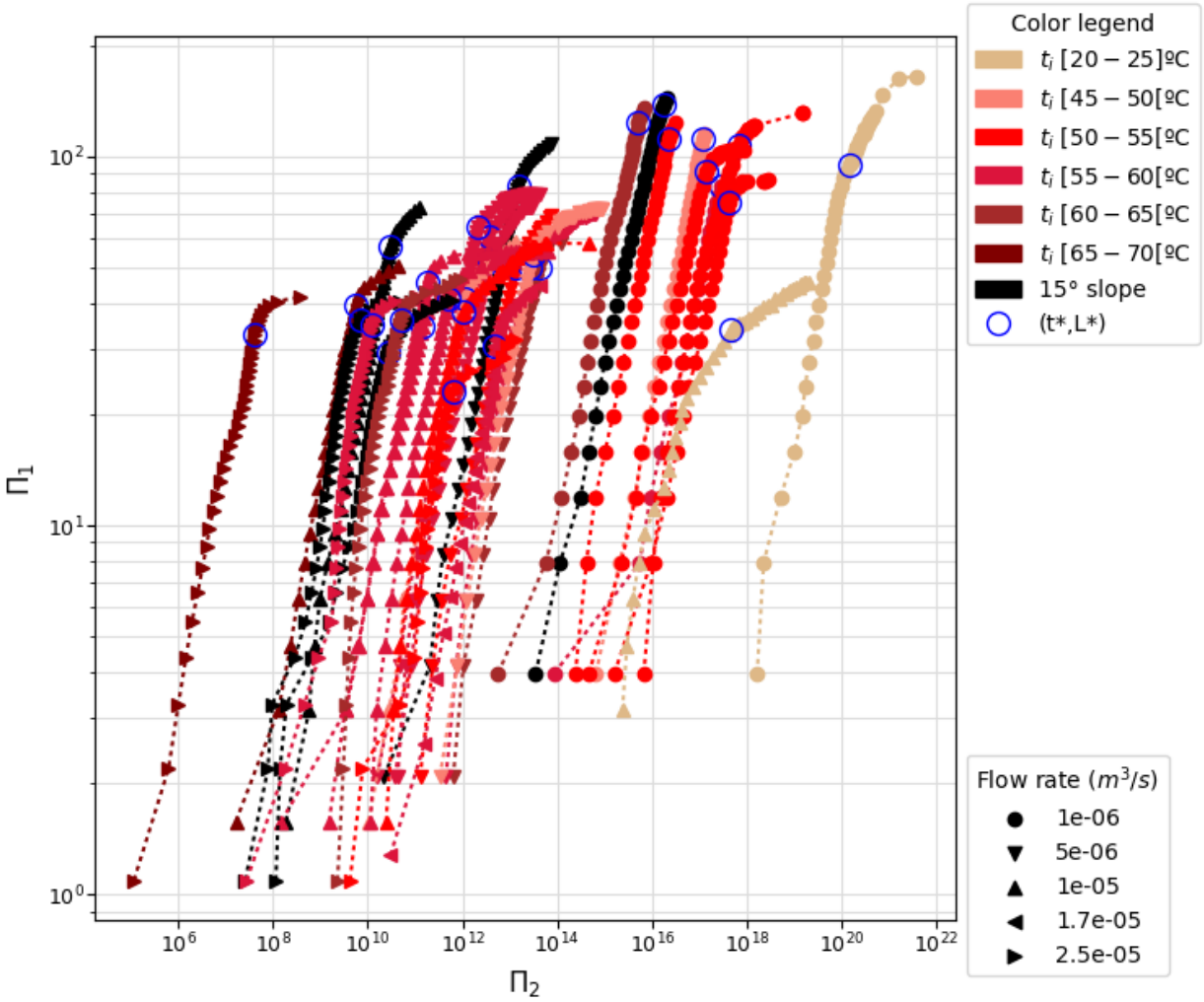

Figure 4.32: Dimensionless time versus length for all experiments. The point (t^*, L^*) is represented in each curve as a blue circumference.

Considering the majority of experiments shows a well defined transition point, the dimensionless numbers are reevaluated and divided by their own $(\pi_2(t^*), \pi_1(L^*))$, as shown in equations 4.7 and 4.8.

$$\pi_1(L^*) = (\frac{(L^*)^5 g}{Q^2})^{\frac{1}{5}} \tag{4.5}$$

$$\pi_2(t^*) = (\frac{\mu_{app}}{\rho})^3 \frac{t^*}{Q^2} \tag{4.6}$$

By factoring all curves with this transition point as shown in Figure 4.33, it is very well defined how most experiments collapse into a single curve with two predominant slopes and share a transition point between early regime evolution at high velocities reaching their transition lengths, followed by a long time regime where flows continue to grow at a diminished rate until

reaching halt. It appears during the first centimeters of advance there is greater dispersion of the data with a number of different slopes that tend to converge to a similar value until reaching $\pi_1(L^*)$ at a constant velocity V^* defined by the early regime. The curve with lighter color represents isothermal experiment 1cc24C and does not completely fits in the same time evolution of the cooling flows, indicating their emplacement is controlled by a different regime. This will be analyzed further in the discussion section.

$$\pi_1^* = \frac{\pi_1(L)}{\pi_1(L^*)} \tag{4.7}$$

$$\pi_2^* = \frac{\pi_2(t)}{\pi_2(t^*)} \tag{4.8}$$

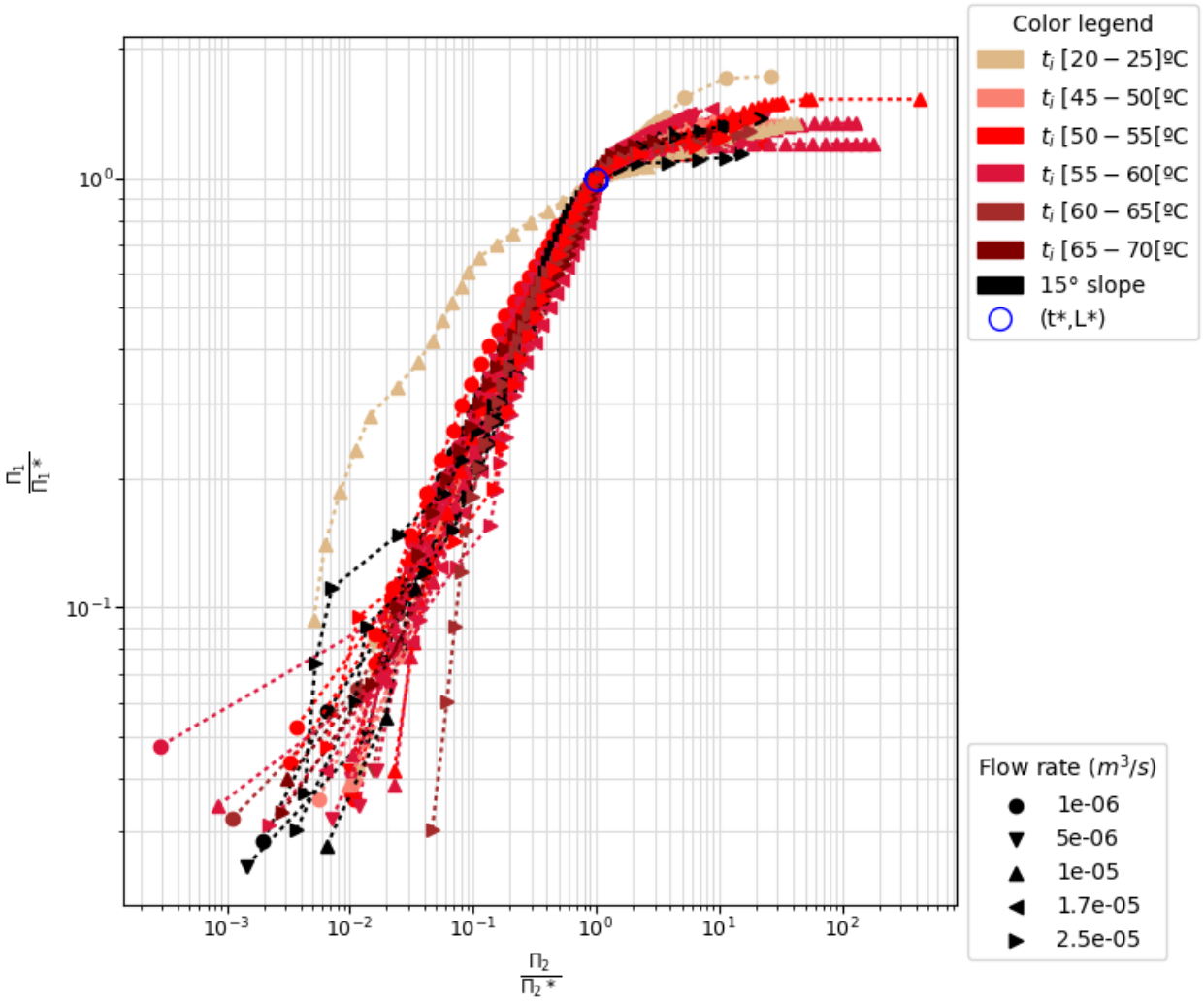

Figure 4.33: Normalized dimensionless time versus normalized dimensionless length for all experiments. The figure shows how the vast majority of flows converge on a curve that has a breaking point that corresponds to (t^*, L^*), identified in each experiment.

4.4.2 Flow properties and emplacement

Attempts to relate rheology with resulting dimensions of the flow are made through a dimensionless yield strength number π_3, shown in equation 4.9, with chosen dimensionless length. As equation 4.9 depends on yield strength, it also needs to be evaluated at a certain temperature, and there are a number of possible scenarios to choose from in order to obtain this number, but only two were chosen for this purpose. The first is an average between maximum and ambient temperature, T_{avg}, and the second is $T_{flowfrontt^*}$, which is estimated from the temperature index of flow front evaluated in t^* and multiplied by T_{max} and represents the temperature of the flow front according to *FLIR* imaging.

$$\pi_3(\tau_y) = \frac{Q^2\rho^5(g\sin\theta)^4}{\tau_y^5} \tag{4.9}$$

Given that not all flows reach their run-out lengths, the chosen distance for evaluating $\pi_1(L)$ can also vary, being X_{max} and L^* the most relevant. The detail of variables presented here, the number of experiments that present such data and were used to obtain the power law fits are detailed in Table 4.3.

Table 4.3: Power law fit for π_1 and π_3 for two settings.

Temperature	**Experiments**	**Length**	**Total data**	**Constant**	**Exponent**	r^2
T_{avg}	Cooling with $V_{final} = 0$	X_{max}	11	35,072	-0,139	0,91
$T_{flowfrontt^*}$	Cooling	L^*	20	32,823	-0,045	0,73

These fits are illustrated in Figure 4.34 with the corresponding experiments that were used to obtain them. Each allows for a method of estimating the maximum possible extent of the flows, the first consists in estimating X_{max} from the power law between $\pi_3(\tau_y(T_{avg}))$ and $\pi_1(X_{max})$ according to experiments with cooling that have $V_{final} = 0$. The second consists of estimating $\pi_1(L^*)$ from $\pi_3(\tau_y(T_{flowfrontt^*}))$, followed by using the ratio known for experiments with $V_{final} = 0$ between L^* and X_{max}, which has an average value of $0,77$, to obtain X_{max}. Given that not all flows have *FLIR* information available, estimated X_{max} can only be obtained for 22 experiments with this approximation. Results obtained for both methods are shown in Tables 4.4 and 4.5.

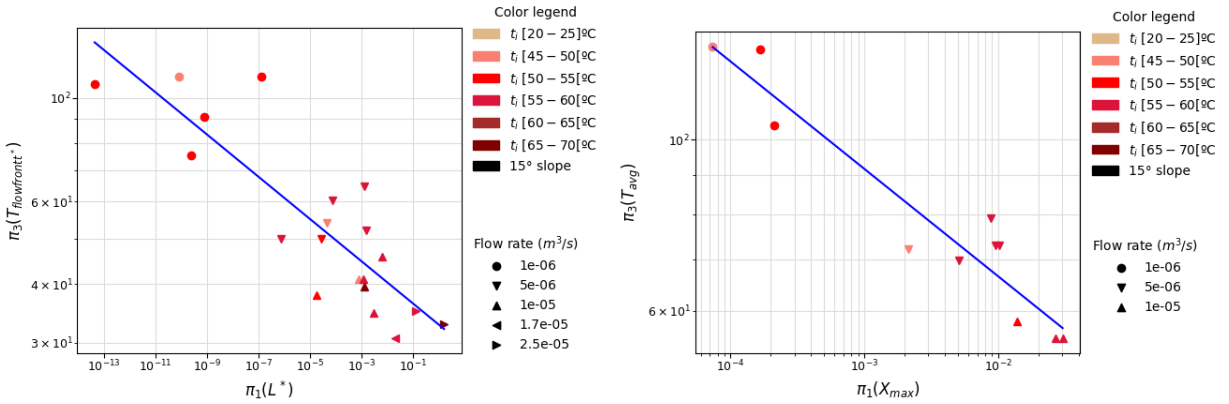

(a) Dimensionless transition length versus dimensionless yield strength estimated at flow front temperature for transition time t^* with power law fit shown in equation 4.3 for all experiments in cooling conditions.

(b) Dimensionless maximum length reached for cooling experiments that came to halt versus dimensionless yield strength evaluated at an average temperature between maximum inicial temperature and room temperature.

Figure 4.34: π_3 versus π_1 evaluated in Table 4.3. Both approximations are be used for estimating the maximum downslope length reached by flows that did not stop completely.

The ratio between estimated X_{max} and L^* with measured lengths from the experiments are also specified in Tables 4.4 and 4.5. The first method has a better correlation and can be applied to a larger number of experiments, which leads in a total of 17 estimated final lengths larger than measured, although this number contains 5 experiments that had already reached their maximum length according to $V_{final} = 0$ criteria. The second method displays a total of 12 experiments with estimated maximum lengths larger than measured, with a total of 4 experiments that had already reached their final lengths according to our criteria.

Table 4.4: Results of estimated X_{max} from material properties for experiments with Q = $1(cc/s)$ and $5(cc/s)$

Exp	X_{max}	V_f	L^*	t^*	1) X_{est}	1) $\frac{X_{est}}{X_{max}}$	1) L^*_{est}	1) $\frac{L^*_{est}}{L^*}$	2) L^*_{est}	2) $\frac{L^*_{est}}{L^*}$	2) X_{est}	2) $\frac{X_{est}}{X_{max}}$
1cc24C	0,415	1,61E-07	0,239	2126,3	0,640	1,541	0,492	0,485				
1cc47C	0,29	6,92E-05	0,28	1465,1	0,342	1,178	0,263	1,064	0,240	0,857	0,312	1,075
1cc51C	0,33	0	0,27	2401,4	0,297	0,899	0,228	1,183	0,299	1,109	0,389	1,178
1cc52C	0,218	7,17E-07	0,19	1502,5	0,312	1,430	0,240	0,792	0,229	1,205	0,297	1,364
1cc54,7C	0,263	0	0,23	1516,0	0,287	1,090	0,221	1,042	0,220	0,955	0,285	1,085
1cc54C	0,363	7,41E-05	0,35	1515,5	0,235	0,647	0,181	1,937				
1cc55C	0,31	6,59E-05	0,28	1178,4	0,282	0,909	0,217	1,291	0,158	0,565	0,205	0,663
1cc59C	0,21	4,27E-05	0,21	1712,2	0,265	1,261	0,204	1,030				
1cc62C	0,34	5,75E-05	0,31	1320,2	0,242	0,712	0,186	1,663				
5cc48C	0,346	0	0,26	316,5	0,393	1,136	0,303	0,859	0,252	0,968	0,327	0,944
5cc50C	0,518	2,79E-05	0,4	342,7	0,310	0,598	0,239	1,676				
5cc53C	0,332	1,53E-05	0,24	293,1	0,338	1,018	0,260	0,922	0,250	1,041	0,324	0,977
5cc55C	0,335	0	0,24	315,2	0,348	1,038	0,268	0,896	0,287	1,197	0,373	1,114
5cc57C	0,35	0	0,25	291,3	0,317	0,907	0,244	1,023	0,226	0,902	0,293	0,837
5cc58C	0,38	0	0,31	329,4	0,322	0,847	0,248	1,251	0,204	0,656	0,264	0,696
5cc59C	0,35	0	0,29	332,0	0,315	0,899	0,242	1,197	0,243	0,837	0,315	0,901
5cc63C	0,28	2,80E-05	0,24	272,3	0,283	1,010	0,218	1,102				
5a25cc56C	0,35	1,67E-05	0,24	198,2	0,382	1,092	0,294	0,816	0,309	1,286	0,401	1,145
						10		12		5		6

Table 4.5: Results of estimated X_{max} from material properties for experiments with Q = $10(cc/s)$ and $25(cc/s)$

Exp	X_{max}	V_f	L^*	t^*	1) X_{est}	1) $\frac{X_{\text{est}}}{X_{max}}$	1) L^*_{est}	1) $\frac{L^*_{est}}{L^*}$	2) L^*_{est}	2) $\frac{L^*_{est}}{L^*}$	2) X_{est}	2) $\frac{X_{\text{est}}}{X_{max}}$
10cc24C	0,29	0	0,214	1180,4	0,854	2,943	0,657	0,326				
10cc49C	0,374	3,07E-05	0,26	145,8	0,410	1,096	0,316	0,824	0,279	1,074	0,363	0,970
10cc50C	0,368	0	0,24	182,0	0,398	1,081	0,306	0,784	0,342	1,426	0,445	1,208
10cc55C	0,35	0	0,29	158,0	0,362	1,036	0,279	1,039	0,264	0,909	0,342	0,978
10cc57C	0,35	0	0,26	140,8	0,356	1,016	0,274	0,949	0,280	1,076	0,363	1,038
10cc59C	0,3	3,36E-05	0,22	134,7	0,327	1,089	0,251	0,875	0,276	1,256	0,359	1,196
10cc60C	0,46	8,40E-05	0,36	144,3	0,270	0,586	0,208	1,735				
10cc67C	0,32	2,37E-05	0,25	142,2	0,293	0,916	0,226	1,107	0,254	1,015	0,329	1,030
25cc50C	0,292	1,30E-05	0,21	93,6	0,429	1,468	0,330	0,636				
25cc54C	0,373	9,55E-06	0,27	69,8	0,341	0,914	0,263	1,029				
25cc58C	0,39	1,71E-05	0,32	89,7	0,383	0,982	0,295	1,085	0,340	1,061	0,441	1,131
25cc60C	0,378	2,42E-05	0,33	90,5	0,300	0,793	0,231	1,430				
25cc62C	0,427	2,01E-05	0,33	95,7	0,337	0,789	0,259	1,272				
25cc70C	0,38	2,40E-05	0,3	70,5	0,301	0,792	0,232	1,294	0,294	0,981	0,382	1,006
						7		8		6		6
Total						17		20		11		12

4.4.3 Graetz number

The Graetz number has been used by previous authors in Hawaiian and Etnean flows, showing most lava flows reached a critical distance at a Graetz number of approximately 300. In Figure 4.35 the Graetz is illustrated for all performed experiments with their corresponding downslope distance, estimated H_{din}, which corresponds to the ξ_{din} value in time as estimated maximum depth, V_1 and thermal diffusivity of manjar plotted against normalized time. Two horizontal cyan lines are plotted in this figure as well, encasing values of 200 and 300 for the Graetz number.

$$Gz = \frac{v_1 H_{\text{din}}^2}{\kappa X_{max}} \tag{4.10}$$

Using the same dimensionless time ratio normalized by t^*, π_2, we plot the Graetz as shown in equation 4.10 in Figure 4.35. Due to the direct relationship between this number and the velocity of the flows, the transition point is also evident in these curves, being the inflection point of the curve. Flow rate is the main difference between flows that reach their final lenghs prior to critical Gz number and those that reach it after these values.

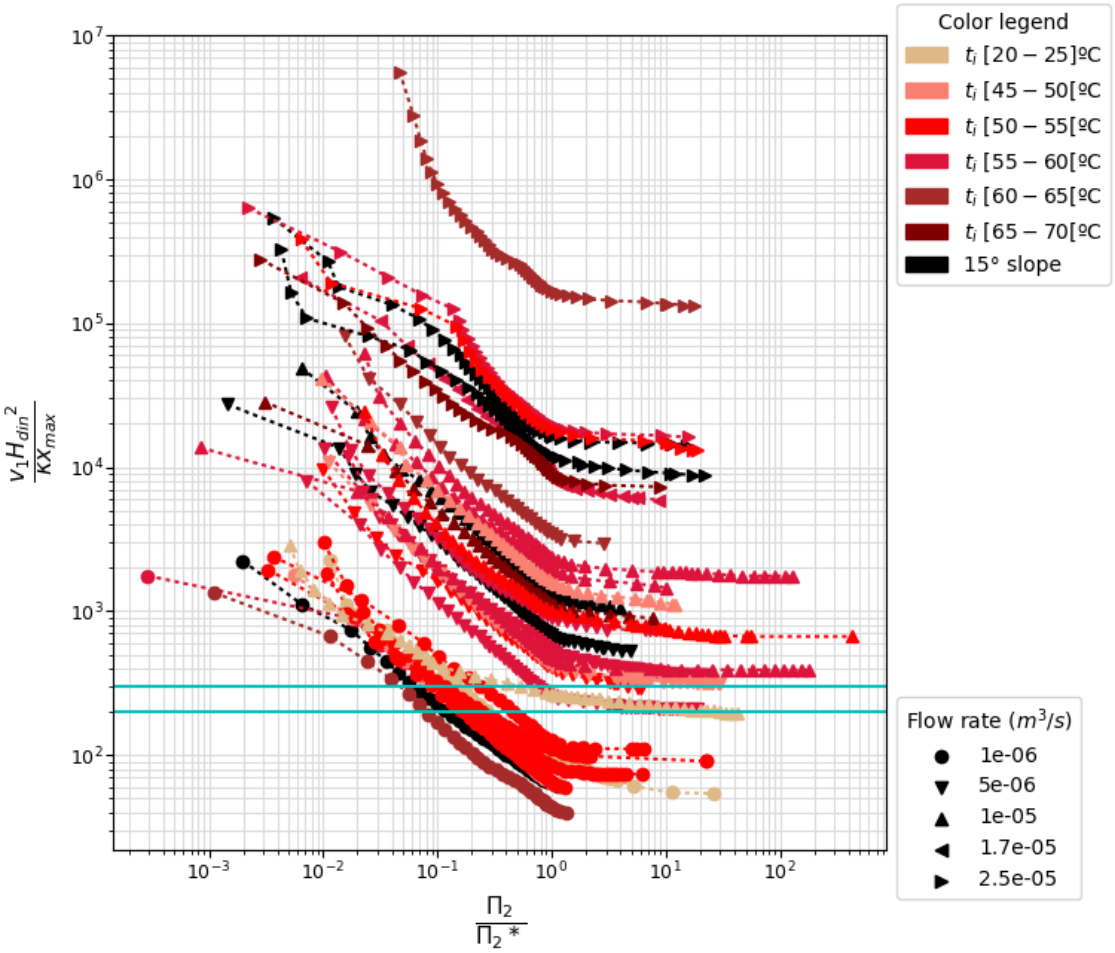

Figure 4.35: Graetz number verus normalized dimensionless time for all experiments.

The Graetz number can be related to crust formation in this type of flows as shown by equation 4.11, where d represents depth of the flow, in this case H_{din}, and $\sqrt{\kappa t}$ the growing crust. We have previously mentioned that manjar does not develop a solid crust, unlike lava flows, but given that we have thermal diffusivity measurements, we use the concept of crust as the rheological layering due to temperature gradient present in cooling manjar flows.

$$\sqrt{Gz} = \frac{\mathrm{d}}{\sqrt{\kappa t}} \tag{4.11}$$

Crust formation is estimated for ζ_Q and transition time, t^*, for each of the flows, presented in Figure 4.36. Considering the critical Graetz number from 200 to 300, our experiments present a wide range of final Gz numbers that pass through this threshold, depending mainly upon flow rate, which is directly related to the duration of material extrusion, given that total volume numbers extruded was set constant. Experiments performed at lowest flow rate reach their final lengths at lower Gz, present the greatest crust growth by ζ_1 when compared to higher flow rates, and continue to flow further downslope while already passing the mentioned threshold. Conversely, experiments of higher flow rates have thinner crust developed by their corresponding ζ_Q and t^* times, and do not pass the threshold of critical Gz number before reaching their final lengths.

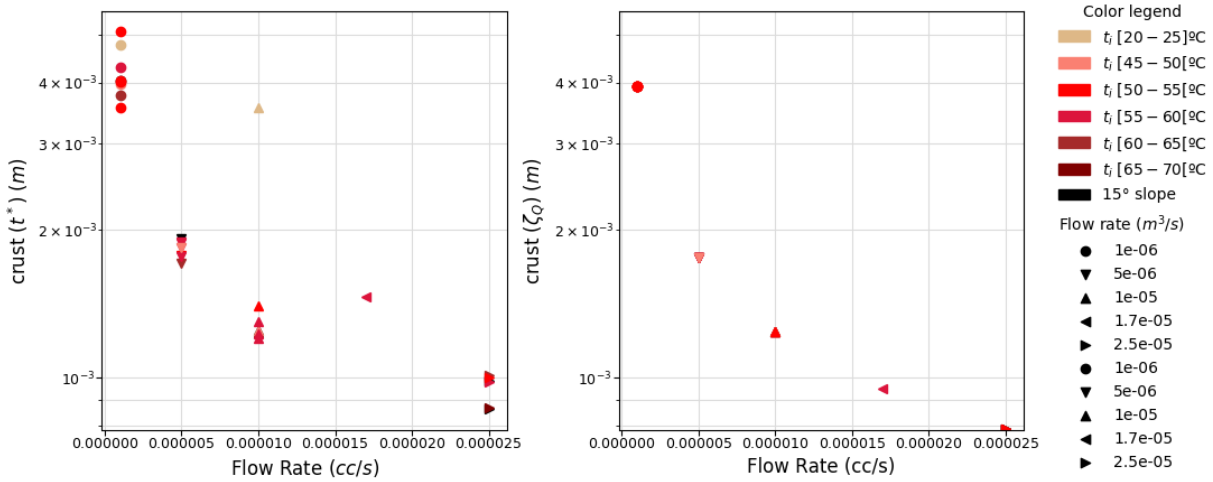

Figure 4.36: Estimated crust lenghts by transition time and ζ_Q.

Although our data reveals large orders of magnitude difference between Graetz numbers for our manjar flow models, there is a tendency to reach a minimum value and then plateau when the transition point of each experiment is reached.

4.5 Comparison with lava flows and experimental data

4.5.1 Flow dynamics

We selected 9 lava eruptions from 7 volcanoes: Puu Oo, 1983-84 (2 selected events) Wolfe (1988); Mauna loa 2984 Lipman and Banks (1987); Etna 2001 Coltelli et al. (2007), etna 2006 Vicari et al. (2009), Colima 1998-99 Navarro-Ochoa et al. (2002); Santiaguito Harris et al. (2004); Navidad 1988-89 Naranjo et al. (1992) and Cordon Caulle 2011 Magnall et al. (2017). We chose these eruptions due to the availability of data from beginning of the extrusion and the fact that, at least for periods of chosen time, the flows are simple and show a transition point similar to the one shown in the experiments. The eruptions had durations ranging from 1 day to 2 years, final lengths from 4 (km) to 26 (km). Compositions vary from basalt to rhyolite with low viscosities from 6 10^4 $(Pa\ s)$ to 3,6 10^{10} $(Pa\ s)$ and densities from 2300 $(kg\ m^{-3})$ to 2600 $(kg\ m^{-3})$.

With available information we are able to obtain dimensionless time and length for all mentioned flows with equations shown in the previous section referring to π_1 and π_2 in order to add this curves into our analysis of flow dynamics, as shown in the results of Figure 4.37.

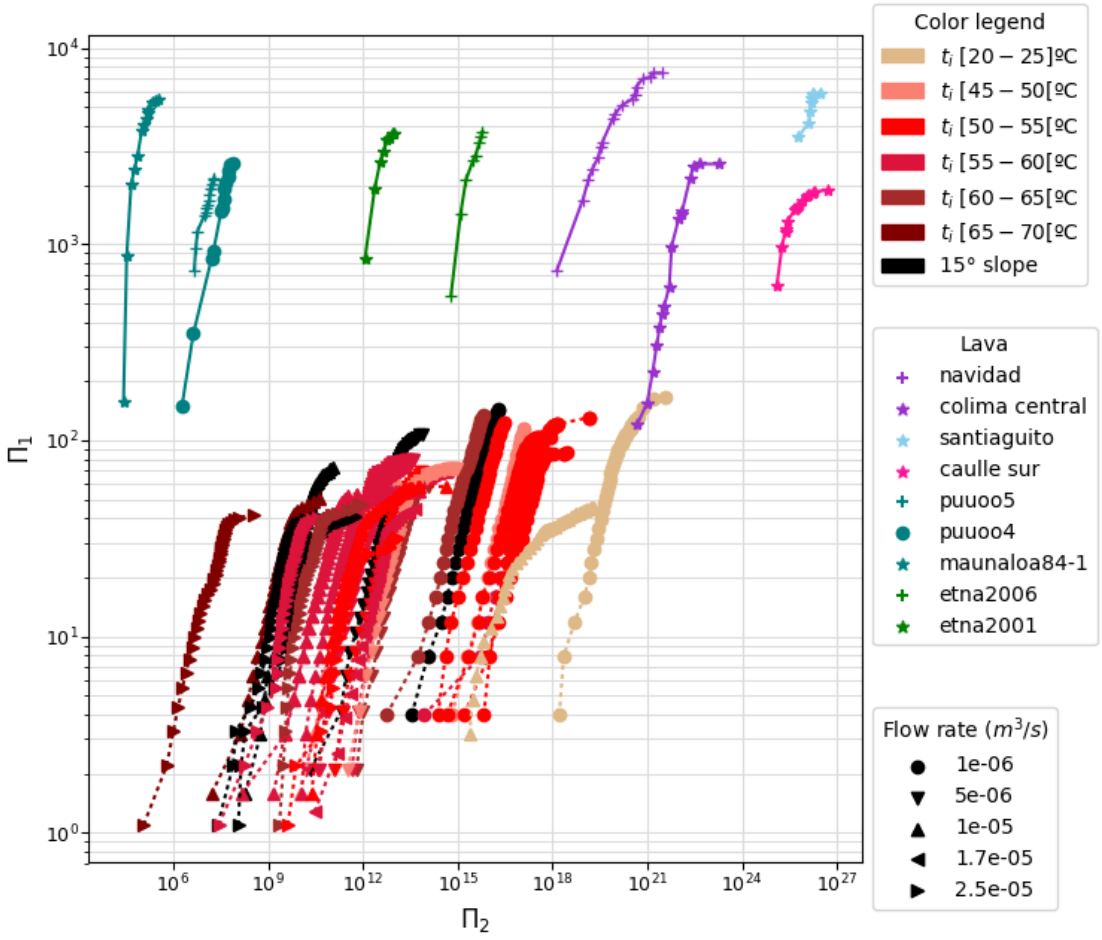

Figure 4.37: Dimensionless time versus length for all experiments and selected lava flows.

When incorporating data of natural lava flows in our dimensional analysis of flow evolution, we can also identify for most of these flows a transition point at which most of the maximum flow length has already been attained and there is still a little left to go to reach the final length but the flow approaches that point at lower velocities. Given the similarity found in our experiments, all mentioned flows can be divided by their own transition point, resulting in the collapse of all flow dynamics as shown by Figure 4.38.

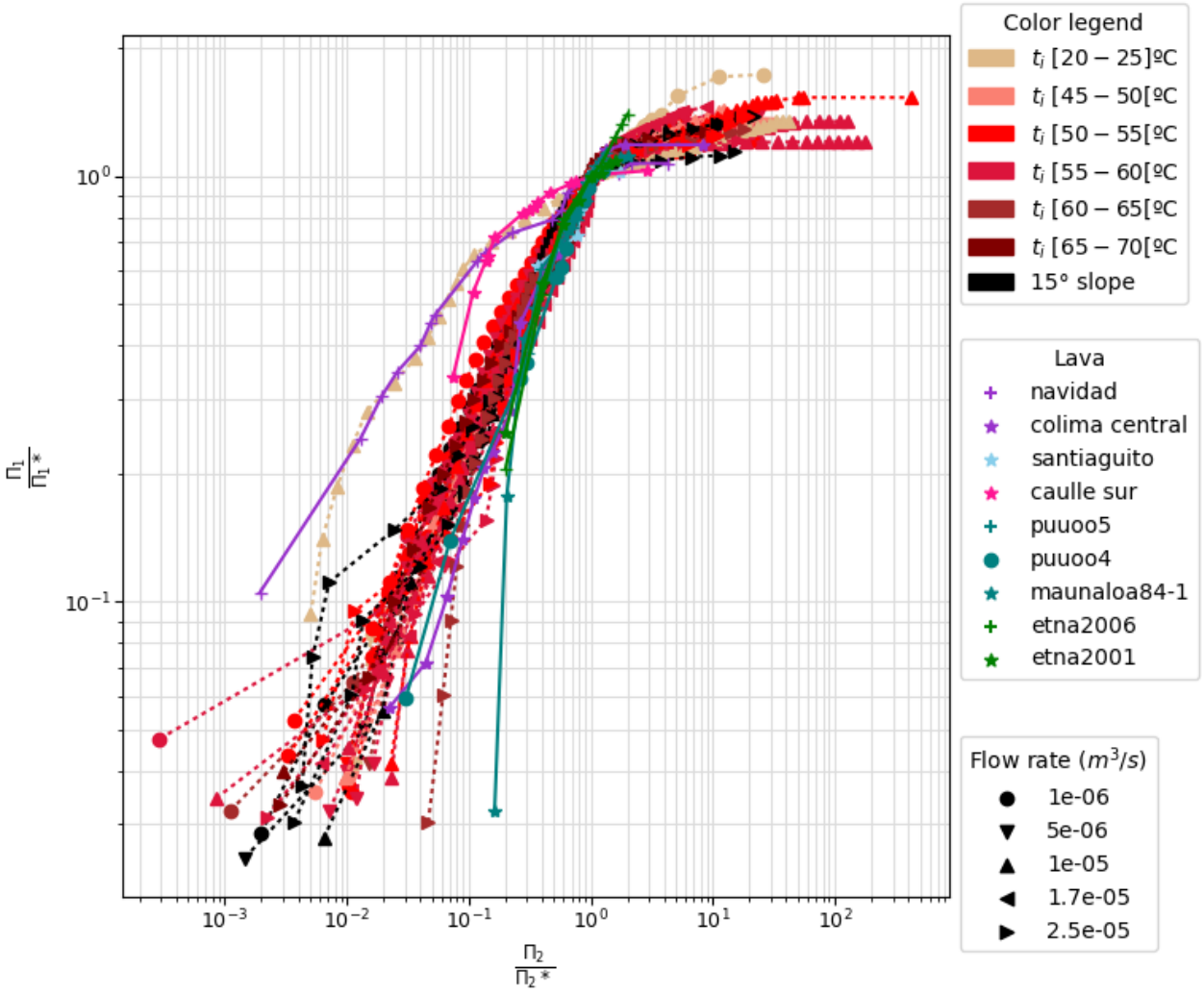

Figure 4.38: Normalized dimensionless time versus length for all experiments and selected lava flows

4.5.2 Flow properties and emplacement

We use the following equations to estimate Fr and Re numbers with equations 4.12 and 4.13 for depths and widths estimated at time t^*, when the flow is still in motion for all experiments, and also for final measured depths and widths for flows that reached their final lengths in Figures 4.39, 4.40, respectively. Our estimates for Fr and Re numbers use equations 4.14 and 4.15, because widths found for that range of lava flow values do not

correspond to autoconfined flows given the underlying topography, while experimental data from Castruccio et al. (2010) only estimates depths and lengths with a channel of predefined width, hence width data are not available for these cases. Still, we consider this comparison useful and revealing.

$$Re = \frac{Q}{w\mathrm{d}}^{2} \frac{\rho}{(\tau_y + \frac{KQ^n}{\mathrm{d}^{3n}})} \tag{4.12}$$

$$Fr = \frac{Q}{w\mathrm{d}\sqrt{g \sin\theta \mathrm{d}}} \tag{4.13}$$

As shown in Figures 4.39, 4.40 we find there is a link between flow rate and aspect ratio of the flows when plotted as modified Reynolds and Froude number as shown in equations 4.14 and 4.15, with a power law for our experimental data, experiments performed by Castruccio et al. (2010) and a range of lava flows defined by Table 3.4. Our results show that all curves present similar power law exponents that can be approximated to 2, but differ by orders of magnitude due to different constants considering the power law fit.

$$Re = \frac{Q^2}{\mathrm{d}^4} \frac{\rho}{(\tau_y + \frac{KQ^n}{\mathrm{d}^{3n}})} \tag{4.14}$$

$$Fr = \frac{Q}{\sqrt{g \sin\theta \mathrm{d}}\mathrm{d}^2} \tag{4.15}$$

Even though geometric dimensions of lava depend upon many factors, composition, underlying topography, total volume erupted, extrusion rate and more; we have chosen the custom range of lava flow properties of emplacement based mainly according to composition in order to estimate the modified Reynolds and Froude number previously exposed.

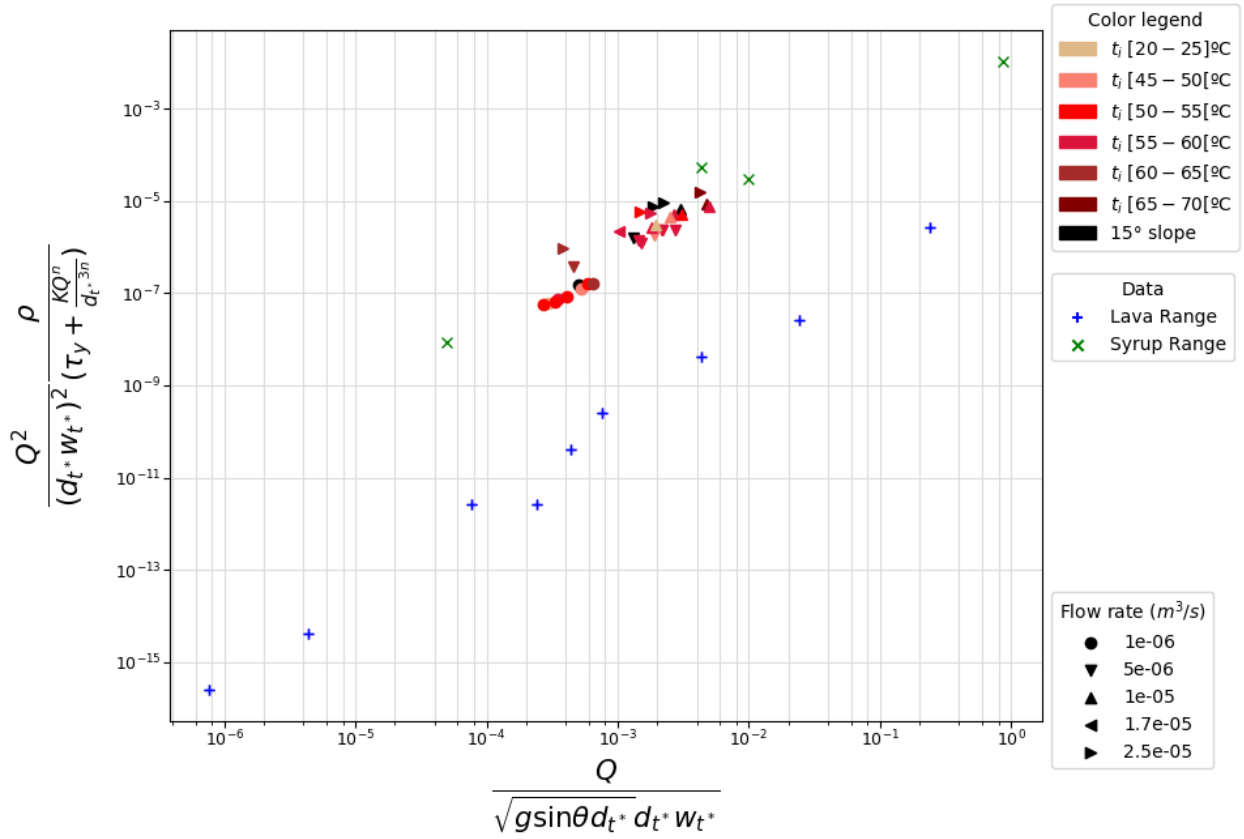

Figure 4.39: Ratio between modified Reynolds and Froude numbers for all experiments with depths and widths estimated ad time t^*, experimental data of Castruccio and a pre-defined range of lava data.

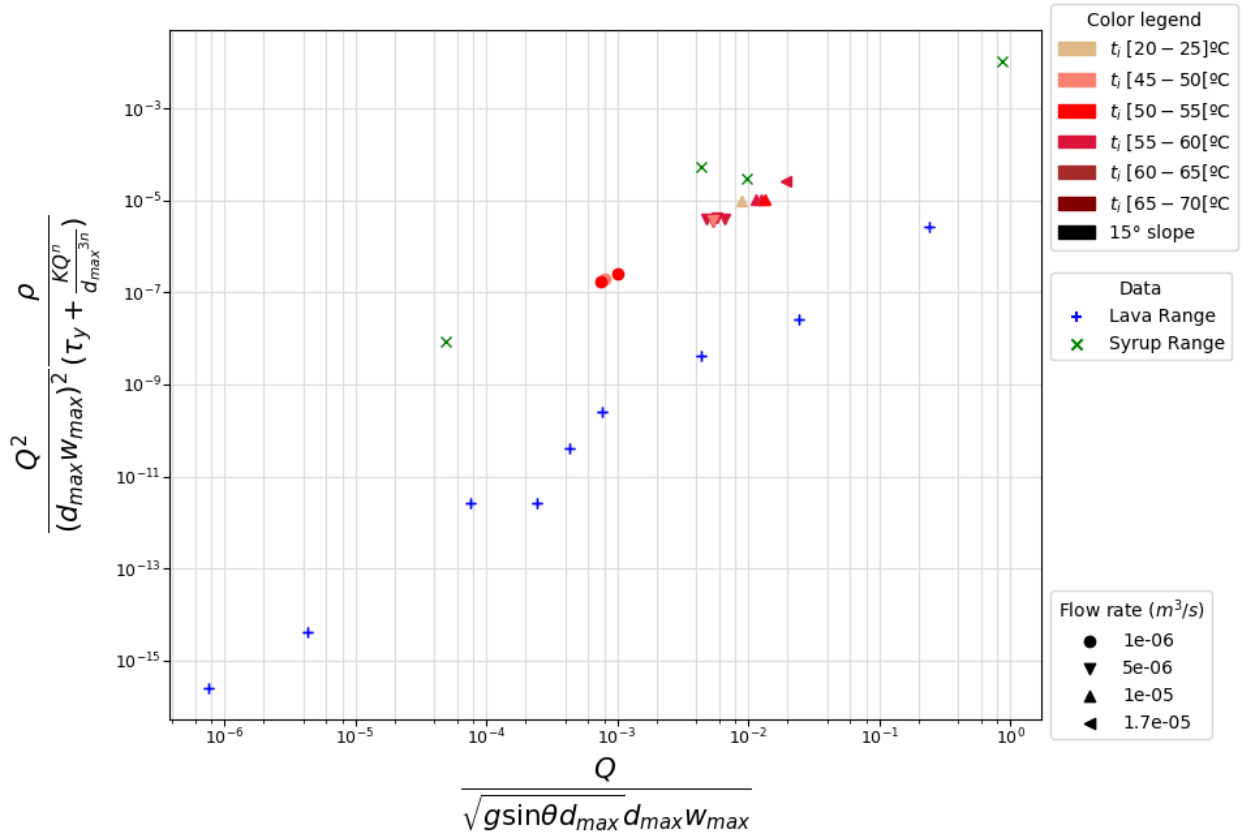

Figure 4.40: Ratio between modified Reynolds and Froude numbers for experiments that reached their final lenghts, with maximum measured widths and deths, experimental data of Castruccio and a pre-defined range of lava data.

This feature is known for laminar flows in a permanent regime and has already been briefly discussed by Filippucci et al. (2010), who relates a dimensionless flow velocity with flow regime as shown in equation 4.16. Our results fall within this approach, although we were not able to find the constant associated to S, representing a constant factor regarding slope, or V^n, that should be dependent of flow characteristics.

$$\frac{Re_{pl}}{Fr^2} = \frac{S}{g_x}\frac{1}{V^n} \tag{4.16}$$

4.6 Morphological features

The chosen experiment for developing the *DEM* estimate is, as the name indicates the flow rate was 1 (cc/s) and the initial temperature was 54℃, with a constant slope of 15°. Features found in this experiment are representative of all models performed with slopes of 15° and consist of the following, as shown by Figure 4.41:

- flow elongates downslope with very short upslope distances
- longitudinal profile follows the same structure revealed by manually obtained profiles shown in previous section with grouped profiles according to flow rate
- the intersection between longitudinal and profile number 1 reflects the location of the extrusion point
- the extrusion point and nearby area, mostly downstream, is a depression confined by edges slightly higher with very smooth slopes shown in profiles 1 and 2
- a transversal profile of the proximal area shows edges as smooth peaks followed by a depression, in profiles 3, and then goes up again to a plug region in the middle of the flow as shown by profile 4, prior to the maximum cross-slope section shown in profile 5
- the maximum cross-slope profile, number 5, shows a rather homogeneous surface with a small peak right in the center
- the distal portion of the flow shows a profile higher than the proximal area with a bulky central region, shown in profiles 6 to 7
- the flow front, in profile 8, is well rounded and presents the maximum depth found throughout the entire flow
- the presence of ridge-like structures between profiles 6 and 8

As previously stated during this chapter, morphological features here described are prominent in experiments performed on higher slopes and faster flow rates, but some of these features are also seen on the remaining models, structures that are present in the majority of experiments include ridge-like structures near the flow front area as evidence of different states of stress inside the flow, an inflated flow front portion with depressed area near the extrusion point zone as shown in Figure 4.22. To finalize this chapter, Figures 4.42, 4.43, 4.44, 4.45 present snapshots of each of the experiments developed in this thesis, where final state measured of textures and dimensions can be observed. It is also noticeable how some flows develop well established features as those seen in experiment 1cc54C, and others show less marked features, depending mainly on slope.

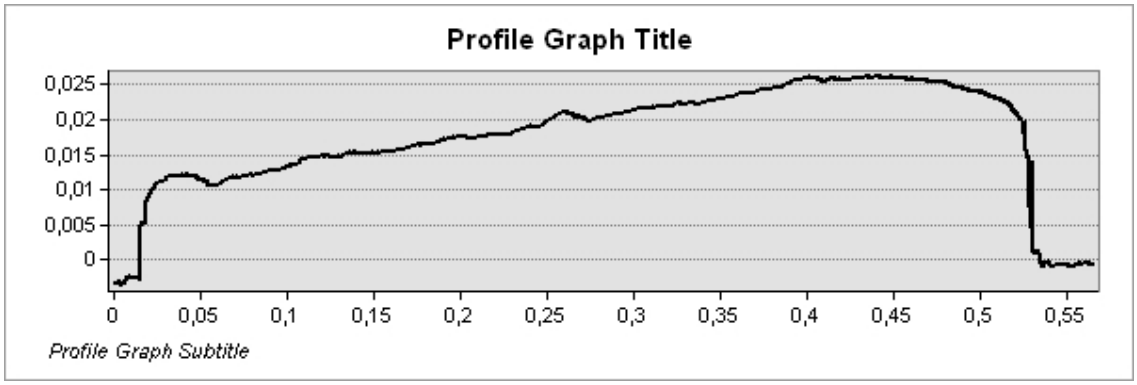

(a) Longitudinal profile.

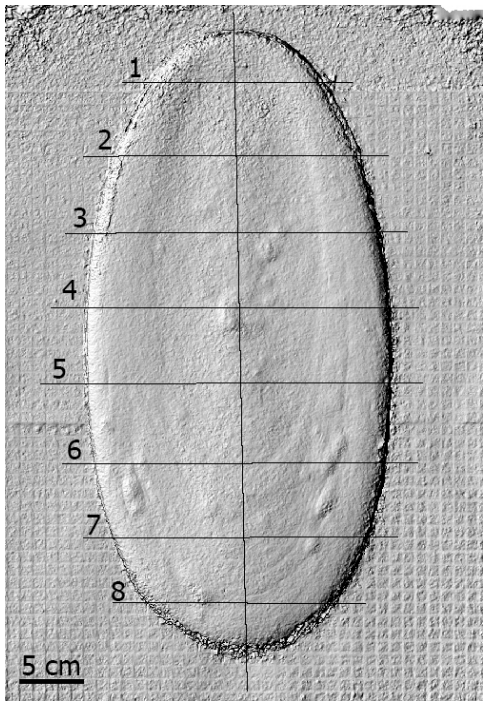

(b) Longitudinal profile.

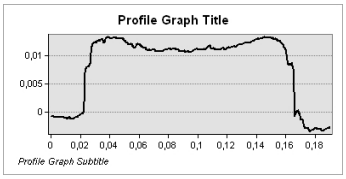

(c) Profile 1.

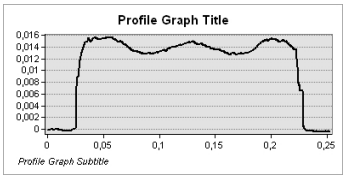

(d) Profile 2.

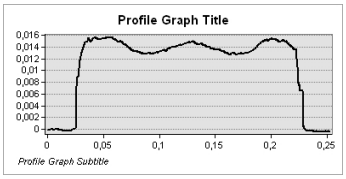

(e) Profile 3.

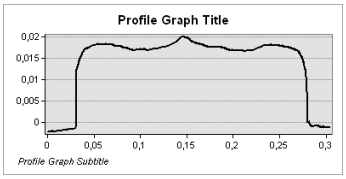

(f) Profile 4.

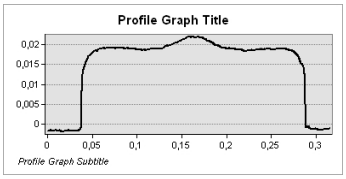

(g) Profile 5.

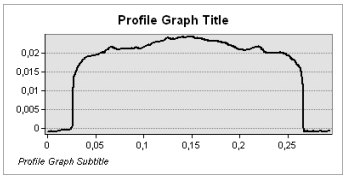

(h) Profile 6.

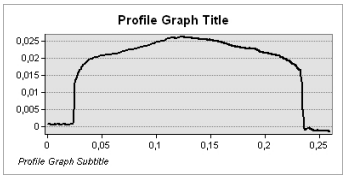

(i) Profile 7.

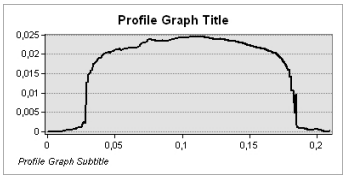

(j) Profile 8.

Figure 4.41: DEM model and corresponding profiles of experiment 1cc54C on a slope of 15°. Figure (a) shows the longitudinal profile with the extrusion point near the 0.05 (cm) shown as the shallower point of the flow. Figure (b) is a picture of the DEM model with all profiles shown numbered from the proximal area to extrusion point up to the flow front. Figures from (c) to (j) represent each of the profiles as indicated by (b).

Figure 4.42: Final flow morphology for Q = 1 (cc/s).

5cc48C

5cc50C 15° slope

5cc53C

5cc55C

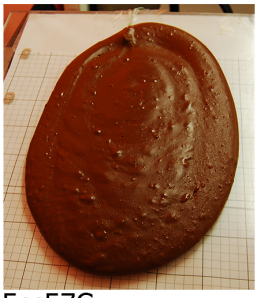

5cc57C

5cc58C

5cc59C

5cc63C

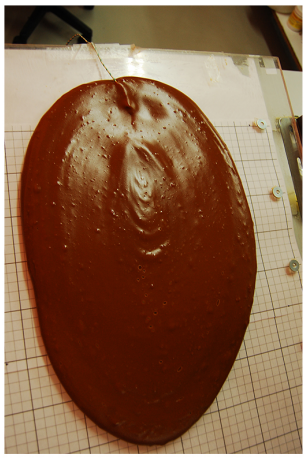

5a25cc

Figure 4.43: Final flow morphology for Q = 5 (cc/s).

Figure 4.44: Final flow morphology for Q = 10 (cc/s).

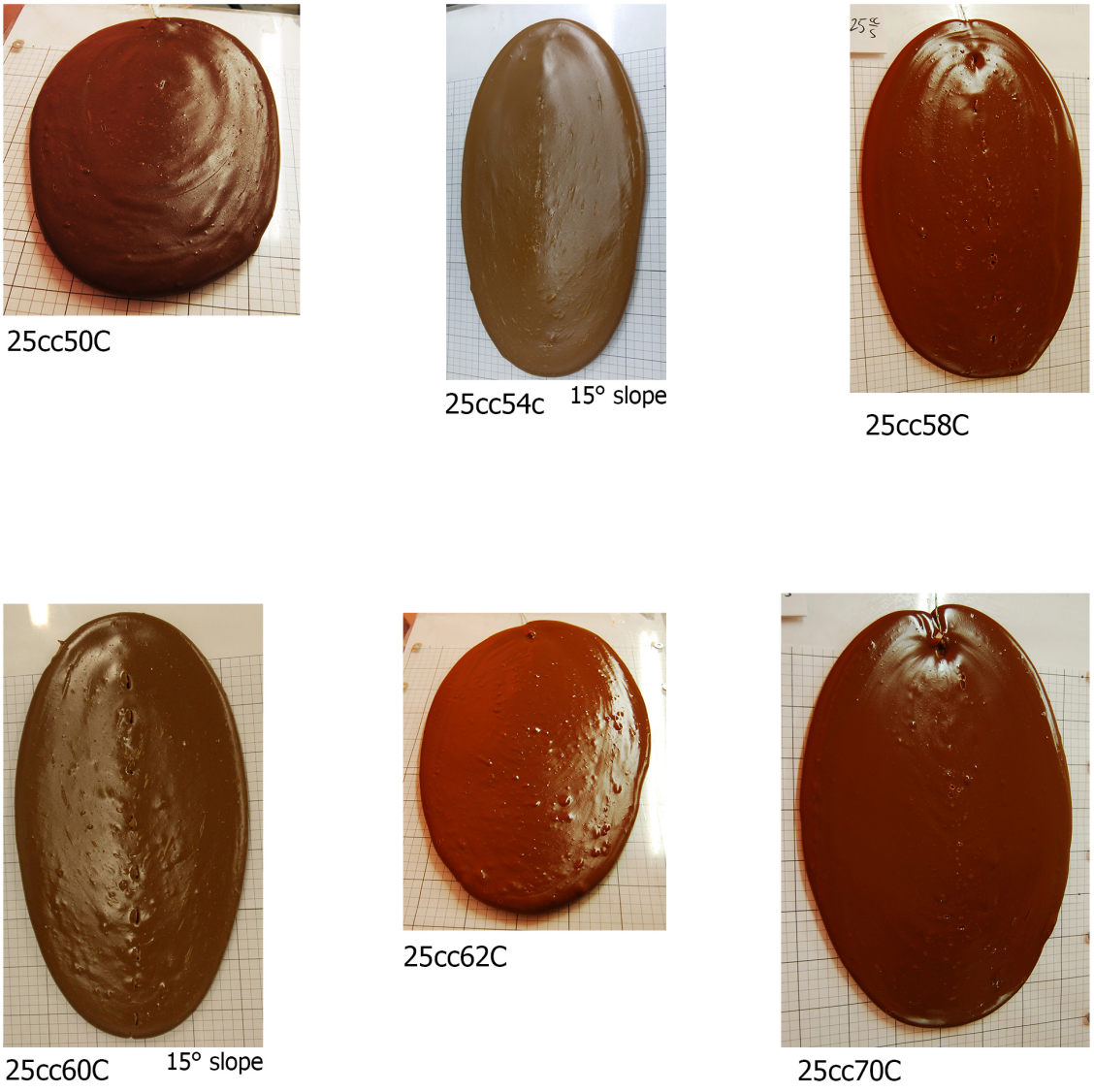

Figure 4.45: Final flow morphology for Q = 25 (cc/s).

Chapter 5

Discussion

The final chapter of this thesis presents the discussions studying the results of the experiments and comparison between previous analogue models and natural flows. We have performed laboratory experiments consisting of point extrusions of viscous material down an inclined plane in cooling and isothermal conditions. Results have shown that manjar is an interesting option for developing models of viscous lava flows given that conditions achieved in the laboratory are comparable to real lava flows as shown by qualitative similarities and according to dimensional analysis. First we will discuss the relevance of rheological evolution given the temperature dependent nature of the material in time over the emplacement conditions of the flows, as has been seen in lava flow evolution throughout several studies, focusing on what factors control dynamics and those that turned out to be irrelevant in our results. Next, we will deepen into the effects of varying flow rate and slope observed in our result as they show good agreement with the theory and nature flows. At last, there is a qualitative and quantitative comparison between previous analogue experiments found in the literature with our models, as well as those with natural lava flows.

An overall picture of the experiments is that, at a first glance, the chosen material seems to be a fairly easy to use, it develops flows with features comparable to those found in viscous lava deposits, with semi-oval shaped flows, in addition to levée like edges confining a central zone of shallower depth that culminates with inflated flow fronts. Likewise, rheological evolution of manjar is truly dependent upon initial temperature of the flows, resulting in very different emplacement times when the experiment was subject to cooling versus isothermal conditions. Also, the effects of varying initial flow rate and slope reflect on times of emplacement and final dimensions, revealing different dynamical regimes that depend upon these features. The comparison between manjar flows and lava flows reflects very similar dynamical regimes, as shown by dimensionless analysis of distance versus time, comparison between Reynolds and Froude number, and also due to Graetz number evolution over time.

Still, there are some issues that need to be taken into account when using this material, like the fact that it is not able to solidify completely, as opposed to other known materials like *PEG* or kaolin and *PEG* mixtures, and the inconsistencies given by the possibility that different batches of manjar may show up distinct results, as evidenced by the following issues: different textures described in Tables 4.1 and 4.2, the two experiments performed with 6 months old stored manjar that resulted in very high aspect ratio flows shown in Figure 4.22;

as well as the possibility that variations in water content could lead to a number of effects, and we did not take into account this factor until seeing the results, making it impossible to measure during the development of the models. Even though we assumed that foil packages allow for good conservation of manjar, because expiration times are longer than the period they were left to rest, this indicates the possibility that material properties vary with time from fabrication, which leads us to advice that experiments done with this material should be made during a period of weeks from manufacturing time shown in the package and more properties and rheological measurements could be done in order to better constrain results obtained.

Additionally, the limited number of experiments performed was not sufficient to deepen into some of the issues found when studying the results; in particular, matters like the handling of manjar, which turned out to present heterogeneous temperatures in the reservoir prior to a number of experiments, the lack of water content estimations during the performing of the models, the repeated use of a certain volume of manjar of up to three times, and the influence of time from manufacturing until performing the experiments, could have had better correlations if the number of experiments performed was higher. Still, our results are encouraging and this issues are here listed as an aid to those seeking to use this type of models for future work.

5.1 Rheology

The main goal of this work is to define the role of temperature dependent rheology in the evolution and final dimensions of the models. Our experiments have shown there is significant difference in the evolution regime of the flows when the material is subject to cooling versus isothermal conditions. We will discuss the nature of this difference and how it relates to processes observed in lava flows.

When studying viscous lava flows, the crystal content of the flows typically is what is thought to give the non-Newtonian behavior of lavas, which leads to producing flows with potent heights and generally high aspect ratios. However, crystal content is not the only factor influencing the non-Newtonian behavior of the flows, as there are other factors that can control flow dimensions producing potent heights and high aspect ratios, such as cooled crust formation that can hold up hotter inner material, avoiding the spreading of the core and generating channel free flows. Geological evidence of this phenomena include strain and accumulation structures, also known as ridges, that represent the differential stress regime suffered by the crust, balancing inner versus outer forces.

We find three relevant aspects to discuss regarding the rheological evolution of the flows that are relevant for our results. First, the initial temperature of the flows, followed by cooling versus isothermal conditions in the experiments and closing with water loss and its effects over manjar flows.

Initial temperature

We attempted to accomplish a range of initial temperatures from ambient up to boiling temperature for each of the flow rates used in order to determine the influence of amount of heating over flow advance and final dimensions. Results have shown that our control over initial temperature of the experiments were inaccurate, and some experiments present heterogeneous temperatures inside the reservoir, as indicated in subsection **Cooling and isothermal flows** in the previous chapter. The index of surface temperature over extrusion point reveals that some experiments did not reach thermal equilibrium prior to initializing the experiment, and present higher temperatures at the beginning of extrusion, followed by lower plateau temperature and then again high temperatures for the last bit of material extruded for a number of experiments in each of the flow rates, which we interpret as the temperature profile found within the reservoir due to our heating methods.

In this context, we even consider that, even though thermal control was inaccurate and the material presented heterogeneous temperatures, initial temperature does not reflect any type of control over dynamics, times of emplacement, morphologies, nor final dimensions in any of the flows, as shown in the previous chapter.

We consider the most relevant factors influencing emplacement of the flows are the following.

Cooling versus Isothermal flows

Results show the most notorious difference between flows in isothermal conditions versus cooling in the evolution of distance over time, as presented in the **Cooling versus isothermal flows** in **Chapter 4**. Regardless of flow rate or slope, experiments with previously heated material show excellent correlation with power law fits in time, first during total material extrusion, up until reaching a breaking point, defined as (t^*, L^*) in the previous chapter. Then, a second regime from this point on until halt. For most flows this transition point coincides closely with the end of material extrusion from the reservoir, which occurs at ζ_Q (s). On the contrary, both flows performed in isothermal conditions do not show a good correlation bewteen two power law fits in time with an inflection point defined as the transition point, but rather advance in a smoother and continuous way, considering a major number of power law fits could be found to relate distance to time, with no marked transition point whatsoever, as shown in Figures 4.25a, and 4.25b.

The fact that flows with cooling present a transition point from which flow velocity diminishes slowly until halt is very similar to the one that has been previously described for lava flow, which present *volume-limited* lengths. Flows grow predominantly at higher rates during material extrusion, until the total volume of the flow has been extruded, point from which final lengths are reached at very low velocities.

Even though isothermal flows do not accurately fit a power law adjustment, and the transition point is not as easy to determine as with cooling flows, there is a relevant change of slope at the end of material extrusion, but the rate of advance remains important even after this point, unlike results shown for experiments with cooling. Isothermal experiments are performed at room temperature with no heating of the material, which translates as a constant and higher yield strength, consistency and smaller flow index relative to their cooling counterparts as

the rheological characterization of our material determines. This lead us to believe thicker and shorter flows would result in isothermal conditions, but results show what was a rather misleading scenario, as isothermal flows presented inconsistent results. The lower flow rate, $Q = 1$ (cc/s), developed further downstream, reaching longer cross and downslope distances with shallower depths, which resulted in smaller aspect ratios than expected, along with much larger times of transition, t^*, and of cross-slope stabilization, evidencing slower but longer lived spreading. On the contrary, while timescales for $Q = 10$ (cc/s) remain on the same range, this experiment presented shorter final lengths and thicker depth. This result is counterintuitive, given that yield strength for ambient temperature flow is considerably larger than for heated material, so other factors should be considered.

As briefly mentioned before, we need to consider the relevance of water in the rheological behavior of manjar, which is a dairy product, and as such, water is an important part of its composition, because it could be as high as 30%. Given the fact that manjar loses water as soon as heating begins and not necessarily with or after boiling, as shown in the characterization of **Chapter 2**, this is the one factor we did not take into account when recording data of the flows. We believe the relevance of water loss lies within the superficial skin of manjar, which proves to hold on to important volumes of material in flow front regions, producing what we will call a pseudo-crust. The existence of the pseudo-crust can be related as well with Graetz number estimates, which will allow us to determine the growth of this pseudo-crust in time thanks to thermal diffusivity measurements made for manjar and supporting this theory.

For most experiments there is a noticeable material accumulation in the flow front region, presenting the thickest portion of the flows as presented by Figure 4.22. Therefore, we consider the existence of a pseudo-crust of manjar holding up inner material with higher mobility than the outer portion exposed to air and that continues to flow downslope given the smaller depths present near the extrusion point. The fact that temperature index at flow front region reaches a stable value for all experiments regardless of flow rate after total material extrusion supports this idea. The existence of this pseudo-crust makes it necessary to discuss the possible *volume-limited* character of the flows, given that manjar does not reach a solid state in experimental conditions used for this thesis, implying there was no real possibility for an outer crust to block all motion from a hotter and mobile interior as happens to *cooling-limited*.

Even though results show that manjar flows reached transition lengths at almost the same time as corresponding ζ_Q, as shown in Figures 4.3 and 4.4, 4.6, where the proximity of the transition point and end of material extrusion indicate the possibility that experiments are *volume-limited* flows that do not reach thermal maturity, as they grow predominantly during material injection and, once manjar supply ends, they continue to grow at a diminished rate until halt. We consider this happens only because the pseudo-crust of manjar is not as strong and is not able to hold up all hotter material in order to define a *cooling-limited* length but is able to stabilize advance reaching a constant velocity during extrusion due to the force exhibited by material injection followed up by a diminished velocity until halt.

Water loss

The effect of water loss seems to be considerably relevant compared to temperature control in the dynamics of the flow, because different initial temperatures do not point to consistent effects in final dimensions, regimes or flow front velocities. For this reason, the effect of water loss could be the most important difference between isothermal and cooling flows dynamics, which do show different results in all these matters as has been discussed in the previous sections.

We consider water loss, in conjunction with exposure to air and cooling, leads to the formation of a pseudo-crust that controls the emplacement of the flows, being able to contain hotter and mobile material. As shown by Figure 4.23, the number of uses of manjar does not seem to play an important role in mentioned results either, which takes us to consider water loss drops to a base level after the first time the material is heated and does not necessarily drops further for the second or third time manjar is used, as long as it is used during the same day. This last observation is made based on the use of material that was stored for a period of months before their first use, which shows the shortest and thickest profiles in Figure 4.22, evidencing there is an important difference between these flows of old manjar compared to those using batches bought shortly before performing the experiments. These results suggest that water loss due to heating is orders of magnitude less strong than the mixture between months old heated material, which is able to contain bigger stresses by showing larger thickness and smaller basal areas than their fresh material counterparts.

A similar issue arose for the authors Balmforth et al. (2006) with corn-syrup. In this work, effects of surface tension were aggravated by the evaporation of water from the superficial skin, evidenced by its ability to buckle and wrinkle, which took them to assume the skin behaved partly elastically and presumably supported some of the stresses exerted on the dome. They discussed the surface effects were probably responsible for qualitative but not quantitative agreement between observed and theoretical dome diagnostics. Kaolin flows developed in the same work, in addition to observed flows by previous authors, also show imperfections showing surface features taking form of intersecting arcs, even forming small-scale saw-tooth-like patterns at their edges, which they also conclude to be a consequence of drying out surface. They also state that surface tension effects might be responsible for the drying out of the fluid edge and surface layers, together with a change in rheology due to buckling and folding shown for a number of experiments.

For future studies, water loss data could be gathered by weighing total material in all stages of the experiments, prior to heating, in the reservoir and later when the flow has already reached its run-out length. Also, rheological measures should be done considering the state of water content. All these details could contribute to better constrain the effects of water in rheology and hence its control on flow dynamics, which to us seems to be the major factor influencing the differences found between isothermal and cooling experiments.

5.2 Variable parameters

Flow rate

Results show that for cooling experiments on a given slope, the times of emplacement of the flow are directly controlled by extrusion rate, reaching transition lengths, L^*, at times t^*, that turned out to be very similar to the extrusion timescale, ζ_Q, of the corresponding flow rate. This also translates into higher flow front velocities and shorter times of upslope and cross-slope stabilization for higher flow rate. This effect is noticeable within one order of magnitude difference between flow rates, specially when comparing results obtained for 1 (cc/s) versus 25 (cc/s) as seen in Figure 4.15. Final dimensions of the flows are slightly dependent upon flow rate as seen in aspect ratio results in Figure 4.20, where higher rate determined lower aspect ratios with wider flows and shallow depths, and lowest rates result in flows with greater depths and narrower widths. This could be due to the previously mentioned pseudo-crust, given that for higher flow rates it has developed for shorter time during evolution of the flows and allows for greater expansion of flow area, while for lower rates the crust develops further with ongoing extrusion, which results in stronger flow borders and vertical accumulation of material under the plastic pseudo-crust. Results shown in Figure 4.36 support this idea, as well as the Graetz number over time. Given that flows fully develop over or below the critical number, there are substantial differences in final flow dimensions given the wide range of strengths that the pseudo-crust possesses at certain points in time.

Slope

Our results indicate that a major factor controlling the final dimensions of the flows is slope. Steeper settings result in shorter times of axisymmetric regime, stabilizing upslope lengths sooner than most experiments and also at smaller distances, accompanied by narrower widths of the flows and larger downstream reaches for flow rates of 10 (cc/s) and lower, as shown in Figure 4.22. Transition lengths L^* are also larger when compared to the rest of the experiences, where manjar reached further distances at similar timescales as shown in Figure 4.15. This effect is similar to using higher flow rates and had already been studied by Lyman and Fink (2001), who determined that flow morphology was equally dependent of flow rate and underlying slope. Although for the range of initial flow rates used in this work it is not as evident, still we see how all transition lengths L^* for flows with $Q = 25$ (cc/s) turn out to be larger than the average transition length for flows with $Q = 1$ (cc/s) as seen in the same Figure 4.15. A possible explanation for the fact that experiments with highest flow rate and slope do not advance further than their lower Q counterparts, having final lengths of approximately 10 (cm) less, around 20% of total maximum length, could lay in the number of uses of manjar, which as indicated in Table 4.1 and 4.2 were the first for all experiments with Q from 1 to 10 (cc/s) and second for two experiments of highest Q. Also, none of the models performed at higher slopes were recorded until the flow came to a halt so there could be little difference due to this as well, although not as large as 20% as we can see in Figure 4.22.

This control is also evident in the final dimensions and morphology of the flows, where narrower widths also lead to more prominent features developing in manjar flows set on a 15°

slope as evidenced by snapshots shown for each of the models in the previous section, where depressed extrusion area, auto-confinement of central channel in between parallel structures at flow edge resembling levées, followed by the accumulation of material in inflated flow fronts, are common to all of these flows and more evident to the eye than for flows performed at lower slope.

5.3 Comparison with previous experiments

Our experimental installation is easy to replicate, inexpensive and the use is straightforward. Manjar can be used directly from the package and there is no need for prior preparation when compared to kaolin or *PEG* slurries that have to be mixed with water some time ahead of the experiments. Relevant rheological contrast can be achieved for flows exposed to air, contrary to those that rely on cold water to attain certain temperatures. One important limitation is that the reservoir and the hose that connects it with the surface have no thermal isolation, and for experiments with low extrusion rates there is up to 25% heat loss from freshly poured material to the latter stages of extrusion for experiments with the lowest flow rate. For higher rates heat loss is lower but still present, with an average of 15% in 5(cc/s) and almost 10% for 25 (cc/s). This scenario could be improved for future experiences.

All manjar flows display a continuous and mostly smooth surface in the majority of experiments as shown in Figure 4.1, unlike materials used previously as analogues Balmforth et al. (2006), discarding surface tension effects in the resulting slumps, in addition to slipping from the surface.

Experiments by Fink and Griffiths (1990), and Lyman et al. (2004), have related flow morphology and cooling rate via dimensionless values, such as ψ_a, that depend on variables we could not obtain for manjar flows, such as thermal expansion index. Despite this inconvenience, qualitative similarities are evident for experiments that present Bingham or Herschel Bulkley rheologies, as the ones shown by Balmforth et al. (2006), Balmforth et al. (2002) and Lyman et al. (2004), with resulting flows of similar geometry and aspect ratios. Balmforth also presents experiments to aid theoretical advances with slurries of kaolin plus *PEG*, and although Bingham numbers are quite different, resulting flows of very high Bingham number considered to be yield stress dominated result in very similar slumps, which leads us to believe there is something more than the value of yield strength only, which allows for the aspect ratio of the flows, which we have already discussed as the ability of the pseudo-crust to retain hotter material resulting in inflated flows.

5.4 Comparison with natural flows

Dynamics

Although results can be interpreted as flows being volume limited, it is necessary to acknowledge that the pseudo-crust of our models is weaker than the crust formed in lava flows, and could not stop the flow from advance as seen in *cooling-limited* case for lavas, given that manjar does not solidify completely. This pseudo-crust rather influences the advance rate of

the flow until ζ_Q, stabilizing it as seen by the different evolution regimes, followed by cooling versus isothermal experiments. This determines manjar models between *cooling limited* and *volume limited* flows. These statements could be studied further with more experiments, using a number of total volumes to determine the role of cooling over amount of material extruded. Our results enable us to state that the existence of such crust can lead to thicken flows regardless, of yield strength values, or, even so, that yield strength does not play such an important role as to control the dynamics of the flows as would the pseudo-crust.

Considering observation of a number of active flows already mentioned in the previous section, we can compare the dynamical evolution using dimensionless analysis as seen in Figure 4.38 for our experiments. Although time exponents differ, the collapse of curves shows the dynamics remain similar, but as has already been mentioned there appears to be inconsistencies for the first few points in each of the curves, which is why Figure 5.1 reveals the estimated time exponents for three different cases. The first is for downslope curve of each of the flows, the second shows the time exponent for dimensionless flow advance as seen in Figure 4.33 and the third is estimated for the same curve minus the first three data points. It reveals that time exponents ranges decrease considerably for flow rates from 1 (cc/s) to 10 (cc/s), which explains the curve collapse.

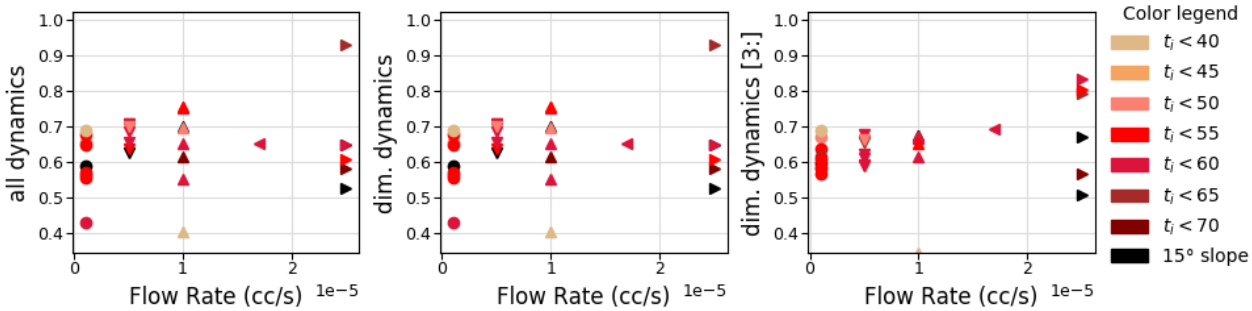

Figure 5.1: Comparison between time exponents of early regime. All dynamics refers to the one shown in Figure 4.5 for downslope curve. Dimensionless dynamics is the exponent estimated for normalized (π_1,π_2). Dimensionless dynamics [3:] is the same estimated exponent discarding the first three points in the curve.

Morphology

Qualitative similarities with lava flows are evident in transversal and longitudinal sections across the flow for the chosen experiment. Manjar tends to channelize hot material in between cooled down borders acting as levées that confine it, with depressed surface near the extrusion point, where hotter material was being injected and inflated flow front with accumulation of material being held down by cooled and more viscous surface skin. These features were enhanced for experiments performed on higher slopes, a characteristic that has also been observed in lava flows and coulées Gregg and Fink (2000). Regardless of slope, there are features common to all experiments such as deformed bubbles and apparent folding in the flow front that represent states of differential strain due to stress because of material accumulation, similar to ogives found in highly viscous flows, although in our experiments this occurrence is less evident and prominent, with very low wave length and depths but still enough to be seen in photographs and videos, considering our material does not solidify and only presents

a cooler and more viscous skin. Theoretical attempts to relate a minimum lava viscosity to the frequency and wavelength of fold structures have been made by Fink (1983).

Profiles shown in Figure 5.2 studied by Chevrel et al. (2016) show thick deposits of andesitic flows of viscosities ranging from 10^9 to 10^{10} $(Pa\ s)$, described as a typical viscous *coulée* of very large size, with the longest flow reaching up to 15 (km) long and 4 (km) wide, with an average thickness of 70 (m). Comparing these profiles to manjar profiles shown in Figure 4.41 some similarities can be found, as seen in flow number 8, where channeled lava is confined by higher levées until the central zone of the channel begins to inflate further downslope, reaching the flow front which presents material accumulation confined by the outer crust of the flows.

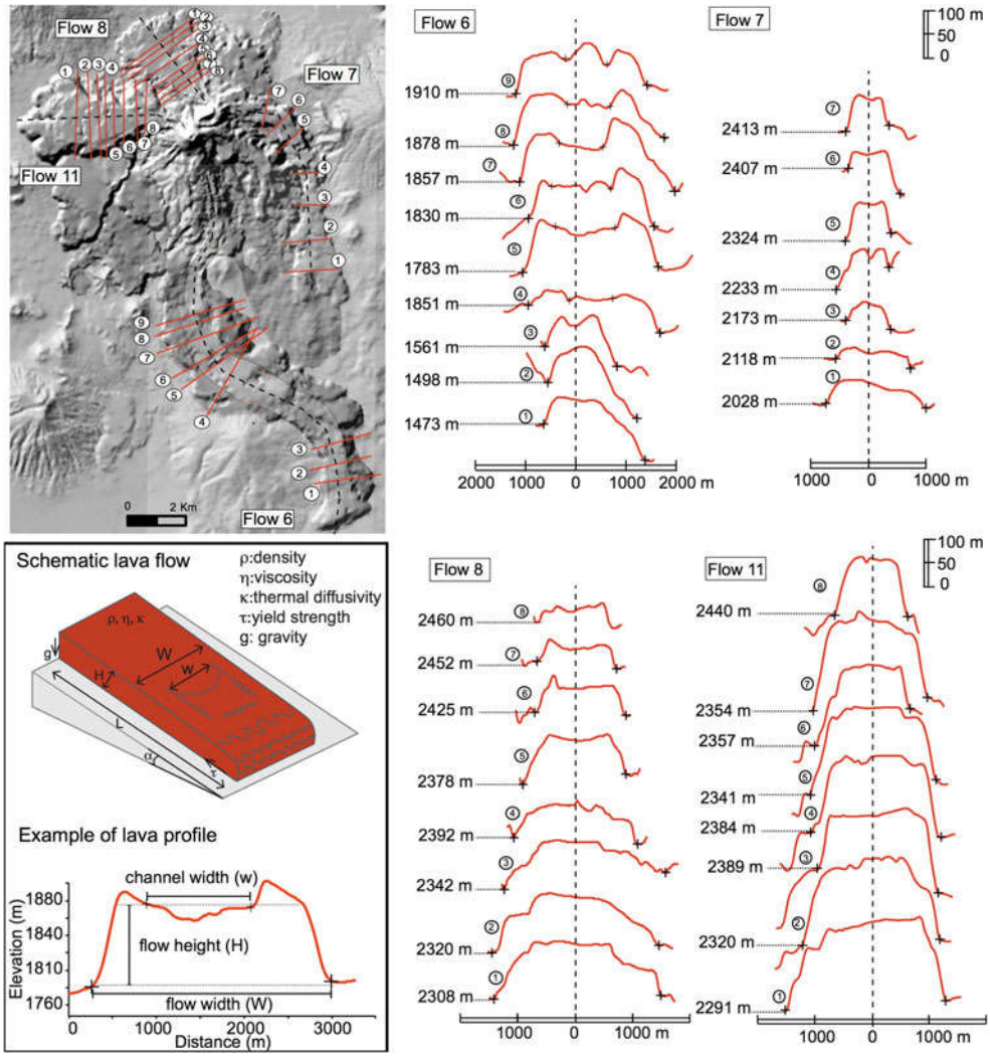

Figure 5.2: Examples of El Metate flow profiles, perpendicular to flow direction. Flow 8 presents channelized lava autoconfined by high levées in the proximal section of the flow, while the distal section presents inflated central zone showing material accumulation due to cooled outer crust retaining core material. Image from Chevrel et al. (2016).

Final profiles of our experiments represent different states of manjar rheology that illustrate through the final morphology the importance of material properties in emplacement features.

For lava flows the process known as inflation is illustrated by Figure 5.3, extracted from Calvari and Pinkerton (1998), for an aa flow of basaltic composition in etna volcano. This process involves high mobility of hotter interior of lava reflecting on carapace or crust exterior formed by cooled down material in contact with ambient conditions, showing that the plastic behavior prior to brittle deformation of the crust allows for expansion due to accumulation of large quantities of ductile material, which reflects in inflated portions of flow front and channel, where hotter and mobile material from the proximal portions of the flow comes to rest contained by the exterior. This is also reflected by deflated portions of the flow as seen in proximities of the extrusion point and throughout the channel downslope. Although this process has been described for flows of on-going eruptions with a series of pulses over time, we consider it relevant for our experiments given the final flow morphologies found, where flows show either deflated zones near extrusion along with an inflated flow front, or the absence of deflated zones that leads to round inflated flows as seen in Figure 4.22 for three flows of $Q = 1(cc/s)$.

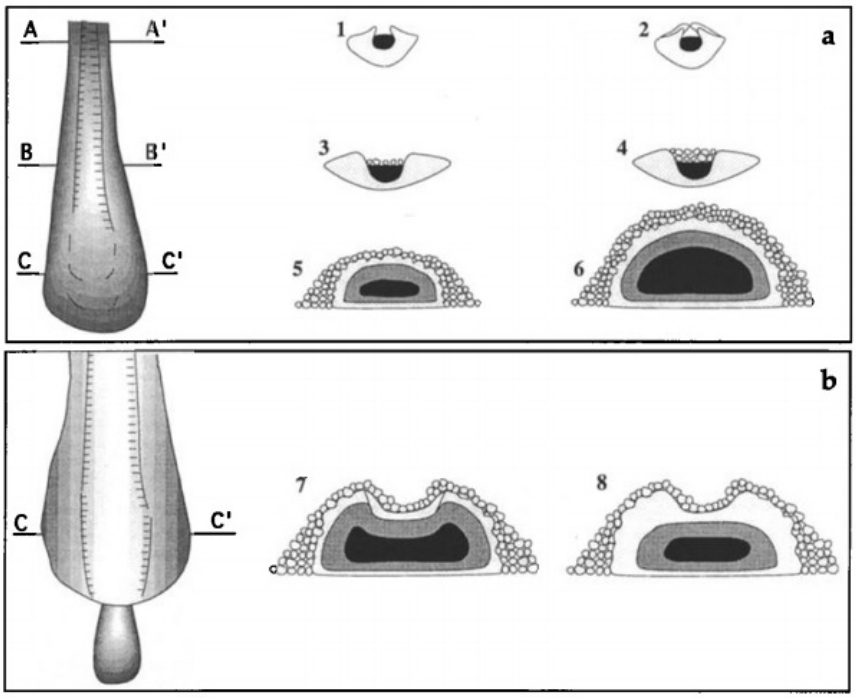

Figure 5.3: Illustrated example of inflation process in lava tubes. Image from Calvari and Pinkerton (1998).

On the last note, as shown by Figures 4.40, and 4.39, dimensionless analysis of flow final aspect ratio determines a power law relation of modified Reynolds and Froude number, aspect that has been studied for flows in permanent regime as mentioned by Filippucci et al. (2010). Our results agree about the existence of a scaling factor that could be obtained in order to relate flow dynamics with these parameters between experimental settings and natural lava flows. We suggest this topic for further study as it goes beyond the scope of this thesis.

Conclusions and suggestions

In the present study a series of experiments provided information regarding flow advance of a thermo rheological fluid in time. Our aim has been to determine the influence of a temperature dependent rheology upon flow dynamics and evolution. Results have shown there is significant contrast between cooling and isothermal experiments, mainly given by the formation of a pseudo-crust, which determines different times of emplacement, final dimensions and distance evolution over time for all experiments. The existence of a pseudo-crust is supported by the following. First, the contrast between dynamical evolution for cooling versus isothermal flows, which suggests there are different forces controlling the advance of manjar over time regardless of flow rate. Secondly, the different final dimensions and aspect ratios found for lower and higher flow rates, which show greatest contrast between the experiments. We propose this contrast is given by the existence of this pseudo-crust, and given the different extrusion timescales present for these two extremes, the development of this pseudo-crust is at different stages. As a consequence, for flows of higher flow rates, basal spreading of the flows goes further than for lower flow rate counterpart, that develop vertically, presenting greater thicknesses and smaller basal areas, due to greater crust development by total volume extrusion times. Lastly, the water content difference must play a role as well in the development of a pseudo-crust, feature that has already been seen by previous authors. Our results show that slope is a major factor controlling the final dimensions of the flow.

Although there are issues with our model that we could not completely resolve, as the precise role of water loss, age and number of uses of manjar, we find out that the results are encouraging. The experimental matrix could be improved as well by a number of items, from preparation to development, by: increasing the number of total volume extruded to consider the role of reservoir dimensions in the final length, divide experiments only by isothermal and cooling conditions, and not necessarily into a fixed temperature range, as we did in order to relate the amount of cooling to the final dimensions or dynamics of the flow, because initial temperature does not seem to be a relevant factor controlling neither of these parameters, as shown that flows with heterogeneous temperatures in the reservoir did not show any particular influence in flow dynamics or final extent. It could also be relevant to perform a new series of experiments of different initial volumes in order to obtain insight on the *cooling-limited* versus *volume-limited* lengths that could be reached by viscous flows like manjar.

The use of food as analogue material for silicate melts is not new as shown by Schellart (2011), Berthelote et al. (2008), and Baker et al. (2004), and for this reason we consider manjar remains an interesting material for further study of models with temperature dependent rheology and hope this work will help to restrict the topic of study and the factors to consider in new experiments.

Bibliography

Bagdassarov, N. and Pinkerton, H. (2004) A review and investigation of the non-newtonian properties of lavas based on laboratory experiments with analogue materials. *Journal of Volcanology and Geothermal Research*, 45(3).

Bagdassarov, N. and Pinkerton, H. (2004). Transient phenomena in vesicular lava flows based on laboratory experiments with analogue materials. *Journal of Volcanology and Geothermal Research*, 132(2):115–136.

Baker, D. R., Dalpé, C., and Poirier, G. (2004). The viscosities of foods as analogs for silicate melts. *Journal of Geoscience Education*, 52(4):363–367.

Balmforth, N. J. and Craster, R. V. (2000). Dynamics of cooling domes of viscoplastic fluid. *Journal of Fluid Mechanics*, 422:225–248.

Balmforth, N. J., Craster, R. V., Rust, A. C., and Sassi, R. (2006). Viscoplastic flow over an inclined surface. *Journal of non-newtonian fluid mechanics*, 139(1-2):103–127.

Balmforth, N. J., Craster, R. V., and Sassi, R. (2002). Shallow viscoplastic flow on an inclined plane. *Journal of Fluid Mechanics*, 470:1–29.

Balmforth, N. J., Frigaard, I. A., and Ovarlez, G. (2014). Yielding to stress: recent developments in viscoplastic fluid mechanics. *Annual Review of Fluid Mechanics*, 46:121–146.

Barbosa, V. C., Garcia-Rojas, E. E., Coimbra, J. S. d. R., Cipriano, P. d. A., Oliveira, E. B. d., and Telis-Romero, J. (2013). Thermophysical and rheological properties of dulce de leche with and without coconut flakes as a function of temperature. *Food Science and Technology (Campinas)*, 33(1):93–98.

Barnes, H. A., Hutton, J. F., and Walters, K. (1989). *An introduction to rheology*, volume 3. Elsevier.

Berthelote, A. R., Prakash, A., and Dehn, J. (2008). An empirical function to estimate the depths of linear hot sources: Laboratory modeling and field measurements of lava tubes. *Bulletin of Volcanology*, 70(7):813–824.

Calvari, S. and Pinkerton, H. (1998). Formation of lava tubes and extensive flow field during the 1991–1993 eruption of mount Etna. *Journal of Geophysical Research: Solid Earth*, 103(B11):27291–27301.

Cashman, K. V. and Sparks, R. (2013). How volcanoes work: A 25 year perspective. *Geological Society of America Bulletin*, 125(5-6):664–690.

Castruccio, A., Rust, A. C., and Sparks, R. (2010). Rheology and flow of crystal-bearing lavas: Insights from analogue gravity currents. *Earth and Planetary Science Letters*, 297(3):471–480.

Chevrel, M. O., Siebe, C., Guilbaud, M.-N., and Salinas, S. (2016). The ad 1250 el Metate shield volcano (Michoacán): Mexico's most voluminous holocene eruption and its significance for archaeology and hazards. *The Holocene*, 26(3):471–488.

Cimarelli, C., Costa, A., Mueller, S., and Mader, H. M. (2011). Rheology of magmas with bimodal crystal size and shape distributions: Insights from analog experiments. *Geochemistry, Geophysics, Geosystems*, 12(7).

Coltelli, M., Proietti, C., Branca, S., Marsella, M., Andronico, D., and Lodato, L. (2007). Analysis of the 2001 lava flow eruption of mt. Etna from three-dimensional mapping. *Journal of Geophysical Research: Earth Surface*, 112(F2).

Colucci, S., Papale, P., and Montagna, C. P. (2017). Non-newtonian flow of bubbly magma in volcanic conduits. *Journal of Geophysical Research: Solid Earth*, 122(3):1789–1804.

Cordonnier, B., Hess, K.-U., Lavallee, Y., and Dingwell, D. (2009). Rheological properties of dome lavas: Case study of Unzen volcano. *Earth and Planetary Science Letters*, 279(3-4):263–272.

Cordonnier, B., Lev, E., and Garel, F. (2016). Benchmarking lava-flow models. *Geological Society, London, Special Publications*, 426(1):425–445.

Cordonnier, B., Schmalholz, S., Hess, K.-U., and Dingwell, D. (2012). Viscous heating in silicate melts: An experimental and numerical comparison. *Journal of Geophysical Research: Solid Earth*, 117(B2).

Costa, A. (2005). Viscosity of high crystal content melts: dependence on solid fraction. *Geophysical Research Letters*, 32(22).

Devices, D. (2011). Kd2 pro thermal properties analyzer operator's manual version 4. *Decagon Devices, Pullman, WA. KD2 Pro thermal properties analyzer operator's manual version*, 4.

Dingwell, D. (2015). Properties of rocks and minerals–diffusion, viscosity, and flow of melts. Elsevier

Diniega, S., Smrekar, S., Anderson, S., and Stofan, E. (2013). The influence of temperature-dependent viscosity on lava flow dynamics. *Journal of Geophysical Research: Earth Surface*, 118(3):1516–1532.

Dragoni, M. (1997). Physical modelling of lava flows. *Annals of Geophysics*, 40(5).

Dzuy, N. Q. and Boger, D. (1985). Direct yield stress measurement with the vane method. *Journal of rheology*, 29(3):335–347.

Farquharson, J., James, M., and Tuffen, H. (2015). Examining rhyolite lava flow dynamics through photo-based 3d reconstructions of the 2011–2012 lava flowfield at Cordón-Caulle, Chile. *Journal of Volcanology and Geothermal Research*, 304:336–348.

Filippucci, M., Tallarico, A., and Dragoni, M. (2010). A three-dimensional dynamical model for channeled lava flow with nonlinear rheology. *Journal of Geophysical Research: Solid Earth*, 115(B5).

Fink, J. H. (1983). Structure and emplacement of a rhyolitic obsidian flow: Little glass mountain, medicine lake highland, northern California. *Geological Society of America Bulletin*, 94(3):362–380.

Fink, J. H. and Griffiths, R. W. (1990). Radial spreading of viscous-gravity currents with solidifying crust. *Journal of Fluid Mechanics*, 221:485–509.

Giordano, D., Russell, J. K., and Dingwell, D. B. (2008). Viscosity of magmatic liquids: a model. *Earth and Planetary Science Letters*, 271(1):123–134.

Gregg, T. K. and Fink, J. H. (2000). A laboratory investigation into the effects of slope on lava flow morphology. *Journal of Volcanology and Geothermal Research*, 96(3-4):145–159.

Griffiths, R. W. (2000). The dynamics of lava flows. *Annual Review of Fluid Mechanics*, 32(1):477–518.

Guest, J., Kilburn, C., Pinkerton, H., and Duncan, A. (1987). The evolution of lava flow-fields: observations of the 1981 and 1983 eruptions of mount Etna, Sicily. *Bulletin of Volcanology*, 49(3):527–540.

Harris, A. J., Flynn, L. P., Matias, O., Rose, W. I., and Cornejo, J. (2004). The evolution of an active silicic lava flow field: an etm+ perspective. *Journal of Volcanology and Geothermal Research*, 135(1-2):147–168.

Hess, K.-U., Cordonnier, B., Lavallée, Y., and Dingwell, D. B. (2008). Viscous heating in rhyolite: An in situ experimental determination. *Earth and Planetary Science Letters*, 275(1-2):121–126.

Hui, H. and Zhang, Y. (2007). Toward a general viscosity equation for natural anhydrous and hydrous silicate melts. *Geochimica et Cosmochimica Acta*, 71(2):403–416.

Huppert, H. E. (1982). The propagation of two-dimensional and axisymmetric viscous gravity currents over a rigid horizontal surface. *Journal of Fluid Mechanics*, 121:43–58.

DIN ENISO 3219:1994 (1994). Plastics - Polymers/resins in the liquid state or as emulsions or dispersions - Determination of viscosity using a rotational viscometer with defined shear rate. Standard.

Jeffreys, H. (1925). Lxxxiv. the flow of water in an inclined channel of rectangular section. *The London, Edinburgh, and Dublin Philosophical Magazine and Journal of Science*, 49(293):793–807.

Lavallée, Y., Hess, K.-U., Cordonnier, B., and Bruce Dingwell, D. (2007). Non-newtonian rheological law for highly crystalline dome lavas. *Geology*, 35(9):843–846.

Lipman, P. W. and Banks, N. G. (1987). Aa flow dynamics, Mauna Loa 1984. *US Geol Surv Prof Pap*, 1350:1527–1567.

Lister, J. R. (1992). Viscous flows down an inclined plane from point and line sources. *Journal of Fluid Mechanics*, 242:631–653.

Liu, Z., Zhang, L., Malfliet, A., Blanpain, B., and Guo, M. (2018). Non-newtonian behavior of solid-bearing silicate melts: An experimental study. *Journal of Non-Crystalline Solids*, 493:65 – 72.

Lyman, A. W. and Fink, J. H. (2001). Predicting yield strengths and effusion rates of silicic lavas on slopes from analog experiments with bingham plastic materials. In *AGU Fall Meeting Abstracts*.

Lyman, A. W., Koenig, E., and Fink, J. H. (2004). Predicting yield strengths and effusion rates of lava domes from morphology and underlying topography. *Journal of Volcanology and Geothermal Research*, 129(1):125 – 138. The role of laboratory experiments in volcanology.

Magnall, N., James, M. R., Tuffen, H., and Vye-Brown, C. (2017). Emplacing a cooling-limited rhyolite lava flow: similarities with basaltic lava flows. *Frontiers in Earth Science*, 5:44.

Malin, M. C. (1980). Lengths of hawaiian lava flows. *Geology*, 8(7):306–308.

Moitra, P. and Gonnermann, H. (2015). Effects of crystal shape-and size-modality on magma rheology. *Geochemistry, Geophysics, Geosystems*, 16(1):1–26.

Naranjo, J., Sparks, R., Stasiuk, M., Moreno, H., and Ablay, G. (1992). Morphological, structural and textural variations in the 1988–1990 andesite lava of Lonquimay volcano, Chile. *Geological Magazine*, 129(6):657–678.

Navarro-Ochoa, C., Gavilanes-Ruíz, J. C., and Cortés-Cortés, A. (2002). Movement and emplacement of lava flows at volcán de Colima, méxico: november 1998–february 1999. *Journal of Volcanology and Geothermal Research*, 117(1-2):155–167.

Nichols, R. L. (1939). Viscosity of lava. *the Journal of Geology*, 47(3):290–302.

Pallister, J. S., Diefenbach, A. K., Burton, W. C., Muñoz, J., Griswold, J. P., Lara, L. E., Lowenstern, J. B., and Valenzuela, C. E. (2013). The Chaitén rhyolite lava dome: Eruption sequence, lava dome volumes, rapid effusion rates and source of the rhyolite magma. *Andean Geology*, 40(2):277–294.

Petford, N. (2003). Rheology of granitic magmas during ascent and emplacement. *Annual Review of Earth and Planetary Sciences*, 31(1):399–427.

Pinkerton, H. and Norton, G. (1995). Rheological properties of basaltic lavas at sub-liquidus temperatures: laboratory and field measurements on lavas from mount Etna. *Journal of Volcanology and Geothermal Research*, 68(4):307–323.

Pinkerton, H. and Sparks, R. (1978). Field measurements of the rheology of lava. *Nature*, 276(5686):383.

Pinkerton, H. and Wilson, L. (1994). Factors controlling the lengths of channel-fed lava flows. *Bulletin of Volcanology*, 56(2):108–120.

Pistone, M., Cordonnier, B., Caricchi, L., Ulmer, P., and Marone, F. (2015). The viscous to brittle transition in crystal- and bubble-bearing magmas. *Frontiers in Earth Science*, 3:71.

Schellart, W. (2011). Rheology and density of glucose syrup and honey: Determining their suitability for usage in analogue and fluid dynamic models of geological processes. *Journal of Structural Geology*, 33(6):1079–1088.

Sigurdsson, H., Houghton, B., McNutt, S., Rymer, H., and Stix, J. (2015). *The encyclopedia of volcanoes*. Elsevier.

Spera, F. J., Borgia, A., Strimple, J., and Feigenson, M. (1988). Rheology of melts and magmatic suspensions: 1. design and calibration of concentric cylinder viscometer with application to rhyolitic magma. *Journal of Geophysical Research: Solid Earth*, 93(B9):10273–10294.

Stasiuk, M. V., Jaupart, C., Stephen, R., and Sparks, R. (1993). Influence of cooling on lava-flow dynamics. *Geology*, 21(4):335–338.

Vetere, F., Behrens, H., Holtz, F., and Neuville, D. R. (2006). Viscosity of andesitic melts—new experimental data and a revised calculation model. *Chemical Geology*, 228(4):233–245.

Vicari, A., Ciraudo, A., Del Negro, C., Herault, A., and Fortuna, L. (2009). Lava flow simulations using discharge rates from thermal infrared satellite imagery during the 2006 etna eruption. *Natural Hazards*, 50(3):539–550.

Vona, A., Romano, C., Dingwell, D., and Giordano, D. (2011). The rheology of crystal-bearing basaltic magmas from Stromboli and Etna. *Geochimica et Cosmochimica Acta*, 75(11):3214–3236.

Walker, G. (1971). Compound and simple lava flows and flood basalts. *Bulletin Volcanologique*, 35(3):579–590.

Walker, G., Huntingdon, A. T., Sanders, A. T., and Dinsdale, J. L. (1973). Lengths of lava flows [and discussion]. *Philosophical Transactions of the Royal Society of London. Series A, Mathematical and Physical Sciences*, 274(1238):107–118.

Whittington, A. G., Hellwig, B. M., Behrens, H., Joachim, B., Stechern, A., and Vetere, F. (2009). The viscosity of hydrous dacitic liquids: implications for the rheology of evolving silicic magmas. *Bulletin of Volcanology*, 71(2):185–199.

Wolfe, E. (1988). Geologic observations and chronology of eruptive events. *The Pu'u'O'o eruption of Kilauea Volcano, Hawaii: episodes 1 through 20, January 3, 1983, through June 8, 1984*.